

On the sensitivity of cavitation inception & dynamics for water quality

MT54035: MSc Thesis

Sacha Oonincx

Delft University of Technology

(This page is intentionally left blank)

Thesis for the degree of MSc in Marine Technology in Ship Hydromechanics

On the sensitivity of cavitation inception & dynamics for water quality

by

Sacha Oonincx

Performed at

Andritz Hydro

This thesis (MT.24/45.014.M) is classified as confidential in accordance with the general conditions for projects performed by the TUDelft.

to be defended publicly on Friday November 8, 2024 at 02:00 PM.

Company Supervisors

Responsible supervisor: M. Neuhauser

Daily supervisors: M. Guggenberger and R. Peyreder

Thesis exam committee

Chair: D. Fiscaletti

Staff member: Prof. T. van Terwisga

Staff member: R. Stigter

Company member: M. Neuhauser

An electronic version of this thesis is available at <http://repository.tudelft.nl/>.

Preface

This Master's thesis marks the end of my academic career as a student at TU Delft. From the start of this career, courses focusing on fluid mechanics caught my interest, with a specific focus on cavitation. Hence, a topic focusing on experimental work on cavitation seemed the perfect fit for me. My achievements during this period could not have been established without the support of numerous people. Therefore, I want to take the opportunity to thank a few of them in particular.

First of all, I would like to thank Tom van Terwisga and Magdalena Neuhauser for initiating this master's thesis and allowing me to study a topic within my field of interest and simultaneously discover the beauty of Austria. Next, I would like to thank my supervisors, Daniele Fiscaletti and Rens Stigter from TU Delft, for their invaluable support during the project and, more importantly, their enthusiasm for the topic. Moreover, I would like to thank Mark Guggenberger and Rudolf Peyreder from Andritz for their extensive support in Austria. Furthermore, I want to express my gratitude to Michael Salfinger for his support in my work while always ensuring a good laugh. I also want to acknowledge the positive support that I received from LaVision and RECENDT, considering the hardware that I used during my measurements.

Lastly, I would like to thank my friends and family for their encouragement over the past years. A special thanks to my dad for his enthusiasm, which resulted in a lot of interesting discussions around the dinner table, my mom for keeping me sane from these discussions, distracting me when necessary and her positivity, and my sister for her endless patience, which allowed me to talk about bubbles endlessly. I also want to thank Britney, Thomas, my friends from Hydro Motion, and my academic friends for their support over the years.

*Sacha Oonincx
Delft, October 2024*

Abstract

The microbubble content is considered one of the most important fluid characteristics influencing cavitation inception and dynamics. However, the effects of microbubbles on cavitation are not yet precisely understood. The current work experimentally assesses the influence of microbubbles on cavitation around the runner of a hydraulic turbine model in a hydraulic test facility. Microbubbles are measured upstream of the model using IPI, while cavitation is observed visually. IPI measurements are performed under different DO concentrations, thereby changing the microbubble content in the facility, at different runner speeds. The results show an increase in microbubble sizes and concentrations for higher DO concentrations. The sizes and concentrations of microbubbles increase accordingly with decreasing σ . This increase is not only the result of a pressure reduction at the measurement position but also the appearance of a cavitating vortex at the outlet of the runner, causing additional bubbles measured at the measurement position. These effects are highlighted once again after the onset of gap cavitation, showing the influence of cavitation on the measured microbubble content as no resorber is located in the test facility. A decrease in the microbubble concentration is observed after the onset of gap cavitation for increasing DO concentrations, as oxygen diffuses into cavitation bubble. Moreover, at low values of σ , a vacuum is applied to the system, resulting in a faster decrease in the DO concentration at a higher initial DO concentration, resulting in a decrease of the microbubble content. A delay in the onset of gap cavitation is observed at lower DO concentrations due to the availability of fewer and smaller microbubbles in the facility. After the onset of cavitation, the development of gap cavitation is significantly altered by a change in the DO concentration. It is shown that gap cavitation covers a larger area of the runner at high DO concentrations, most likely caused by an increase in the vapour volume fraction at the outlet of the labyrinth seal, thereby increasing the number of vapour bubbles around the gap of the runner.

Contents

Preface	i
Abstract	ii
List of Figures	x
List of Tables	xi
Nomenclature	xii
1 Introduction	1
1.1 Problem definition	2
1.2 Relevance and research objective	4
1.3 Outline	4
2 Cavitation and microbubbles	5
2.1 Introduction	6
2.2 Flow parameters	6
2.3 Microbubbles	7
2.3.1 Bubble Dynamics	7
2.3.2 Critical bubble size and pressure	9
2.3.3 Dissolved oxygen content	10
2.3.4 Surface tension	11
2.3.5 Viscosity	12
2.4 Effects of microbubbles on cavitation inception	12
2.4.1 Activation rate	12
2.4.2 Inception condition	13
2.4.3 Inception zone	13
2.5 Effects of microbubbles on cavitation dynamics	14
2.5.1 Dynamics of sheet cavitation	14
2.5.2 Periodic shedding	14
3 Interferometric Particle Imaging	16
3.1 Introduction to measuring techniques	17
3.2 Principles of Interferometric Particle Imaging	17
3.2.1 General arrangement	18
3.2.2 Mie Scattering	18
3.2.3 Limitations of IPI	20
3.3 Image processing	21
3.4 Uncertainty in microbubble size	22
4 Principles of hydraulic turbines and model testing	24
4.1 Introduction to hydraulic turbines	25
4.2 Francis Turbine	26
4.3 Operating conditions of hydraulic turbines	27
4.4 Hillchart	27
4.5 Model testing	30
4.6 Cavitation on model scale	31
5 Methodology	35
5.1 Camera calibration	36
5.1.1 General arrangement	36
5.1.2 Circle detection	36

5.1.3	Focal plane	38
5.1.4	Magnification	39
5.1.5	Collection angle and disk diameter	40
5.2	IPI measurements	41
5.2.1	Test location	41
5.2.2	General arrangement	42
5.2.3	Adapted arrangement	43
5.2.4	Measurement procedure	44
6	Post processing of IPI data	48
6.1	Bubble detection	49
6.2	Postprocessing of microbubble data	52
6.2.1	IPI calibration	52
6.2.2	Resolution	54
6.2.3	Concentration estimation	55
7	Results	59
7.1	Variation in DO concentration	60
7.2	Microbubble content	61
7.2.1	DO variation at the critical working point	61
7.2.2	DO variation at a non-critical working point	66
7.2.3	Air injection	67
7.2.4	Freshwater replacement	68
7.2.5	Repeatability of IPI measurements	70
7.3	Microbubbles and cavitation	71
7.3.1	Gap cavitation inception	71
7.3.2	Turbine efficiency drop	72
7.3.3	Cavitation development	73
8	Conclusions	76
9	Recommendations	79
	References	82
A	Background information	89
A.1	Filters	89
A.2	Hough transform	91
A.3	Fourier Transform	92
B	Concentration distributions	94

List of Figures

1.1	3D render of a) a whole Francis Type 350 turbine model and b) the inside of a Francis 350 turbine model. Water enters the turbine in the grey cylinder in the top left. The radial inflow in the green block is converted to an axial outflow causing a rotation of the turbine blades.	3
2.1	Phase diagram for water, indicating typical phase changes by increasing the temperature (boiling) and by decreasing the pressure (cavitation) [10].	6
2.2	Change in bubble radius for different local pressures for an initial bubble size $R_0=100 \mu\text{m}$ and a water temperature $T=20^\circ\text{C}$	9
2.3	Relation between bubble size, tensile strength and bubble concentration for different nuclei populations. The depleted case was measured with Centerbody Susceptibility Meter (CSM), while the abundant and sparse cases were measured with Interferometric Particle Imaging (IPI) [22]	10
2.4	Relation between DO content and a) bubble concentration and b) corresponding size distribution for a tunnel condition $p=77\text{kPa}$ and $U=7 \text{ m/s}$ [33]. c) Bubble concentration as a function of DO content in a closed tunnel with operating conditions $p=50 \text{ kPa}$, $U=7 \text{ m/s}$ and $\gamma=30\text{-}39\%$ [39]	11
2.5	a) Relation between the surface tension of water and the concentration of a) a surfactant [49], b) salts [50]. Here, C_{20} and CMC denote the surfactant concentration at a 20% reduction of the surface tension and the critical micelle concentration, respectively.	12
2.6	Activation rate A per unit diameter as a function of the nuclei diameter in a) depleted water and b) abundant water for different cavitation numbers. For both cases, the blue, orange and green curves represent a σ of 1.0, 0.9 and 0.8, respectively. [53]	13
2.7	Relation between inception location s_i/c and cavity length L_{max}/c of TVC for different a) nuclei populations and b) cavitation numbers σ . [54]. The mono and polydisperse populations refer to microbubbles in the order of $\mathcal{O}(100\mu\text{m})$ and $\mathcal{O}(10 - 100\mu\text{m})$ in the liquid.	13
2.8	Illustration of the leading edge of a cavitating hydrofoil at a constant $\sigma=0.55$ for a) a depleted case and b) an abundant case. For the depleted case, glassy spanwise cells indicate the presence of a laminar separation bubble For the abundant case, many nuclei activations are visible along the span, growing separately [22].	14
2.9	Cavitation regimes for the upper side of a plano-convex hydrofoil for $Re=2000$. Periodic shedding of sheet cavitation is observed in the periodic zone, characterised by the angle of attack and the cavitation number.	14
2.10	Space-time diagram for a) a depleted and b) an abundant population of nuclei. Snapshots are made at midspan, $z/b=0.5$, of the NACA0115 hydrofoil, and the flow is from bottom to top. The purple dotted lines indicate the time points of the snapshots. The blue, green, orange and red lines indicate the extension of the cavity, region of the re-entrant jet, the shockwave regime and advection, respectively [22]	15
3.1	Nuclei concentration, C , and diameter, d , ranges for three different measuring techniques: red, blue and green region indicating Cavitation Susceptibility Meter (CSM), Mie Scattering Imaging (MSI) and Long-Range Microscopic Shadowgraphy (LMS). The lines represent the measurements carried out in the Australian Maritime College (AMC) tunnel [33]	17
3.2	a) General arrangement of an IPI configuration showing the main parameters of the setup [31] b) out-of-focus image for different bubble sizes [17]	18

3.3	a) Possible ways the light from a laser can scatter on a spherical transparent bubble. The red and blue lines indicate reflected and refracted light, respectively [63] b) Overview of the different parameters that are used in the Mie Scattering theory. The light from a wave, E_i , propagating along the x-axis is scattered by a bubble in the origin. The green plane indicates the logarithmic intensity variations for varying scattering angles θ [17]	19
3.4	Relation between calibration constant κ for $\theta=85^\circ$ and bubble diameter. The black and blue lines represent the derived values for κ of the perpendicular and parallel scattering plane over the entire range of bubble diameters, respectively. The red and pink curves represent a polynomial fit of the black and blue lines, respectively. [66]	20
3.5	Correlation between the number of fringes and the bubble diameter as a function of α for $\theta=45^\circ$	21
3.6	Out-of-focus images of microbubbles illustrating a) overlapping regions causing interference of fringe patterns [69], b) a distorted fringe pattern due to scattering of light from other microbubbles [69], c) distortion in a fringe pattern caused by a small particle.	21
3.7	a) Fringe pattern ($f=0.05$ cycles/px) for a resolution of 200 by 100 px and b) corresponding spatial frequency retrieved from FFT analysis	22
4.1	Schematic overview of a hydraulic power plant showing the reservoir, penstock and hydraulic turbine. The direction of the flow is indicated by the blue arrow. The height difference between the water level in the reservoir and the centerline of the turbine runner (here simplified to the turbine) is defined by the gross head H_g	25
4.2	Schematic of existing hydraulic turbines and their components	26
4.3	Existing hydraulic turbines and their operating range (Private communication).	26
4.4	Overview of the different components inside a Francis turbine. I and \bar{I} represent the inlet spiral, the high-pressure side and the outlet of the draft tube, the low-pressure side of the turbine. Modified from Nicolet [76]	27
4.5	Four quadrant characteristics of turbines adjusted from International Electrotechnical Commission [74]	27
4.6	Propeller efficiency curve at $n_{ED}=0.2234$. The blue and red curves represent the normalised efficiency and the AOA, respectively. For each propeller curve diagram, the efficiency of the turbine can be determined as a function of the AOA of the guide vanes and thus the Q_{ED}	28
4.7	Predicted Hillchart of the Francis RD-188 Type. The blue dots around the normal continuous operating range show the operating points of the Francis RD 188-Type where cavitation is predicted. The best efficiency point (BEP) of the turbine is indicated by the dot inside the turbine's normal continuous operating range. The values for the BEP and the isocurves for efficiency are not shown for confidential reasons.	29
4.8	a) Schematic of a radial test rig used to conduct the measurements in this study, b) Close-up of the turbine model and tank downstream of the turbine. The suction head H_s is controlled by the water level TWL , which is controlled by vacuum and pressurised air. Both of these systems can be controlled by valves above the tank.	31
4.9	Different regimes in a standard Hillchart of a Francis turbine indicating the different forms of cavitation: 1) inlet edge suction side, 2) inlet edge pressure side, 3) inter blades vortices, 4) cavitating vortex free zone, 5) part load cavitating vortex, 6) full load cavitating vortex, 7) bubble cavitation at the outlet edge suction side. Here, Ψ , ϕ and GVO denote the n_{ED} , Q_{ED} and the guide vane opening, respectively. These parameters are normalised to the turbine's BEP.	32
4.10	Runner of a Francis RD-188 Type model showing the different components where different forms of cavitation can be observed.	32
4.11	Francis RD-188 Type runner a) free of a cavitating vortex, b) with a cavitating vortex appearing at the outlet of the runner	33
4.12	Schematic overview of a total Francis model (left), close-up of a Francis model from the front (middle), and close-up of the outer edge of the Francis turbine (right). The different components of the Francis turbine are as follows: spiral casing (blue), runner blades (green), labyrinth (yellow), and the draft tube (red). The labyrinth exit is located in the blue plane (right) [78].	33

4.13 a) Francis RD-188 Type model, showing a cavitating vortex in the outlet of the runner and vapour bubbles at the gap of the runner, marked with the red box. b) Close-up of a part of the gap showing the first vapour bubbles.	34
5.1 Illustration of a) the general arrangement of the camera calibration, and b) an R2L2S3P4 Thorlabs fixed grid distortion target plate.	36
5.2 Application of an intensity threshold to an image (Figure 5.1b) of the R2L2S3P4 Thorlabs fixed grid distortion target plate. The regions with an intensity above the intensity threshold are marked with purple, while those with an intensity below the threshold are marked with yellow. Circles are detected within the yellow regions only.	37
5.3 A schematic overview of the position of an object with respect to the lens and focal plane of the camera. Here, z_1 and z_0 denote the distance between the lens and focal plane and the distance between the focal plane and object, respectively. For an object positioned in the focal plane, $z_0=0$ mm.	38
5.4 Relation between the out of focus distance z_0 and the width of the 2D Gaussian χ . At the minimum of this function, the edges of the dots are the most sharp, which can be found when the target plate is positioned in the focal plane of the camera.	39
5.5 Relation between the magnification of the camera and z_0 . The curve and shaded areas represent the mean and std of the magnification. For $z_0=0$ mm, the target plate is positioned in the focal plane of the camera.	40
5.6 Schematic overview of the position of microbubbles with respect to the focal plane. For increasing z_0 , the image size of a microbubble increases.	41
5.7 Schematic of the pipe segment used for the IPI measurements. The laser beam enters the pipe segment via the bottom window and leaves via the top window. The front window functions as an opening for the high-speed camera. The laser windows have a diameter of 50 mm, while the camera window has a diameter of 150 mm.	42
5.8 Overview of the a) total intended IPI setup and b) small optical components mounted on a breadboard.	43
5.9 Overview of the different components of the reversed IPI setup. Demineralised water can be circulated with the blue tubes, causing the cooling plate, and indirectly the laser, to drop in temperature. The sheet optics are located behind the laser and cooling plate but are not visible here. A close-up of these components is shown in Figure 5.10	43
5.10 Close up of the sheet optics when a) the laser is not operating, b) the laser is operating. The laser beam first enters the sheet optics housing and is then projected into the bottom window of the pipe segment by a coated mirror.	44
5.11 Schematic overview of two configurations of the sheet optic housing consisting of a plano concave spherical and meniscus lens. Since the plano concave spherical lens diverges lights, increasing the distance between the plano concave spherical and meniscus lens increases the laser beam width. An additional lens can be mounted to the sheet optic housing to manipulate the laser beam. Modified from LaVision GmbH [80]	44
5.12 Schematic of the test rig of Andritz Hydro located in Linz. The red cross and red arrows indicate the location of the turbine's runner and the flow direction, respectively	46
6.1 a) Chronological order of steps that are used to detect microbubbles. b) Example IPI image.	49
6.2 Image processing steps that are used to detect circular image disks. In chronological order: a) background removal, b) filter application, c) intensity threshold, d) edge detection, e) Hough gradient, f) Accepted circles after additional constraints. Figures 6.2a-6.2b and 6.2f have identical legends representing the intensity of the px in the figures. The range of the legend of Figure 6.2c is smaller due to the application of the intensity threshold. Finally, Figures 6.2d-6.2e show an equivalent legend with a maximum corresponding to the maximum value of the Canny edge detection.	51

6.3	Circle modifications performed on particles before applying a 2D FFT. If particles overlap (step 1), the overlap is removed (step 2). From the remains of these particles, the largest possible rectangle is drawn (step 3). This step is also performed when there is no overlap between particles. The edges are excluded from these rectangles as the FFT will find an additional spatial frequency coming from the gradient between the edges of the circles and the background. After these steps, a 2D Hann and a 2D FFT are applied.	52
6.4	Intensity profile from a) a dataset of microbubbles as a function of the distance from the laser beam centre in the x-direction, b) the laser beam as a function of its centre. From the dataset of microbubbles, the 70th percentile for different distances d from the beam centre in the x-direction is determined, from which a Gaussian distribution is obtained. The set of microbubbles does not entirely follow a Gaussian distribution caused by the shape of the laser beam.	54
6.5	Relation between the measurement volume and the diameter of microbubbles. The volume increases until microbubbles are saturated, starting at $D=140.2 \mu\text{m}$. The measurement volume goes to zero around the Nyquist limit, which is found at $D= 505.8 \mu\text{m}$. These values are found at the critical working point ($n_{ED}= 0.2234$, $Q_{ED}= 0.2293$, $AOA=20.3^\circ$) at $n=1000$ rpm, $DO=8.5$ mg/L and $H_s=7.30$ m and vary slightly for different datasets.	57
6.6	Concentration distribution of microbubbles measured at the critical working point ($n_{ED}= 0.2234$, $Q_{ED}=0.2293$, $AOA= 20.3^\circ$) at $n=1000$ rpm, $DO= 8.5$ mg/L and $H_s=7.30$ m. The curve shows the mean concentration of all iterations of the Monte Carlo algorithm, while the shaded area is the 5 to 95th percentile interval of these iterations.	58
7.1	Time-averaged DO concentration for different values of H_s at different runner speeds of the Francis 188 RD Type for a) condition 1: the presence of a cavitating vortex, b) condition 2: the absence of a cavitating vortex. The crosses indicate the inception point of gap cavitation for the different conditions. At higher H_s , a vacuum is created downstream of the turbine model, which causes a decrease in the DO concentration. This drop significantly increases once the inception point is reached.	61
7.2	Total microbubble concentration as a function of σ at the critical working point ($n_{ED}=0.2234$, $Q_{ED}=0.2293$, $AOA=20.3^\circ$) for a) $n=800$ rpm, b) $n=1000$ rpm, c) $n=1200$ rpm. The dashed lines represent the mean concentration obtained by integrating over all Monte Carlo simulations, while the shaded areas represent the standard deviation of this integration. For each curve, the inception point of gap cavitation is illustrated by the black symbols.	64
7.3	Microbubble concentration distribution obtained for different values of σ for the non-critical working point ($n_{ED}=0.2234$, $Q_{ED}=0.2293$, $AOA=20.3^\circ$) at $n=800$ rpm for a) $DO=3.5$ mg/L, b) $DO=5.5$ mg/L, c) $DO=8.5$ mg/L. All curves represent the mean concentration distribution obtained from the Monte Carlo simulation. The uncertainty of these distributions is not shown to enhance visibility.	65
7.4	Microbubble concentration distribution comparison for a) rope (presence of a cavitating vortex) and rope-free (absence of a cavitating vortex) conditions at $\sigma=0.187$, b) the rope-free (absence of a cavitating vortex) condition for different values of σ . All curves represent the mean concentration distribution obtained from the Monte Carlo simulation. The uncertainty in the concentration distributions is not shown in Figure 7.4b to enhance visibility.	66
7.5	Microbubble concentration distribution for a) the critical working point ($n_{ED}=0.2234$, $Q_{ED}=0.2293$, $AOA=20.3^\circ$), i.e., in the presence of a cavitating vortex, b) the non-critical working point ($n_{ED}=0.2234$, $Q_{ED}=0.1773$, $AOA=15^\circ$), i.e., in the absence of a cavitating vortex. The uncertainty in the concentration distributions is not shown to enhance visibility.	67
7.6	Comparison of the microbubble concentration distribution ($n=800$ rpm, $\sigma=0.342$) between an initial DO concentration of 3.5 mg/L and an air injection of a) 0.5% of Q_m , b) 1.0% of Q_m . All measurements were performed at the non-critical working point ($n_{ED}=0.2234$, $Q_{ED}=0.1773$, $AOA=20.3^\circ$). All curves illustrate the mean concentration distribution obtained from the Monte Carlo simulation, while the shaded areas represent 2-std	68

7.7	Comparison of the microbubble concentration distribution ($n=1000$ rpm, $\sigma=0.220$) between an initial DO concentration of 3.5 mg/L and an air injection of a) 0.5% of Q_m , b) 1.0% of Q_m . All measurements were performed at the non-critical working point ($n_{ED}=0.2234$, $Q_{ED}=0.1773$, $AOA=20.3^\circ$). All curves illustrate the mean concentration distribution obtained from the Monte Carlo simulation, while the shaded areas represent 2-std	68
7.8	Comparison of microbubble concentration between storage tank water and fresh tap water at the non-critical working point ($n_{ED}=0.2234$, $Q_{ED}=0.1773$ and $AOA=15^\circ$) at a) $n=800$ rpm, DO= 5.5 mg/L, b) $n=800$ rpm, DO= 8.5 mg/L	69
7.9	Concentration distribution of microbubbles measured at the beginning and end of a working shift under the same conditions ($n_{ED}=0.2234$, $Q_{ED}=0.2293$, $AOA=20.3^\circ$, $DO=5.5$ mg/L) at an H_s of a) 2.50 m, b) 5.50 m and c) 7.00 m. Here, the curves represent the mean concentration of all iterations of the Monte Carlo simulation, while the shaded area represents twice the std. For every value of H_s , a similar distribution of microbubbles is observed between the start and end of a shift, with a decrease in the mean value at the end of a shift. This effect is observed at a larger range of microbubble diameters for increasing H_s	71
7.10	Sigma break curves showing the normalised efficiency for different values of σ for different DO concentrations at the critical working point ($n_{ED}=0.2234$, $Q_{ED}=0.2293$, $AOA=20.3^\circ$) at $n=1200$ rpm. σ_i of gap cavitation for each DO concentration is marked with the black symbols.	73
7.11	Cavitation observed around the runner of a Francis RD-188 Type model at the critical working point ($n_{ED}=0.2234$, $Q_{ED}=0.2293$, $AOA=20.3^\circ$) at a) $\sigma=0.0481$, DO=3.5 mg/L, b) $\sigma=0.0396$, DO=3.5 mg/L, c) $\sigma=0.0501$, DO=8.5 mg/L, d) $\sigma=0.0410$, DO=8.5 mg/L	75
A.1	Application of a kernel filter to a greyscale image. The cover of the kernel filter on the original image is here limited to 2 locations.	89
A.2	a) Original image. The convolution of the original image and the 3x3 kernel filter is used to b) sharpen the image, c) blur the image with a box blur and c) blur the image with a Gaussian blur.	90
A.3	a) Two samples of a cosine function f with $\omega=1.0$ rad/s, and the multiplication of the Hann window w with f , indicated by the blue and orange curves, respectively. The red line indicates the time corresponding to the end of the first sample. b) Outcome of the FFT of the original function f and windowed function $w \cdot f$, indicated by the blue and orange lines, respectively. The amount of spectral leakage is significantly reduced by applying the Hann window.	90
A.4	a) Characterisation of a line in the image space by the parameters ρ and θ . A set of 4 different points on the line are shown. b) Parameter space representing the data points on the line in the image space.	91
A.5	Different points (x_i, y_i) on a circle with radius 1 and centre (0,0) shown in the a) image space and b) parameter space. In the parameter space, the points (x_i, y_i) are represented by a circle. The intersection of these circles represents the centre of the circle that is shown in the image space.	92
A.6	Visualisation of point (x_1, y_1) that is shown Figure A.5a for different radii in the parameter space. For every value of r , point (x_1, y_1) is represented by a different circle in the parameter space, resulting in a cone shape.	92
A.7	a) Fringe pattern ($f=0.05$ cycles/px) for a resolution of 200 by 100 px and b) corresponding spatial frequency retrieved from FFT analysis	93
A.8	a) Fringe pattern ($f=0.1$ cycles/px) for a resolution of 200 by 100 px and b) corresponding spatial frequency retrieved from FFT analysis	93
B.1	Average microbubble concentration distribution of all Monte Carlo simulations for a working point with characteristics $n_{ED}=0.2234$, $Q_{ED}=0.2293$, $AOA=20.3^\circ$ for a) $n=1000$ rpm, DO=3.5 mg/L, b) $n=1200$ rpm, DO=3.5 mg/L, c) $n=1000$ rpm, DO=5.5 mg/L, d) $n=1200$ rpm, DO=5.5 mg/L, e) $n=1000$ rpm, DO=8.5 mg/L, f) $n=1200$ rpm, DO=8.5 mg/L	95

B.2 Average microbubble concentration distribution of all Monte Carlo simulations for a working point with characteristics $n_{ED}=0.2234$, $Q_{ED}=0.2293$, $AOA=20.3^\circ$ for a) $n=1000$ rpm, $DO=3.5$ mg/L, b) $n=1200$ rpm, $DO=3.5$ mg/L.	96
---	----

List of Tables

1.1	Test conditions of different test facilities of Andritz Hydro	3
1.2	Differences in cavitation number for measurements performed on a Francis 350 type turbine model at different test locations of Andritz	4
3.1	Parameters and their definition used in the Hough gradient method [71]	22
5.1	Overview of the measurements performed during this study. The amount of air injected (measurement 3) is a function of the discharge at model scale (Q_m). All measurements, except for measurement 4, are performed with storage tank water, while measurement 4 is conducted with fresh tap water.	47
5.2	Operating conditions for the sigma break curves for $n_{ED}=0.2234$ and $Q_{ED}=0.2293$. The subscript m denotes the model scale.	47
6.1	Overview of the parameters constraining the number of microbubbles selected to determine the microbubble content. Here, a , b , x_{edge} and y_{edge} represent the centre coordinates of a circular disk and the px values of the x and y edges of the IPI images. α_{tf} denotes the tilt in the fringe pattern. Microbubbles that satisfy all constraints are used to estimate the microbubble content.	53
6.2	Overview of parameters and their uncertainty that are used to calculate the size and concentration of microbubbles.	56
7.1	Average DO concentration measured by the sensor positioned in the test rig for a reference point ($n_{ED}=0.2234$, $Q_{ED}=0.1773$, $AOA=15^\circ$, $DO=3.5$ mg/L) and different volumes of air injections.	68
7.2	Comparison of the water quality of storage tank and fresh tap water. The absence of NaCl only results in a reduction of Na, thereby increasing the hardness of the water (Ca).	69
7.3	σ_i of gap cavitation for both considered working points: measurement 1:critical working point ($n_{ED}=0.2234$, $Q_{ED}=0.2293$, $AOA=20.3^\circ$) and measurement 2: non-critical working point ($n_{ED}=0.2234$, $Q_{ED}=0.1773$, $AOA=15^\circ$) for different runner speeds and DO concentrations.	72

Nomenclature

Below a list of abbreviations and symbols is given. Both abbreviations and symbols will be defined the first time in the report. Unless stated otherwise, cartesian coordinates are used in this report.

Abbreviations

Abbreviation	Definition
AOA	Angle of attack
a.u.	Astronomical unit
BEP	Best efficiency point
CFD	Computation fluid dynamics
CL	Centerline
CMC	Critical micelle concentration
CRLB	Cramer-Rao Lower Bound
CSM	Cavitation Susceptibility Meter
cw	Continuous wave
DFT	Discrete Fourier Transform
DO	Dissolved oxygen
DPSS	Diode-pumped solid-state
FFT	Fast Fourier Transform
FT	Fourier Transform
FWHM	Full Width Half Maximum
fps	Frames per second
IMO	International Maritime Organisation
IPI	Interferometric Particle Imaging
LMS	Long range Microscopic Shadowgraphy
MPFT	Multi-Phase Flow Tunnel
MSI	Mie Scattering Imaging
NACA	National Advisory Committee for Aeronautics
\mathcal{O}	Order of magnitude
PSD	Power Spectral Density
PSF	Point Spread Function
P-Polarization	Perpendicular polarization
p.d.u.	Procedure defined unit
pt	prototype
px	Pixels
RD	Research and Development
SNR	Signal to Noise Ratio
Std	Standard deviation
S-Polarization	Parallel polarization
TWL	Tailwater level
TVC	Tip vortex cavitation
URN	Underwater Radiated Noise
ZOHWP	Zero-Order Half-Wave plate

Symbols

Symbol	Definition	Unit
A	Effective cross-sectional area of a laser beam	mm^2
A_{cs}	Cross-sectional area of a laser beam based on I_{th}	mm^2
A_s	Area of saturation	mm^2
a	Particle size	μm
a_p	Particle size	px
C	Chord length	m
C	Contrast	-
C_0	Normalised contrast	-
C_L	Lift coefficient	-
C_p	Pressure coefficient	-
$C_{p_{min}}$	Minimum pressure coefficient	-
C_s	Concentration of dissolved gas in the saturated surrounding liquid	kg/m^3
C_∞	Concentration of dissolved gas in the surrounding liquid	kg/m^3
c	Dissolved oxygen concentration	mg/L
c	Concentration of microbubbles	p.d.u
c_{sat}	Saturated oxygen concentration	mg/L
D	Aperture	mm
D	Bubble diameter	μm
D_a	Aperture	mm
D_i	Image disk size	mm
D_{max}	Maximum microbubble diameter	μm
$D_{max,I}$	Microbubble diameter from where saturation occurs	μm
D_{min}	Minimum microbubble diameter	μm
D_{min}	Minimum distance between the centres of two circles	px
$D_{min,I}$	Minimum microbubble that can be measured based on I_{th}	μm
D_{px}	Diameter of the particle image	μm
d	Distance to the laser beam centre	mm
d_p	Particle diameter	μm
dp	Inverse ratio of the accumulator resolution to the image resolution	-
$E_{S\parallel}$	Intensity of parallel polarised light w.r.t. scattering plane	a.u.
E	Specific energy	m^2/s^2
$E_{S\perp}$	Intensity of perpendicular polarised light w.r.t. scattering plane	a.u.
f	Shedding frequency	s^{-1}
f	Focal length	mm
f_f	Frequency	s^{-1}
f_p	Fringe frequency	px^{-1}
f_s	Sampling frequency of signal	px^{-1}
g	Gravitational constant	m/s^2
H	Henry's constant	s^{-1}/m^2
H	Net head of a flow	m
H_m	Model head	m
$H_{L,dt}$	Draft tube losses	m
H_s	Suction head	m
I	Intensity	a.u.
I_{BD}	Bit depth ratio	-
I_{max}	Maximum intensity	a.u.

Symbol	Definition	Unit
I_{min}	Minimum intensity	a.u.
I_{Th}	Intensity threshold	a.u.
\tilde{I}_0	Proportionality constant	$px^2 \mu m^{-2}$
\tilde{I}_s	Normalised intensity	$px^2 \mu m^{-2}$
K	Correlation factor relating the boundary layer thickness with the Reynolds number	-
L	Characteristic length scale	p.d.u.
L_b	Length of laser beam	mm
L_{max}	Cavity length	m
L_{px}	Size of a px	μm
l	Distance between collecting lens and out of focus plane	m
l_x	Distance between out-of-focus plane and image plane	m
M	Magnification	-
MB	Motion blur	μm
M_0	Magnification at $z_0=0$ mm	-
m	Refraction index ratio	-
N	Number of fringes	-
N	Number of samples	-
N_b	Number of microbubbles	-
N_{img}	Number of images	-
n	Rotational speed	rpm
n	Refractive index of the medium	-
n_{ED}	Non dimensional runner speed	-
P_h	Hydraulic power	W
P_m	Mechanical power	W
P_n	Noise power	dB
P_s	Signal power	dB
$p1$	Higher threshold for the Canny edge detection	-
$p2$	Accumulator threshold	-
p_a	Ambient pressure	Pa
p_c	Critical pressure	Pa
p_{g0}	Gas pressure at initial state	Pa
p_M	Pressure at point of interest	Pa
p_{loss}	Pressure losses in test rig	Pa
p_r	Pressure at reference point	Pa
p_v	Vapour pressure	Pa
p_∞	Local pressure	Pa
Q	Discharge	m^3/s
Q_{ED}	Non dimensional discharge	-
R	Bubble radius	μm
R_0	Initial bubble radius	μm
R_c	Critical radius	μm
R_{max}	Maximum radius of a particle image	px
R_{min}	Minimum radius of a particle image	px
Re	Reynolds number	-
r	Ratio between dissolved and saturated oxygen at a certain pressure	-
r	Radius of a circle	p.d.u.
r_0	Distance between the laser beam centre and the centre of a microbubble	mm
r_l	Radius of circle at a chosen intensity level	px
S	Surface tension coefficient	N/m

Symbol	Definition	Unit
S_1	Amplitude function for parallel polarised light	-
S_2	Amplitude function for perpendicular polarised light	-
St	Strouhal number	-
s_i	Inception location	m
T	Tensile strength	Pa
T	Torque	Nm
T	Wave period	s
T_w	Water temperature	°C
t_s	Shutter time	μs
U_{IPI}	Flow velocity	$\mu\text{m}/\mu\text{s}$
U_∞	Flow velocity	m/s
V	Measurement volume	cm^3
We	Weber number	-
x	Distance to laser beam center	mm
x_0	Location of laser beam center	mm
z	Height difference between in and outlet of turbine	m
z_0	Out-of-focus distance	mm
z_1	Distance between the lens and the focal plane	mm
α	Collection angle	-
γ	Percentage of dissolved oxygen at a certain pressure relative to saturated oxygen at atmospheric pressure	-
Γ	Circulation	-
γ_{st}	Surface tension	N/m
δ	Distance between the laser beam centre and the focal plane of the camera	mm
δ_b	Width of laser beam	mm
η_h	Hydraulic efficiency	-
η_m	Efficiency of the turbine model	-
$\eta_{m,max}$	Maximum efficiency of the turbine model	-
θ	Scattering angle	-
θ	Angle between x-axis and perpendicular line	-
κ	Constant of angular wavelength of scattered light with size	μm
λ	Wavelength of light	nm
λ_{px}	Wavelength of fringes in an image	μm
μ	Dynamic viscosity	Ns/m^2
ν	Kinematic viscosity	m^2/s
ρ	Density	kg/m^3
ρ	Perpendicular distance between a line and the origin	-
ρ_{hg}	Density of gas	kg/m^3
ρ_w	Density of water	kg/m^3
σ	Cavitation number	-
$\sigma_{D_{px}}$	Variance in particle diameter	μm
σ_f	Variance in sampling frequency	px
σ_i	Cavitation inception number	-
σ_{tm}	Cavitation number of a turbine model	-
$\sigma_{\eta,1}$	Cavitation number for 1% efficiency drop	-
τ	Contrast coefficient	-
τ_{res}	Characteristic time for diffusion	s
ϕ	Polarisation angle	-
χ_{PSF}	Width of Gaussian Point Spread Function	μm

Symbol	Definition	Unit
ω	Angular velocity	rad/s

1

Introduction

The impact of underwater radiated noise (URN) has gained increasing attention in recent years [1], [2]. URN in the seas is to a large extent caused by cavitation on ship propellers [3]. For years, lowering URN has been essential for naval vessels to avoid detection and threats [3]. More recently, the effects of URN on marine life have increased awareness among the International Maritime Organisation (IMO) [4]. The IMO has, therefore, revised its guidelines to minimise adverse effects on the vital functions of marine life [5]. Different approaches to reduce these effects have been suggested in these guidelines, focusing on the reduction of cavitation of ship propellers. To achieve this, a deeper understanding of the main driving forces behind this phenomenon is required. The knowledge gained by studying cavitation around ship propellers is not only relevant for the maritime industry but also gives further insight into cavitation observed in other industries, such as the hydraulic industry.

Cavitation is characterised by two processes, cavitation inception and dynamics [6]. The first process is defined by the formation of vapour bubbles due to a phase change of water from liquid to vapour [6]. This phase change can either be caused by a temperature increase or a pressure decrease. The first is referred to as boiling, whereas the latter is referred to as cavitation inception [7]. The second process, cavitation dynamics, describes the development of vapour bubbles. This includes the growth to their critical size, which depends on the local pressure [8]. Once these vapour bubbles travel to a region with a higher surrounding pressure, the bubbles can collapse [7], [9]. This collapse can result in noise and erosion damage on the material [10].

Flow properties, including the local pressure and the flow velocity, affect cavitation [7]. However, cavitation is also affected by water quality [11]. According to the National Oceanic and Atmospheric Administration [12], water quality is defined as the condition of water, including chemical, physical and biological properties. The first property includes the concentration of salts, nutrients, and dissolved oxygen (DO) [13]. Physical characteristics include the water temperature and turbidity, whereas the biological side is characterised by organisms, including algae and bacteria [13].

The size and concentration of microbubbles in a flow can be altered by the flow properties and the water quality [14]–[16]. Although these bubbles play a significant role in cavitation, the extent to which microbubbles affect cavitation is unclear. Relating the microbubble content to cavitation can be done experimentally by measuring microbubbles in a flow. Different measuring techniques exist to determine the microbubble content in a flow, including the Cavitation Susceptibility Meter (CSM), Long range Microscopic Shadowgraphy (LMS) and Interferometric Particle Imaging (IPI) [17]. The latter can measure microbubbles of $\mathcal{O}(10 - 100\mu m)$, which are the most important for cavitation [17].

1.1. Problem definition

This master's thesis is performed at Andritz, a company that focuses on different sectors, including the hydraulic industry. Within this industry, a wide range of hydraulic turbines exist, which includes Francis, Kaplan and Pelton turbines. More information regarding the main principles behind hydraulic turbines and their application can be found in Chapter 4. For all these different turbines, the designs are in a preliminary state optimised by Computational Fluid Dynamics (CFD) models. With these models, it is not only possible to visualise the pressure and loss distributions within the turbine but also to predict cavitation around a turbine. However, in a later stage model tests are performed for a more accurate identification of cavitation around the turbine and the turbine performance. These model tests are performed at different locations of Andritz, among which Linz has the largest test facility. At this location, the main focus lies on studying the performance of Kaplan and Francis turbines. In this study, the focus lies on studying cavitation around the latter.

Figure 1.1 shows a 3D rendering of the Francis Research and Development (RD) 350 Type model, designed by Andritz Hydro ¹. The conversion from radial inflow to axial outflow results in the rotation of the blades located inside the green part of the turbine. This results in the conversion from kinetic energy to mechanical energy [18]. The efficiency of this conversion can be hindered by cavitation [19]. At a later stage, cavitation can cause erosion damage on the blades of a turbine [20], as low-pressure regions found at these blades are favourable for cavitation [9]. To mitigate the effects of cavitation, cav-

¹Andritz Hydro is a company within Andritz that focuses on hydropower.

itation measurements are conducted to predict the behaviour around these blades more accurately.

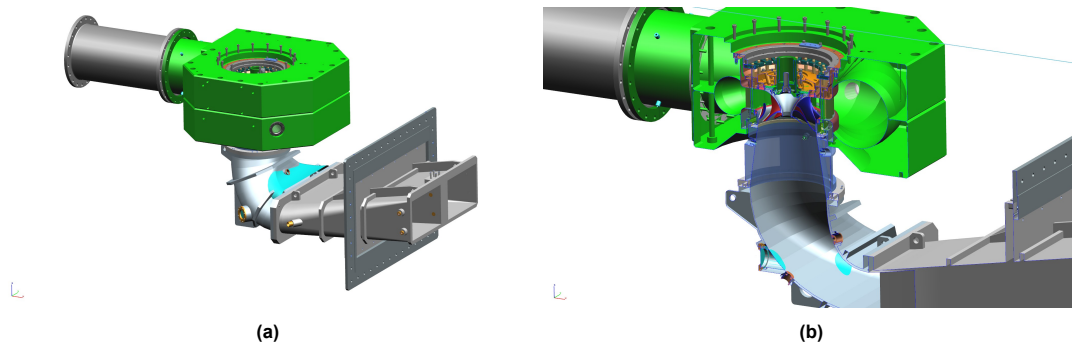


Figure 1.1: 3D render of a) a whole Francis Type 350 turbine model and b) the inside of a Francis 350 turbine model. Water enters the turbine in the grey cylinder in the top left. The radial inflow in the green block is converted to an axial outflow causing a rotation of the turbine blades.

Before the start of this study, cavitation experiments were conducted by Andritz Hydro at three test facilities located in Linz, Graz and Montreal. At every test location, an identical Francis RD 350-type turbine was positioned inside the test rig. This is a closed-loop test facility, in which the pressure, flow rate and oxygen level can be controlled. In general, cavitation measurements start at a high pressure inside the test rig, which is lowered until vapour bubbles are formed. This point, commonly known as the cavitation inception point σ_i is a parameter observed during these measurements. The second parameter relevant for Andritz Hydro is the point at which an efficiency drop of the turbine model of 1% is observed, also known as $\sigma_{\eta 1}$. More information regarding the procedure of model testing is described in Chapter 4.

Table 1.1 lists the test conditions for the different test locations during the cavitation measurements. Except for the oxygen (O_2) content and water temperature (T_w), the conditions are equal at different locations. Although the oxygen content in the test rig of Linz was only approximately 9% lower than that in the test rig of Graz, a larger deviation was observed in Montreal. Moreover, the water temperature in Graz strongly differs from that measured in Linz and Montreal. This was caused by a malfunction in the cooling system of the test rig in combination with a high environmental temperature as the measurements were conducted during the summer.

Table 1.1: Test conditions of different test facilities of Andritz Hydro

Test location	O_2 content (ppm)	T_w ($^{\circ}C$)
Graz	3.85	32.3
Linz	3.49	19.9
Montreal	5.25	22.3

For all facilities, the cavitation numbers at inception (σ_i), i.e. when the first vapour bubbles are observed visually, and at an efficiency drop of 1% ($\sigma_{\eta 1}$) were calculated and are listed in Table 1.2. It should be noted that for all test locations, the same definitions for σ_i and $\sigma_{\eta 1}$ were used. Moreover, no data on σ_i was available from the experiments conducted in Linz. From Table 1.2, it can be concluded that the σ_i is similar for Graz and Montreal, whereas larger differences can be found for $\sigma_{\eta 1}$. However, under equal test conditions, similar results in cavitation behaviour would be expected. Hence, it can be concluded that the differences in σ_i and mostly $\sigma_{\eta 1}$ must be caused by a parameter that was not considered in the study of Andritz. Since the population of microbubbles in a flow is considered to be one of the most important parameters for cavitation [11], [21], [22], the hypothesis has been stated that the differences in σ_i and $\sigma_{\eta 1}$ are caused by a difference in the population of microbubbles between the facilities.

Table 1.2: Differences in cavitation number for measurements performed on a Francis 350 type turbine model at different test locations of Andritz

Test location	σ_i	$\sigma_{\eta 1}$
Graz	0.242	0.179
Linz	-	0.195
Montreal	0.240	0.166

1.2. Relevance and research objective

One of the most important parameters that affect cavitation is the microbubble content in a flow. However, it remains unclear to what extent cavitation is influenced by microbubbles, as the amount of research on this topic is limited. Hence, this study aims to develop a better understanding of the role of microbubbles on cavitation. The role of flow parameters and water quality on microbubbles should be taken into account to assess the differences in σ_i and $\sigma_{\eta,1}$ measured at different test facilities. The main research question of this study following this objective is formulated as follows:

How do the size and concentration of microbubbles influence the cavitation behaviour, i.e. inception and dynamics, around the runner of a model of a hydraulic turbine?

This research question is supported by multiple subquestions, which are formulated as follows:

1. *How do flow parameters inside a test facility affect the size and concentration of microbubbles?*
2. *How do the bubble size and concentration affect cavitation inception?*
3. *How do the bubble size and concentration affect cavitation dynamics?*
4. *How and to what level does interferometric particle imaging give an accurate representation of the microbubble content relevant for cavitation inception and dynamics?*

These subquestions are partly answered by means of a literature study. The outcome of this study can be found in Chapters 2 and 3. The main research question of this master's thesis is answered by means of experimental work, which is performed at one of the test rigs of Andritz Hydro located in Linz. During these measurements, cavitation is observed around a model of the Francis RD-188 Type, while microbubbles are measured with the IPI technique. More information on this methodology can be found in Chapter 5.

1.3. Outline

The goal of this Master's thesis is to find a relationship between the size and concentration of microbubbles and cavitation around a hydraulic turbine model. This starts by defining the problem and the research's objective in Chapter 1. Thereafter, background information on cavitation is given in Chapter 2. Furthermore, background information on microbubbles and their role in cavitation can be found in this chapter. Chapter 3 describes the principles behind the IPI technique, that is used to measure these microbubbles. This also includes the different aspects of image processing and the uncertainty of IPI. Chapter 4 focuses on the main principles of hydraulic turbines and the procedures of model testing. Thereafter, Chapter 5 is dedicated to the methodology of this Master's thesis. This includes the calibration of the high-speed camera, which is used for recording microbubbles, as well as a description of the IPI setup. Furthermore, the test plan for the IPI measurements performed at Andritz is described here. Chapter 6 describes the different steps necessary to post-process the data retrieved with the IPI technique, including the estimation of the size and concentration of the microbubbles. Lastly, the results of this study are described in Chapter 7, followed by some final conclusions and recommendations for future work in Chapters 8 and 9, respectively.

2

Cavitation and microbubbles

This chapter describes the background theory behind cavitation and microbubbles. First of all, an introduction to cavitation is given in Section 2.1, followed by an overview of different flow parameters that are relevant for cavitation in Section 2.2. Section 2.3 gives more insight into microbubbles and describes the role of other parameters on these microbubbles. Finally, the role of microbubbles on cavitation inception and dynamics is discussed in Sections 2.4 and 2.5.

2.1. Introduction

Understanding the driving mechanism of cavitation is key to developing accurate models that can confidently predict this phenomenon. The outcome of these models can then contribute to a further understanding of the underlying principles of cavitation.

Cavitation is defined as the formation from liquid to vapour by decreasing the pressure below some critical value, called the vapour pressure. A transition from a liquid to vapour phase can also be achieved by an increase in temperature, which is referred to as boiling [10]. Both of these transitions are illustrated by Figure 2.1. This figure also illustrates a curve from the triple point T_r towards the critical point C . Here, T_r indicates at which temperature and pressure the three phases coexist in a substance, whereas C indicates the limiting temperature and pressure at which a substance can be in a liquid or vapour phase. After this point, the substance becomes supercritical.

Cavitation occurs in different forms. In general, three main types of cavitation can be distinguished: transient bubble, sheet, and vortex cavitation [6]. The appearance of these types of cavitation depends on various parameters. These include flow properties and water quality. Their role in cavitation is described in Sections 2.2-2.3.

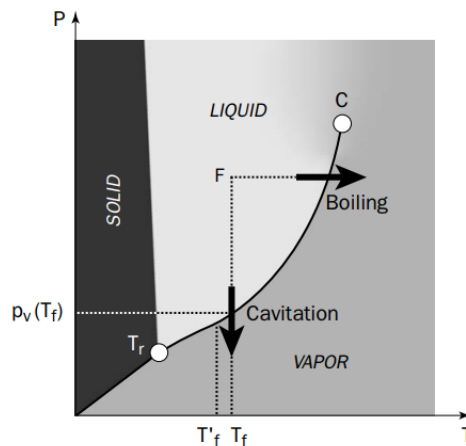


Figure 2.1: Phase diagram for water, indicating typical phase changes by increasing the temperature (boiling) and by decreasing the pressure (cavitation) [10].

2.2. Flow parameters

The degree of cavitation in a flow can be described by the non-dimensional cavitation number. This number relates the local pressure to the vapour pressure and the kinetic energy [10]:

$$\sigma = \frac{p_r - p_v(T)}{\Delta p} \quad (2.1)$$

Here, p_r is the pressure at the reference point, i.e., the local pressure and p_v is the vapour pressure. Different forms of Equation 2.1 exist and are applied, depending on the geometry of the body [23], [24]. For each form, a flow is cavitating if the following condition is satisfied [10]:

$$\sigma \leq \sigma_i \quad (2.2)$$

where σ_i is the cavitation number when vapour bubbles are formed, also known as the cavitation inception point [7]. This point is often numerically computed using the pressure coefficient C_P , a non-dimensional number used to describe the pressure along the surface of a geometry [6], [7]:

$$\sigma_i = -C_{p_{min}} \quad \text{with} \quad C_p = \frac{p_M - p_r}{\Delta p} \quad (2.3)$$

where $C_{P_{min}}$ and p_M are defined as the minimum pressure coefficient and the pressure at the point of interest. Equation 2.3 illustrates that the onset of cavitation occurs at low pressure regions, caused by high local velocities in the flow. Additionally, pressure drops can be caused by accelerations and oscillations of the flow. [10]. Another flow parameter influencing cavitation is the viscosity of the liquid. The importance of this parameter with respect to the inertia forces can be considered using the Reynolds number:

$$Re = \frac{U_\infty L}{\nu} \quad (2.4)$$

where U , L and ν are the fluid velocity, the characteristic length scale of the geometry and the kinematic viscosity of the fluid. The role of Re on cavitation inception is crucial for TVC [23]:

$$\sigma_i = KC_L^2 Re^n \quad (2.5)$$

where K and C_L are a correlation factor that relates the boundary layer thickness of the geometry with Re and the lift coefficient, respectively. It should be noted that the dependence of σ_i on Re depends on the separation zone of the geometry. For axisymmetric geometries, including hydrofoils, a large separation zone is developed resulting in a strong correlation between σ_i and Re . Depending on the water quality, the value of the coefficient n changes [25]–[27]. More information regarding the influence of water quality on TVC is given in Section 2.4.2.

After the formation of vapour bubbles, cavities start to develop. Due to instabilities in the flow, cavities will shed from the geometry, which is commonly observed for sheet cavitation [22]. The frequency at which shedding occurs can be defined with the Strouhal number [28]:

$$St = \frac{fL}{U_\infty} \quad (2.6)$$

where f and L are the shedding frequency and the length of the geometry, respectively. More information regarding shedding phenomena is given in Section 2.5.

2.3. Microbubbles

The formation of vapour bubbles does not only require low-pressure regions in the flow but also spots of weakness in the liquid where vapourisation can start, commonly known as nuclei [29]. These nuclei can be categorized as (micro)bubbles or pockets of gas trapped on surfaces, for example, on solid particles or walls [10], [29]. Although the concentration of solid particles in water is found to be much higher than of microbubbles [30], [31], these are considered not to have a dominant impact on the flow behaviour [32]. Hence, in this study, only the influence of microbubbles on cavitation is studied.

In literature, the term water quality is frequently used to discuss the role of microbubbles on cavitation [11], [33]. However, several factors characterise this term, which can be divided into physical, chemical, and biological categories [12]. Some examples of these factors falling into these categories are solid particles, salinity and dissolved oxygen, and algae, respectively. [13]. In this section, an introduction to bubble dynamics and the role of these parameters on microbubbles is given.

2.3.1. Bubble Dynamics

The shape of a bubble can be characterised by the non-dimensional Weber number, which relates the inertia in a flow to the surface tension [28]:

$$We = \frac{\rho U_\infty^2 D}{\gamma_{st}} \quad (2.7)$$

where D and γ_{st} denote the diameter of a bubble and the surface tension applied to a bubble. For $We \ll 1$, surface tension is dominant, causing a bubble to remain spherical, while $We \gg 1$ indicates that the inertia forces are dominant, causing an elongation in the bubble. Assuming that a bubble remains spherical, the growth of a bubble can be described with the non-linear second-order differential Rayleigh-Plesset equation [34]:

$$\underbrace{\rho \left(R\ddot{R} + \frac{3}{2}\dot{R}^2 \right)}_{\text{Inertia}} = \underbrace{p_v - p_\infty(t)}_{\text{Pressure difference}} + \underbrace{p_{g0} \cdot \left(\frac{R_0}{R} \right)^{3k}}_{\text{Non-condensable gas}} - \underbrace{\frac{2S}{R}}_{\text{Surface tension}} - \underbrace{4\mu \frac{\dot{R}}{R}}_{\text{Viscosity}} \quad (2.8)$$

where

- R is the bubble radius
- \dot{R} is the first order time derivative of R
- \ddot{R} is the second order time derivative of R
- $p_\infty(t)$ is the pressure of the surrounding liquid
- p_{g0} is the pressure of gas inside the bubble
- R_0 is the initial bubble radius
- k is the polytropic coefficient
- S is the surface tension coefficient
- μ is the dynamic viscosity

Here, the subscript 0 denotes the initial state of the bubble and $k=1$, as it is assumed that p_∞ is constant and the gas transformation is isothermal [10]. The pressure difference $p_v - p_\infty(t)$ indicates the closeness of the liquid pressure to the vapour pressure. Assuming that the effects of viscosity are negligible, the equilibrium state of a bubble ($\dot{R} = \ddot{R} = 0$) in both the initial state and outside this state can respectively be defined as:

$$p_{\infty 0} = p_{g0} + p_v - \frac{2S}{R_0} \quad (2.9)$$

$$p_\infty = p_{g0} \cdot \left(\frac{R_0}{R} \right)^3 + p_v - \frac{2S}{R} \quad (2.10)$$

Over time, a bubble can change in size as it travels to regions with changing local pressures, the exchange of gas between the surrounding liquid and the bubble and the effects of surface tension. First of all, the growth of a bubble is hindered by surface tension. Secondly, the change in bubble size as a result of a change in the liquid pressure can be determined by substituting Equation 2.9 into Equation 2.10, resulting in:

$$p_\infty = \left(p_{\infty 0} - p_v + \frac{2S}{R_0} \right) \cdot \left(\frac{R_0}{R} \right)^3 + p_v - \frac{2S}{R} \quad (2.11)$$

As the pressure of the surrounding liquid increases ($p_\infty > p_{\infty,0}$), a bubble will shrink (Figure 2.2). Here, $p_{\infty 0}$, R_0 , S , p_v are set to 1 atmospheric pressure (atm), 100 μm , 0.0728 N/m [35] and 2.339 kPa [36], respectively. It should be noted that the effects of gas diffusion are not considered here.

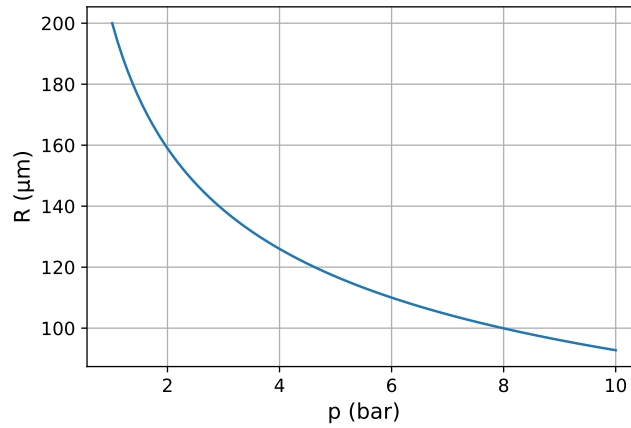


Figure 2.2: Change in bubble radius for different local pressures for an initial bubble size $R_0=100 \mu\text{m}$ and a water temperature $T=20^\circ\text{C}$.

Secondly, the exchange of gas between the surrounding liquid and a bubble can significantly change the size of a bubble. The diffusive equilibrium of a bubble and its surroundings can be defined by Henry's law [10]:

$$C_s = H p_g \quad (2.12)$$

where C_s and H denote the concentration of dissolved gas in the surrounding liquid and Henry's constant, respectively. In a non-equilibrium case, a bubble can grow or shrink depending on the gas content of the surrounding liquid, also known as C_∞ . For $C_\infty > C_s$ the size of a bubble increases, as gas is transported from the liquid to the bubble. In contrast, the opposite applies for $C_\infty < C_s$ [10]. If the effects of surface tensions are neglected, the characteristic time of diffusion can be described as follows [10]:

$$\tau_{res} = \frac{R_0^2}{2D} \cdot \frac{\rho_g}{C_s - C_\infty} \quad (2.13)$$

where ρ_g is defined as the density of the gas. In general, the characteristic time scale for a bubble to dissolve is in the order of seconds.

2.3.2. Critical bubble size and pressure

The equilibrium of a bubble, illustrated with Equation 2.10, takes the critical radius and critical pressure of a bubble into account as follows [10]:

$$R_c = R_0 \cdot \sqrt{\frac{3p_{g,0}R_0}{2S}} \quad (2.14)$$

$$p_c = p_v - \frac{4S}{3R_c} \quad (2.15)$$

To determine if the critical pressure of a bubble is close to the vapour pressure, the tensile strength applied to the liquid (T) is introduced:

$$T = p_v - p_c = \frac{4}{3} \frac{S}{R_c} \quad (2.16)$$

From Equation 2.16, it follows that bubbles with a larger diameter will have a critical pressure closer to the vapour pressure compared to small bubbles. As the pressure does not have to drop significantly below the vapour pressure to obtain the critical pressure, water is often referred to as weak water [22], [37], [38]. In contrast, water containing small microbubbles is referred to as strong water. Figure 2.3 illustrates the effects of different microbubble populations on the tensile strength. Here, the depleted case consists of small background microbubbles that are already present in a MultiPhase Flow Tunnel (MPFT), while the abundant case consists of large injected microbubbles. The sparse case is similar

to the abundant case but consists of fewer injected microbubbles. Figure 2.3 does not only show the relation between the tensile strength and the critical radius (Equation 2.16) but also the relation between the tensile strength and the concentration of microbubbles measured in the MPFT, showing a power law for all concentrations.

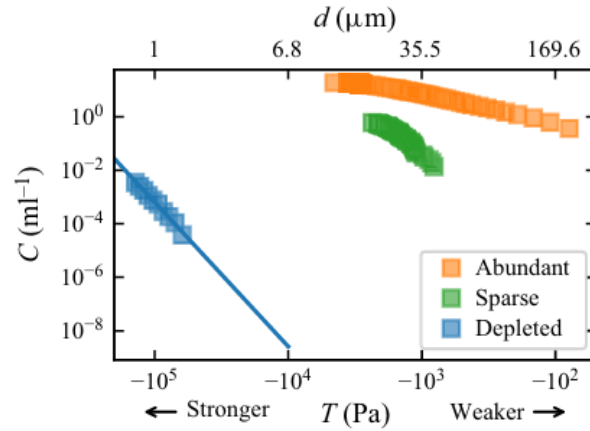


Figure 2.3: Relation between bubble size, tensile strength and bubble concentration for different nuclei populations. The depleted case was measured with Centerbody Susceptibility Meter (CSM), while the abundant and sparse cases were measured with Interferometric Particle Imaging (IPI) [22]

For a depleted case, i.e. small background microbubbles, the concentration of microbubbles has been determined as a function of the tensile strength in different MPFTs [39]–[41]. These background nuclei were measured with a Centerbody Susceptibility Meter (CSM), a technique based on the principles of a venturi. Since the pressure at the nozzle throat of the venturi changes with the flow rate [31], the size of nuclei that are measured will change as well. Decreasing the flow rate of the CSM makes it possible to measure the low concentration of background nuclei [42]. All measurements show a power law between the concentration of microbubbles and the tensile strength. Although there is some variation between the measured concentrations, Venning *et al.* [42] concluded that the concentration of small background microbubbles is invariant, as these can withstand dissolution.

2.3.3. Dissolved oxygen content

In MPFT's small background microbubbles are present in low concentrations [39]. Additional microbubbles can be added to a system by injection or by regulating the dissolved oxygen (DO) concentration [29], [33]. Increasing the DO concentration in MPFT's has shown to increase the microbubble content (Figure 2.4a), with a significant increase in small microbubbles (Figure 2.4b). Since the microbubble concentration increases as a result of an increasing DO concentration, the nucleation rate in the presence of a cavitating body, i.e., the number of vapour bubbles, increases as well [43]–[45]. Depending on the condition inside an MPFT, the DO concentration can vary. In general, the state of the water can be expressed as saturated or undersaturated of gas by means of the saturation level r . This ratio defines the likeliness of oxygen to either dissolve or leave the working fluid as a free gas, which is expressed as:

$$r = \frac{c}{c_{sat}} \cdot 100\% \quad (2.17)$$

where c and c_{sat} denote the DO concentration and saturated DO concentration at a certain temperature and pressure, respectively. Here, $r < 100\%$ indicates that the water is undersaturated. Figure 2.4c shows the bubble concentration for different saturation levels over a time window of approximately one week. Since the water is undersaturated, gas trapped in the bubbles will diffuse, causing a decrease in bubble concentration [39]. This is not entirely visible in Figure 2.4c due to a difference in tunnel conditions, such as the DO content, over the range of measurements

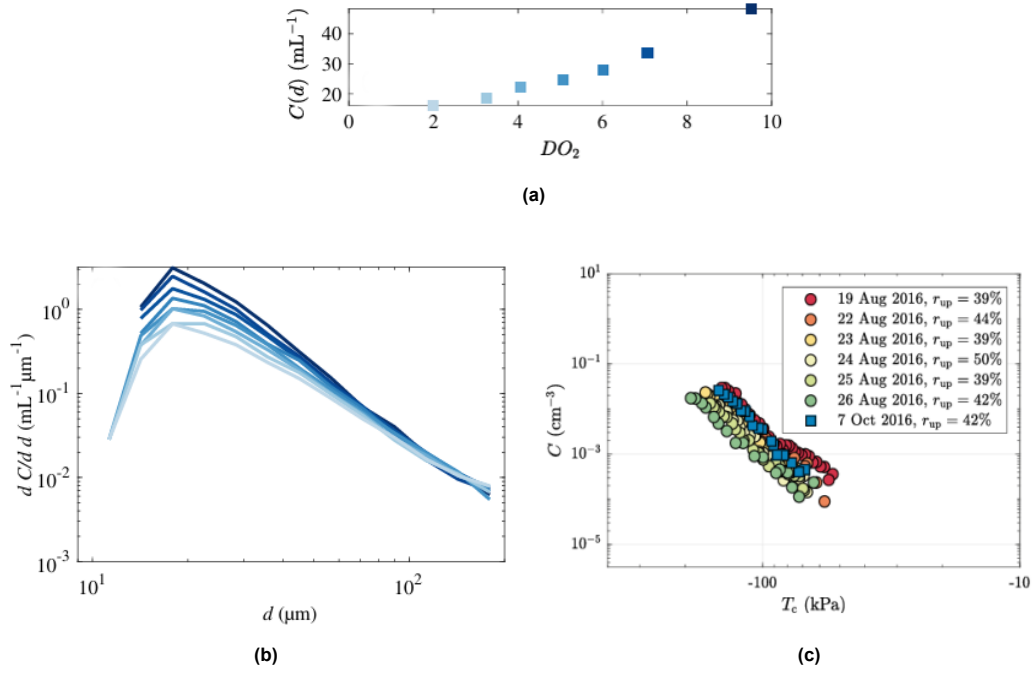


Figure 2.4: Relation between DO content and a) bubble concentration and b) corresponding size distribution for a tunnel condition $p=77$ kPa and $U=7$ m/s [33]. c) Bubble concentration as a function of DO content in a closed tunnel with operating conditions $p=50$ kPa, $U=7$ m/s and $\gamma=30$ -39% [39]

2.3.4. Surface tension

Since the cohesive forces between water molecules are strong, the surface tension of water, approximately 72 mN/m at a temperature of 20°C, is relatively high compared to other substances [46]. Decreasing the surface tension of water will disrupt the cohesive forces, allowing larger microbubbles to form [7]. Some substances, including surfactants and salts, can decrease the surface tension of water [46]–[48].

Surfactant molecules consist of a lyophobic tail and a lyophilic head, making it possible to gather at interfaces such as air-water interfaces, thereby disrupting the bonds between water molecules [49]. At high concentrations, these molecules can form a micelle, thereby enclosing one substance from the other substance [49]. The effects of surfactants on the surface tension are illustrated in Figure 2.5a. Here, C_{20} and CMC denote the surfactant concentration at a 20% reduction of γ and the critical micelle concentration, respectively. Whereas a significant drop in the surface tension is observed at low concentrations of a surfactant, the surface tension remains constant after the development of micelles. Although salts can also decrease the surface tension of water, the effects are only observed at large concentrations of salt in the water, as illustrated in Figure 2.5b. Here, the surface tension of American Society for Testing and Materials (ASTM) D1141 water, serving as a substitute for ocean water containing no organic materials, was used.

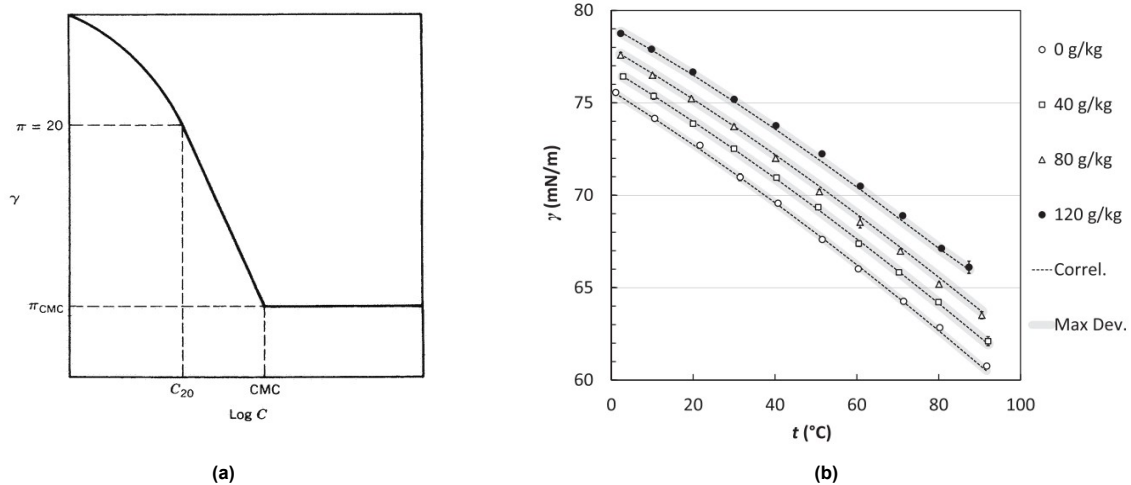


Figure 2.5: a) Relation between the surface tension of water and the concentration of a) a surfactant [49], b) salts [50]. Here, C_{20} and CMC denote the surfactant concentration at a 20% reduction of the surface tension and the critical micelle concentration, respectively.

2.3.5. Viscosity

The transfer of gasses between water and microbubbles is influenced by the viscosity of water, which can be altered by the addition of other substances to water. Increasing the viscosity of water will increase the holdup of gasses inside the water, thereby hindering the growth of bubbles. Consequently, smaller bubbles will be measured in a flow [51].

2.4. Effects of microbubbles on cavitation inception

In this section, the effects of microbubbles on cavitation inception are described. First of all, the activation rate is discussed (Section 2.4.1), followed by the change in the cavitation inception point (Section 2.4.2) and the change in inception zone and cavity length (Section 2.4.3).

2.4.1. Activation rate

Cavitation can be initiated by microbubbles in low-pressure regions below the vapour pressure of a geometry [52]. The activation rate, which is defined as the number of vapour bubbles observed around a geometry, shows a strong correlation with the microbubble content in a flow. Figures 2.6a and 2.6b show the activation rate per unit diameter of microbubbles measured around a sphere for different cavitation numbers for a depleted (small background microbubbles) and an abundant (additional seeding of microbubbles) case, respectively. For both cases, an increase in the activation rate is observed as the pressure around the geometry is decreased, thereby enhancing the growth of microbubbles. Hence, the activation rate will increase since larger microbubbles are less stable than smaller ones. Moreover, the activation rate differs by several orders of magnitude between a depleted and abundant case, as more and larger microbubbles are present in the flow in the abundant case, which can act as weak spots in the liquid.

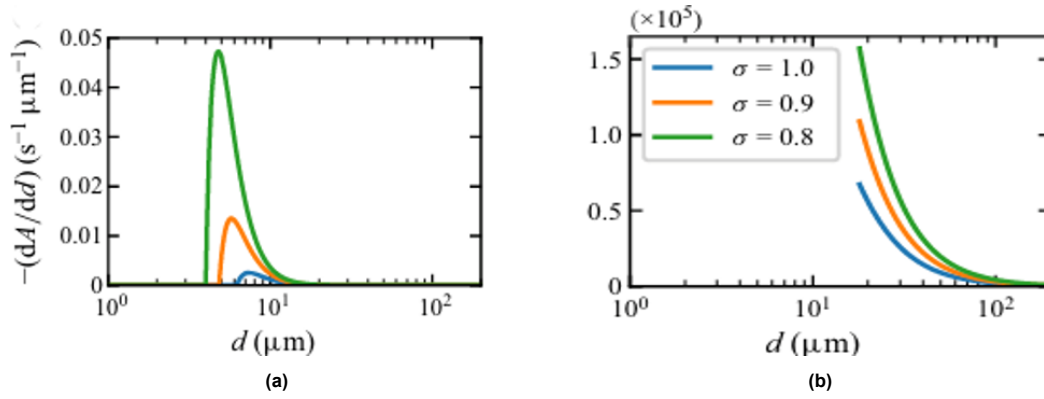


Figure 2.6: Activation rate A per unit diameter as a function of the nuclei diameter in a) depleted water and b) abundant water for different cavitation numbers. For both cases, the blue, orange and green curves represent a σ of 1.0, 0.9 and 0.8, respectively. [53]

2.4.2. Inception condition

Although the microbubble content is considered one of the most important parameters influencing cavitation, the role of the microbubble content on the inception point σ_i for different forms of cavitation remains unclear. However, for TVC, a relation between the microbubble content and the inception point σ_i was found by Arndt *et al.* [11]. For weak water, i.e., water containing small background microbubbles σ_i scales with $C_L^{0.35}$ (Equation 2.5), which is in accordance with Fruman *et al.* [25] and Maines *et al.* [27]. In contrast, for strong water, i.e., water containing a high concentration of large microbubbles, σ_i scales with $C_L^{1.4}$. This implies that the inception of TVC is delayed in water containing small concentrations of small microbubbles.

2.4.3. Inception zone

For axisymmetric bodies, the microbubble content in a flow does not seem to affect the inception zone of the body [54]. This is illustrated in Figure 2.7a for both a mono ($\mathcal{O}(100\mu\text{m})$) and polydisperse concentration ($\mathcal{O}(10 - 100\mu\text{m})$) of microbubbles around a National Advisory Committee for Aeronautics (NACA) 0012 hydrofoil. Here, L_{max}/C and s_i/C denote the ratio between the cavity length of TVC and the chord length of the foil and the inception location and the chord length of the foil, respectively. For both populations, the maximum cavity length is observed at $s_i/C=0$, indicating the minimum pressure region of the geometry [54]. In contrast, the cavity length and the inception zone on the geometry are significantly increased by the cavitation number (Figure 2.7b), as a decrease in the local pressure is favourable for activating vapour bubbles in the flow.

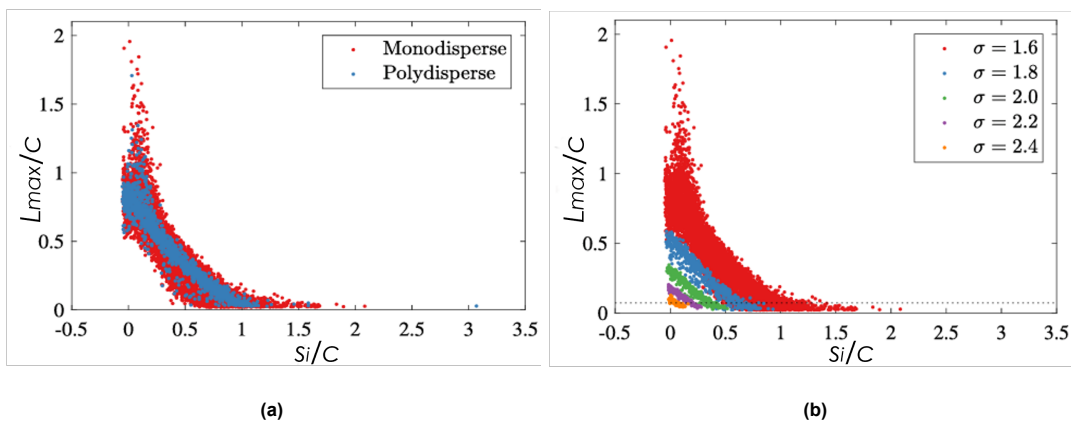


Figure 2.7: Relation between inception location s_i/c and cavity length L_{max}/c of TVC for different a) nuclei populations and b) cavitation numbers σ . [54]. The mono and polydisperse populations refer to microbubbles in the order of $\mathcal{O}(100\mu\text{m})$ and $\mathcal{O}(10 - 100\mu\text{m})$ in the liquid.

2.5. Effects of microbubbles on cavitation dynamics

In this section, the role of microbubbles on cavitation dynamics is discussed. First of all, the role of microbubbles in the general dynamics of sheet cavitation is described (Section 2.5.1). Thereafter, the role of microbubbles in the periodic shedding of sheet cavities is described in Section 2.5.2.

2.5.1. Dynamics of sheet cavitation

As discussed in subsection 2.1, different types of cavitation can occur, such as TVC, bubble and sheet cavitation. The occurrence of these types of cavitation depends not only on the geometry and flow parameters but also on the concentration of microbubbles. The role of microbubbles on sheet cavitation around a NACA 0015 hydrofoil was studied by Venning *et al.* [22]. The observed sheet cavity around the foil for both a depleted and abundant case of microbubbles for $\sigma=0.55$ is illustrated in Figure 2.8. For a depleted case, a series of bubbles is formed around the surface of the hydrofoil due to strong adverse pressure gradients in the transition zone between a laminar and turbulent flow [22]. In contrast, for the abundant case, larger and separated bubbles are observed as the leading edge of the hydrofoil is broken up by a continuous supply of activated microbubbles [22].

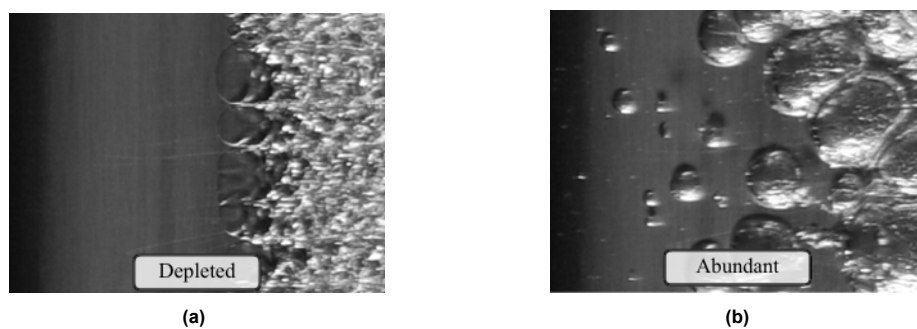


Figure 2.8: Illustration of the leading edge of a cavitating hydrofoil at a constant $\sigma=0.55$ for a) a depleted case and b) an abundant case. For the depleted case, glassy spanwise cells indicate the presence of a laminar separation bubble. For the abundant case, many nuclei activations are visible along the span, growing separately [22].

2.5.2. Periodic shedding

Sheet cavitation sheds due to the unsteadiness of the flow caused by low-pressure regions that fill with vapour as a result of separated shear layers [55]. The shedding of this form of cavitation depends on the angle of attack (AOA) of the geometry and the cavitation number (Figure 2.9).

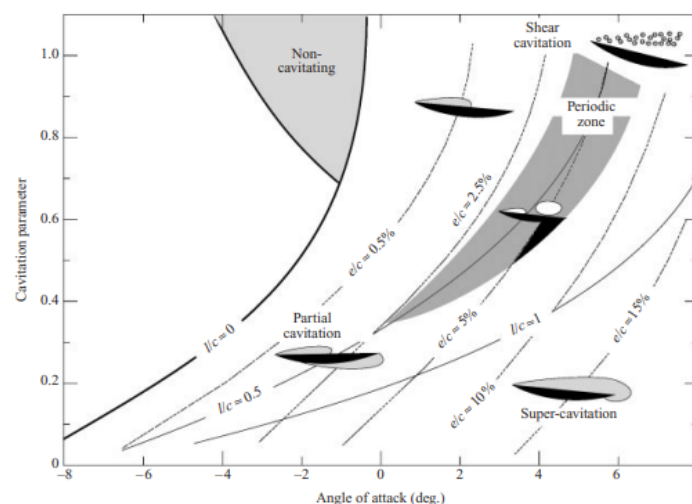


Figure 2.9: Cavitation regimes for the upper side of a plano-convex hydrofoil for $Re=2000$. Periodic shedding of sheet cavitation is observed in the periodic zone, characterised by the angle of attack and the cavitation number.

The periodic shedding of sheet cavitation can be driven by a re-entrant jet and shockwaves [56], depending on the cavitation number [22]. Although periodic shedding mainly driven by the re-entrant jet is observed at high cavitation numbers, while the role of shockwaves becomes more dominant at lower cavitation numbers [57], [58], periodic shedding can also be driven by a combination of these factors for some geometries. For different geometries, the characteristic frequency of periodic shedding lies around $St=0.2$ [22], [56], but can be altered by the microbubble content [22]. This holds for both the shedding frequency of sheet cavitation due to the formation of the re-entrant jet and shockwaves [22], [53].

The different physical processes of periodic shedding can be characterised by a space-time diagram, illustrated in Figures 2.10a and 2.10b for a depleted and abundant population of microbubbles respectively. Here, the blue, green, orange and red curves represent the cavity extension, the re-entrant jet region, the shockwave regime and advection, respectively. The purple dotted lines indicate the time shots used in the measurements of Brandner *et al.* [53]. From Figures 2.10a and 2.10b, it can be concluded that the shedding cycle of sheet cavitation is increased by the abundant population of microbubbles, mainly caused by the formation of a second shockwave. This second wave causes large-scale condensation and regrowth along the span of the hydrofoil. In the abundant case, a continuous supply of microbubbles acting as nuclei causes a growth of the cavity developed at the leading edge of the hydrofoil.

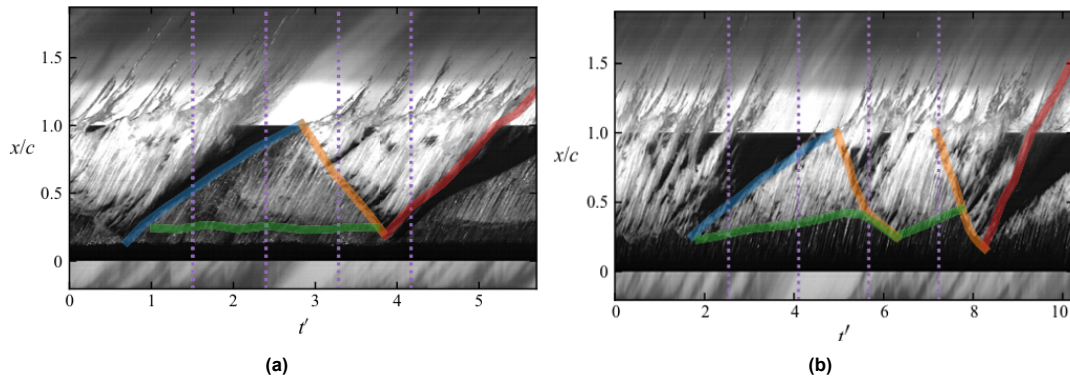


Figure 2.10: Space-time diagram for a) a depleted and b) an abundant population of nuclei. Snapshots are made at midspan, $z/b=0.5$, of the NACA0115 hydrofoil, and the flow is from bottom to top. The purple dotted lines indicate the time points of the snapshots. The blue, green, orange and red lines indicate the extension of the cavity, region of the re-entrant jet, the shockwave regime and advection, respectively [22]

3

Interferometric Particle Imaging

In this chapter the theoretical background behind measuring microbubbles is given. First of all, an overview of current measurement techniques is given in Section 3.1. Thereafter, the theoretical background behind IPI is described in Section 3.2, followed by an overview of the different steps that are taken to process IPI images in Section 3.3. Finally, the uncertainty of IPI is described in Section 3.4.

3.1. Introduction to measuring techniques

The methods available for assessing the bubble content in a liquid can roughly be categorised into two groups: acoustic and optical measurement techniques [31]. A commonly used acoustic measurement technique to measure microbubbles in a flow is the CSM [39], [59]. Optical methods include techniques such as Holography, Shadowgraphy and IPI [31], of which the latter is a promising technique for measuring microbubbles that are most relevant for cavitation [17].

The selection of a technique depends on the research's objectives, as each method possesses varying capabilities in detecting bubbles. Figure 3.1 shows the range of bubble size and concentration that can be measured with three different techniques: CSM, IPI and Long-Range Microscopic Shadowgraphy (LMS). The first technique makes use of a venturi, where the pressure in the throat can be controlled by regulating the flow rate [31]. Decreasing the flow rate makes it possible to measure the low concentration of small background microbubbles, as shown in Figure 3.1. On the contrary, LMS can measure much larger and higher concentrations of microbubbles. With this technique, microbubbles are illuminated resulting in a shadow projected onto the camera [60]. The range of microbubbles that can be measured with LMS depends on the image resolution and the relative level [61], [62]. Although the principles behind this technique are simple, the measurements can become complex if the light source, object and camera are not aligned. The third measurement technique shown in Figure 3.1 is IPI, also known as Mie Scattering Imaging (MSI). This technique is based on the principles of scattering light on a transparent bubble, resulting in a light pattern [31]. This light pattern is not only characterised by the light source itself but also by different parameters of the set-up, constraining the size of bubbles that can be measured [17], [31]. The typical size of microbubbles that can be measured with IPI ($10\text{-}100\mu\text{m}$) is most relevant for cavitation [17] and is therefore the technique used in this study.

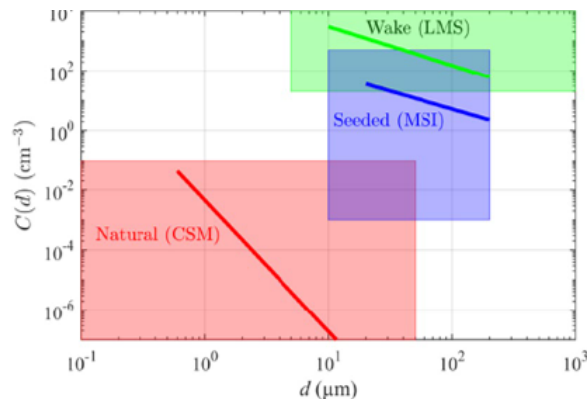


Figure 3.1: Nuclei concentration, C , and diameter, d , ranges for three different measuring techniques: red, blue and green region indicating Cavitation Susceptibility Meter (CSM), Mie Scattering Imaging (MSI) and Long-Range Microscopic Shadowgraphy (LMS). The lines represent the measurements carried out in the Australian Maritime College (AMC) tunnel [33]

3.2. Principles of Interferometric Particle Imaging

This section focuses solely on the principles behind IPI, starting with an explanation of the setup (Section 3.2.1). Thereafter, the theory and limitation of this technique are described in Sections 3.2.2 and 3.2.3.

3.2.1. General arrangement

A general arrangement used for IPI measurements is illustrated by Figure 3.2a. The setup involves a light source (laser), camera and optionally sheet optics to change the shape of the laser beam [31]. The laser is used to illuminate particles, which are recorded by the camera with a lens, referred to as the collecting lens (Figure 3.2a). Microbubbles can be positioned both in and outside of the focal plane of the camera. In the first case, these bubbles appear as illuminated dots, known as glare points, in the image plane (at a distance L from the collecting lens) as a result of reflected and refractive light [63]. Measuring the distance between two glare points, which increases with increasing bubble sizes, indicates the diameter of the bubble of interest. However, this method becomes more complex for smaller bubbles [64]. In the second case, a microbubble is positioned at a distance I_x out of the image plane (Figure 3.2a) and positioned at a distance I from the collecting lens. Examples of fringe patterns for different microbubble sizes are illustrated in Figure 3.2b. It can be concluded that the density of fringes increases with increasing bubble size. Additionally, the collection angle α , which defines the boundaries of the collecting lens (Figure 3.2a), is a significant parameter influencing the fringe density. Another parameter important for IPI is the scattering angle θ , which is the angle between the laser and the camera, as it influences the brightness and steadiness of the fringe pattern.

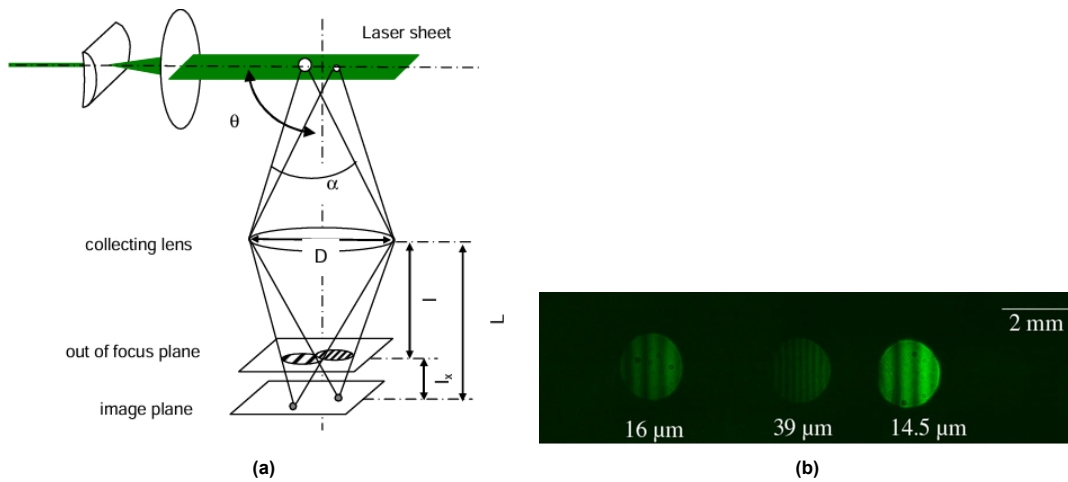


Figure 3.2: a) General arrangement of an IPI configuration showing the main parameters of the setup [31] b) out-of-focus image for different bubble sizes [17]

3.2.2. Mie Scattering

IPI relies on the principles of Mie scattering, which describes the scattering of light by spherical particles [17]. When a laser illuminates a transparent bubble (Figure 3.2a), the light can scatter in infinite ways. Figure 3.3a shows two of these possibilities. Here, the red and blue lines indicate the reflection and refraction of light under different angles θ with the centre line of the bubble. A combination of these waves results in bright and dark regions as a result of in-phase and out-of-phase waves, respectively. This results in a fringe pattern, which can be described using the Lorenz-Mie theory [17].

The main principles of this theory rely on parameters that are defined in Figure 3.3b. Here, the polarisation angle ϕ is defined as the angle between the polarisation of the laser and the camera. Light from the laser propagating along the x-axis can scatter in the parallel plane ($\hat{e}_{S\parallel}$), perpendicular plane ($\hat{e}_{S\perp}$) or a combination of them. The intensity of light in these planes depends not only on the intensity of the laser (E_i) but also on ϕ and θ [17]. This is because a perpendicular polarisation ($\phi=90^\circ$) results in a higher brightness than parallel polarisation ($\phi=0^\circ$), and the intensity of scattered light, indicated with the green area (Figure 3.3b), is a function of θ . For a spherical and transparent bubble, this results in the following relation between the intensity of light in the parallel ($\hat{E}_{S\parallel}$) and perpendicular ($\hat{E}_{S\perp}$) plane and these parameters [65]:

$$\begin{bmatrix} E_{S\parallel} \\ E_{S\perp} \end{bmatrix} = E_i \frac{e^{ip}}{-ip} \begin{bmatrix} S_2(\theta) & 0 \\ 0 & S_1(\theta) \end{bmatrix} \begin{bmatrix} \cos(\phi) \\ -\sin(\phi) \end{bmatrix} \quad (3.1)$$

where S_1 and S_2 represent amplitude functions describing an infinite sum of scattering options of light that is parallel and perpendicular polarised, respectively [17].

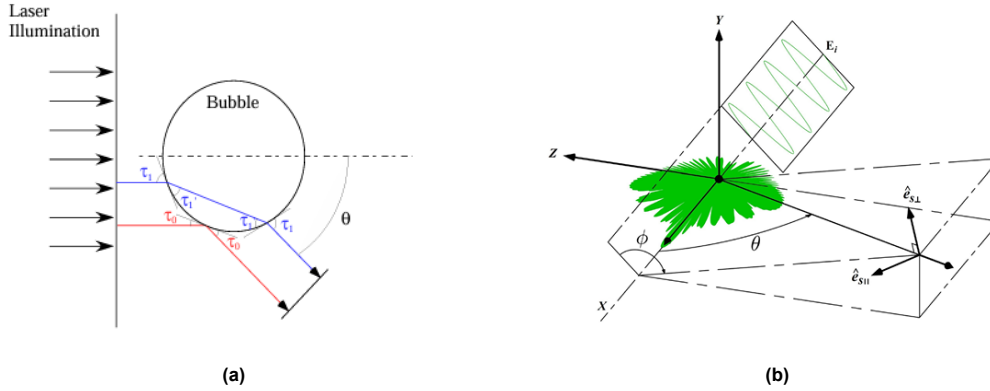


Figure 3.3: a) Possible ways the light from a laser can scatter on a spherical transparent bubble. The red and blue lines indicate reflected and refracted light, respectively [63] b) Overview of the different parameters that are used in the Mie Scattering theory. The light from a wave, E_i , propagating along the x -axis is scattered by a bubble in the origin. The green plane indicates the logarithmic intensity variations for varying scattering angles θ [17]

Although the intensity of light scattered in the parallel and perpendicular plane can be determined for every value of ϕ and θ , it is not analytically feasible and time intensive to solve S_1 and S_2 . However, Méès *et al.* [31] proposed a method to relate the fringe pattern to the diameter of a bubble, which does not require the solutions to S_1 and S_2 , as it only requires parameters of the IPI setup. This starts by relating the size of a bubble as seen on the camera to the out-of-focus distance and the aperture of the camera, also known as the collecting lens (Figure 3.2a):

$$a = D_a \frac{L-l}{L} = D_a \frac{l_x}{L} \quad (3.2)$$

where D_a is the aperture of the camera. Additionally, it can be concluded that the fringe frequency of a particle follows from the size of the particle and the number of fringes observed in the particle:

$$f_p = \frac{N}{D_{px}} \quad (3.3)$$

where f_p , N and D_{px} are the fringe frequency of a particle, the number of fringes and the image diameter of a particle. The fringe spacing, inversely proportional to N , can then be written as:

$$\Delta\theta = \frac{\alpha}{N} = \frac{\alpha}{D_{px} f_p} \quad (3.4)$$

According to Méès *et al.* [31], the actual diameter of a bubble is approximately inversely proportional to $\Delta\theta$:

$$d_p = \kappa \frac{1}{\Delta\theta} = \frac{\kappa D_{px} f_p}{\alpha} \quad (3.5)$$

where κ is a constant of angular wavelength of scattered light. For measurement in the absence of walls and bubbles with a refractive index ratio m , κ is derived from geometrical optic considerations as follows [31]:

$$\kappa = 2\lambda \cdot \left(\cos\left(\frac{\theta}{2}\right) + \frac{m \cdot \sin\left(\frac{\theta}{2}\right)}{\sqrt{m^2 - 2m \cdot \cos\left(\frac{\theta}{2}\right) + 1}} \right)^{-1} \quad (3.6)$$

where λ is defined as the wavelength of the laser. It should be noted that Equation 3.6 can only be used for $20^\circ \leq \theta \leq 70^\circ$. For scattering angles that do not fall in this range, κ can be calculated using

the principles of Mie scattering, which includes calculating S_1 and S_2 . A method to determine κ using this theory was proposed by Boucheron *et al.* [66], which consists of dividing the Mie response by the number of fringes in a particle for a collection angle near the scattering angle for a certain laser wavelength. Applying this method to different bubble diameters, results in a relation between κ and the bubble diameter (Figure 3.4). Here, the obtained values for parallel and perpendicular polarisation are indicated with the blue and black curves, respectively. A polynomial fit of these curves is illustrated with the pink and red curves, respectively. It can be concluded that the deviation in κ is largest for small diameters ($D \leq 40 \mu\text{m}$) and the unsteadiness in κ is larger for perpendicular polarisation. A similar trend in κ was determined for $\lambda=532 \text{ nm}$ and $\theta=90^\circ$ by Russell *et al.* [17], showing large deviations for bubbles with $D \leq 30 \mu\text{m}$. The uncertainty in bubble diameter as a result of the uncertainty in κ becomes negligible for bubble large bubble diameters [17].

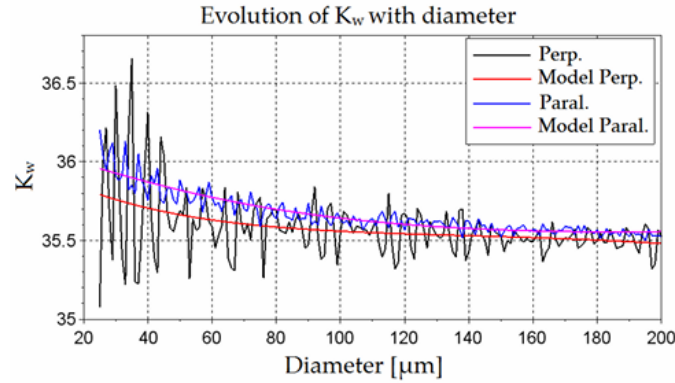


Figure 3.4: Relation between calibration constant κ for $\theta=85^\circ$ and bubble diameter. The black and blue lines represent the derived values for κ of the perpendicular and parallel scattering plane over the entire range of bubble diameters, respectively. The red and pink curves represent a polynomial fit of the black and blue lines, respectively. [66]

3.2.3. Limitations of IPI

Although IPI is a simple method to measure microbubbles, there are some limitations to this technique related to the size of microbubbles and the detection of microbubbles. First of all, the range of microbubble diameters that can be measured with IPI is constrained by the number of fringes and the Nyquist frequency. The minimum bubble diameter depends on the number of detectable fringes in a bubble image, which is approximately two. This corresponds to a fringe frequency of $2/D_{px}$ [67]. Substitution into Equation 3.5, results in:

$$D_{min} = 2 \frac{\kappa}{\alpha} \quad (3.7)$$

The maximum bubble diameter that can be measured with IPI is constrained by the Nyquist frequency, which is the highest spatial frequency that can be sampled without aliasing [63]. Since the Nyquist frequency is half of the sampling frequency [68] and the size of the images is measured in pixels (px), the Nyquist frequency is set to $1/2 \text{ px}$. Substitution into Equation 3.5 results in:

$$D_{max} = \frac{1}{2} \frac{\kappa D_{px}}{\alpha} \quad (3.8)$$

Equations 3.7 and 3.8 show that the range of microbubble diameters which can be measured with IPI is strongly related to the collection angle. This is because the number of fringes in a particle, which depends on the collection angle (Figure 3.5), that can be detected by the camera is fixed. Since the number of fringes increases with increasing collection angle, the upper limit of the camera is reached at smaller bubble diameters. Hence, a larger range of bubbles can be measured at smaller collection angles. However, the downside of a small collection angle is a reduction in accuracy [63].

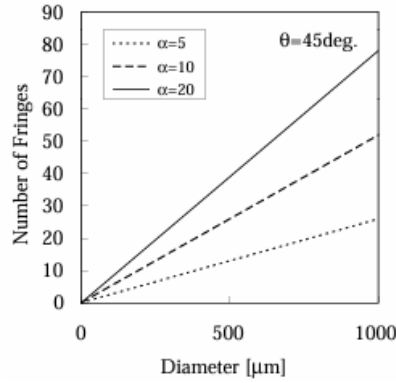


Figure 3.5: Correlation between the number of fringes and the bubble diameter as a function of α for $\theta=45^\circ$

The other limit of IPI relates to the detection of microbubbles, which can be hindered by different factors in an image. First of all, a large number of microbubbles or other particles can result in overlapping regions, resulting in an interference of multiple (fringe) patterns [69]. An example of the interference of multiple fringe patterns is illustrated in Figure 3.6a. Due to the interference, the detection of individual fringe patterns becomes more difficult. Nonetheless, these individual fringe patterns can still be analysed and related to the correct bubble images by only considering a part of the microbubble without overlap [67]. Next, some microbubbles have a tilt in the orientation of their fringe pattern due to the interference of scattering light of other microbubbles [67], [69]. Furthermore, small particles located near microbubbles can block parts of the fringe pattern (Figure 3.6c) and can even cause a hologram on the bubble image. Since the signal of such a hologram is stronger than the fringe, it is impossible to determine the size of the microbubble [67].

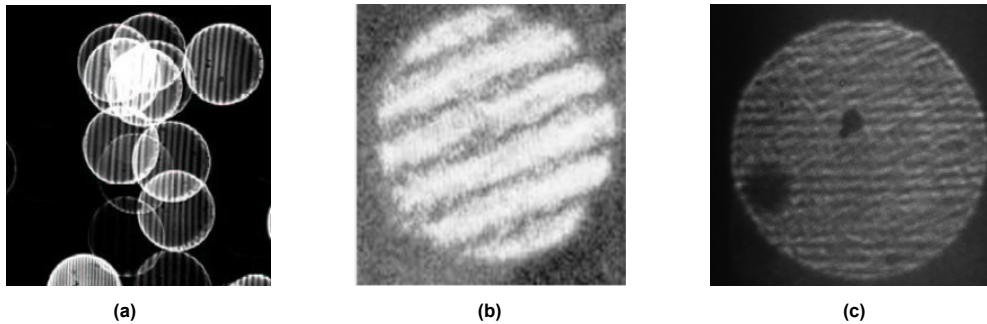


Figure 3.6: Out-of-focus images of microbubbles illustrating a) overlapping regions causing interference of fringe patterns [69], b) a distorted fringe pattern due to scattering of light from other microbubbles [69], c) distortion in a fringe pattern caused by a small particle.

3.3. Image processing

To determine the size of microbubbles measured with IPI, the IPI images need to be post-processed. This process involves the use of filters, the Hough Gradient method and the application of the Fourier Transform (FT).

In this study, a Gaussian kernel filter and 2D Hann filter are used to reduce the noise in the IPI images and to reduce the spectral leakage in the power density spectrum (PSD) obtained from the FT. More information regarding the principles of these filters can be found in Section A.1. The Hough gradient method is used to detect the microbubbles, thereby obtaining the centre and image diameter of the microbubbles. This method is applied using the *HoughCircles* function inside the *OpenCV* library, based on the principles of the Hough Gradient method described by Duda *et al.* [70]. More details on these principles can be found in Section A.2. The parameters used in the *HoughCircles* function are listed in Table 3.1. Here, dp , p_1 and p_2 need some further explanation. First of all, the resolution of the accumulator and the image defined with dp refer to the resolution of the parameter and image space,

respectively. For example, if dp has a value of 2, the parameter space will be a factor 2 smaller than the image space. Secondly, the higher threshold for Canny edge detection defined with p_1 refers to the highest grey value in the image that will be detected. Finally, the accumulator threshold defined with p_2 indicates the minimum value inside the accumulator matrix needed to detect a circle. Hence, if p_2 is set to a low value, only a small number of points should intersect in the parameter space. This will result in a large number of circles detected by the Hough gradient method.

Table 3.1: Parameters and their definition used in the Hough gradient method [71]

Parameter	Definition
dp	Inverse ratio of the accumulator resolution to the image resolution
D_{min}	Minimum distance between the centre of particles
R_{min}	Minimum radius of a circle
R_{max}	Maximum radius of a circle
p_1	Higher threshold for Canny edge detection
p_2	Accumulator threshold

The fringe frequency follows from the FT applied to the microbubbles. In this study, a 2D Fast Fourier Transform (FFT), a fast algorithm to numerically apply the FT to signals, is used. More information regarding the principles of the FT and FFT can be found in Section A.3. Applying a 2D FFT to a fringe pattern results in a PSD of the spatial frequency. An illustration of a fringe pattern and the corresponding PSD is illustrated in Figure A.7. Due to the appearance of sine and cosine waves in the frequency domain, two equivalent frequencies with opposite signs are found by the 2D FFT. In this study, only the positive spatial frequency is used to determine the size of microbubbles.

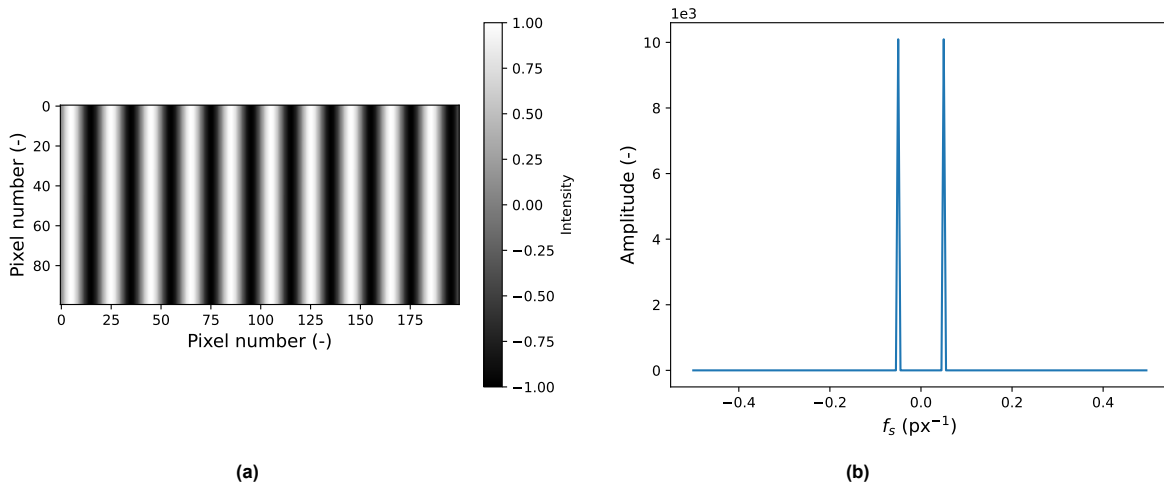


Figure 3.7: a) Fringe pattern ($f=0.05$ cycles/px) for a resolution of 200 by 100 px and b) corresponding spatial frequency retrieved from FFT analysis

3.4. Uncertainty in microbubble size

According to Méès *et al.* [31], the diameter of a microbubble can be determined with Equation 3.5. The uncertainty in parameters used in this equation results in an uncertainty in the bubble diameter. This includes the uncertainty in α , κ , f_p and D_{px} .

First of all, the uncertainty in α depends on the uncertainty in other parameters of the setup. The uncertainty in these parameters follows from a camera calibration, which is performed to determine the value of α . A detailed description of this procedure can be found in Section 5.1. Secondly, while the value of κ is a function of the bubble diameter (Figure 3.6), a single value for κ is chosen to determine the size of the microbubbles. This results in an uncertainty, which increases for smaller bubble diameters. For example, the uncertainty in the bubble diameter of a microbubble of 10 and 100 μm relies

for 98.3 and 16.5% on this parameter [17]. Next, the uncertainty in the spatial frequency of the fringe pattern increases the uncertainty in the microbubble diameter. The uncertainty in the frequency can be estimated with the Cramer-Rao Lower bound (CRLB), which describes that the minimum variance in the frequency can be estimated as [72]:

$$\sigma_f^2 = \frac{12}{(2\pi)^2 SNR N (N^2 - 1)} \cdot f_s^2 \quad \text{with} \quad SNR = 10 \log_{10} \frac{P_s}{P_n} \quad (3.9)$$

with:

- σ_f : std of f_p
- SNR : signal to noise ratio
- N : number of samples
- f_s : sampling frequency
- P_s : signal power
- P_n : noise power

Both P_s and P_n are determined from the PSD of the frequency spectrum found by the FFT. Since σ_f increases several orders of magnitude for $SNRN < 15$ dB [73], microbubbles are in this study only considered when $SNRN \geq 15$ dB.

Lastly, the uncertainty in D_{px} should be considered, which depends on the Full-Width at Half Maximum (FWHM) [67]. In general, the FWHM describes the width of a function described between the points where the function's value is half of the maximum of this function. In this study, the FWHM can be used to determine the uncertainty in the edge location of a microbubble. More specifically, the intensity gradient of a microbubble can be determined, which shows two peaks corresponding to the edges of the microbubble. Assuming that these peaks follow a Gaussian, the uncertainty in D_{px} can be written as [67]:

$$\sigma_{D_{px}} = \frac{\sqrt{FWHM_{left}^2 + FWHM_{right}^2}}{\sqrt{8}} \quad (3.10)$$

4

Principles of hydraulic turbines and model testing

In this chapter, the main principles of hydraulic turbines relevant to this study are described. First of all, an introduction to different hydraulic turbines is given in Section 4.1. Thereafter, the main principles behind the Francis turbine are described in Section 4.2, followed by a theoretical background in the operating conditions of turbines in Section 4.3. Finally, the principles behind a Hillchart model testing and cavitation in turbine models are described in Sections 4.4, 4.5 and 4.6, respectively.

4.1. Introduction to hydraulic turbines

Hydraulic turbines convert hydraulic power into mechanical power. This hydraulic power is a function of the mass flow ($\rho_w Q$) and the specific energy [74]:

$$P_h = \rho_w Q E \quad \text{with} \quad E = gH \quad (4.1)$$

where Q , E and H are the discharge of water, the specific energy and the net head of the turbine, respectively. Here, the head is defined as the height difference between the water source and the turbine minus the losses in the penstock (Figure 4.1).

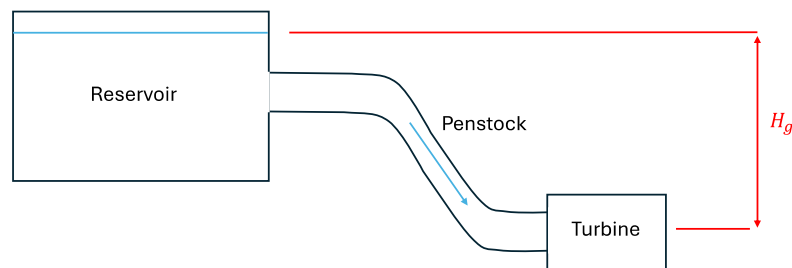


Figure 4.1: Schematic overview of a hydraulic power plant showing the reservoir, penstock and hydraulic turbine. The direction of the flow is indicated by the blue arrow. The height difference between the water level in the reservoir and the centerline of the turbine runner (here simplified to the turbine) is defined by the gross head H_g .

The conversion of hydraulic to mechanical power comes with losses, which are considered in the efficiency of the turbine as follows [74]:

$$\eta_h = \frac{P_m}{P_h} = \frac{T\omega}{\rho_w Q E} \quad (4.2)$$

where T and ω are the torque and angular velocity of the runner, respectively. Depending on the type of hydraulic turbine, this torque is obtained via an impulsive or reactive mechanism [75]. Turbines based on the first principle are identified as impulse turbines, whereas turbines based on the second principle are known as reaction turbines. The geometry of the former is characterised by a fixed nozzle that releases water from a reservoir to symmetric bucket-shaped turbine blades (Figure 4.2). The rotation of these blades relies solely on the conversion of kinetic energy into torque. In contrast, reaction turbines rely on changes in both the kinetic energy and pressure to produce a torque. This torque is caused by the rotation of the runner blades due to the radial flow of water. Thereafter, water leaves the turbine axially between the runner blades. The decreasing spiral casing diameter (Figure 4.2) and the guidance of the water flow through the vanes increases the efficiency of the turbine [75].

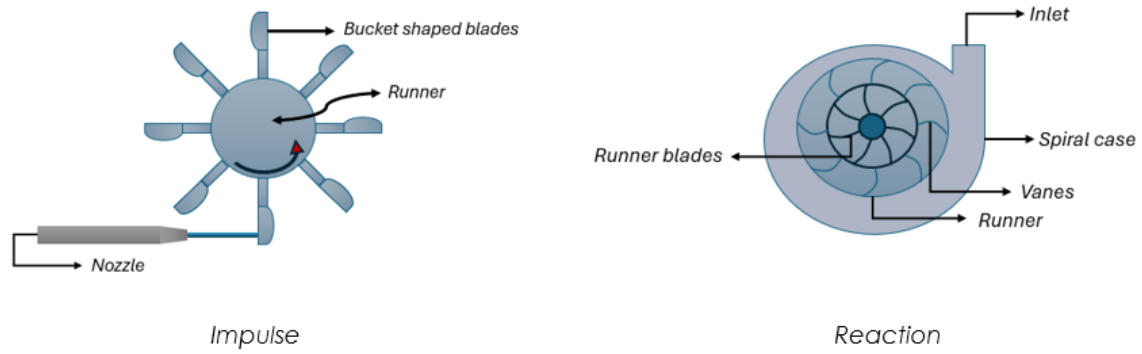


Figure 4.2: Schematic of existing hydraulic turbines and their components

Examples of turbines classified as reaction turbines are the Francis and Kaplan turbines, whereas the Pelton turbine is the most common impulse turbine. Figure 4.3 provides an overview of the existing types of hydraulic turbines and their operating range. Although there is some overlap between the operating regions of different turbines, impulse turbines typically operate at higher heads than reaction turbines. This is because the velocity of the water at the exit of the nozzle should be large enough to develop a torque, which is only possible if the head of the turbine is large enough. In contrast, reaction turbines do not have to operate at high heads, as a significant part of the hydraulic power is developed by the discharge of water through the turbine.

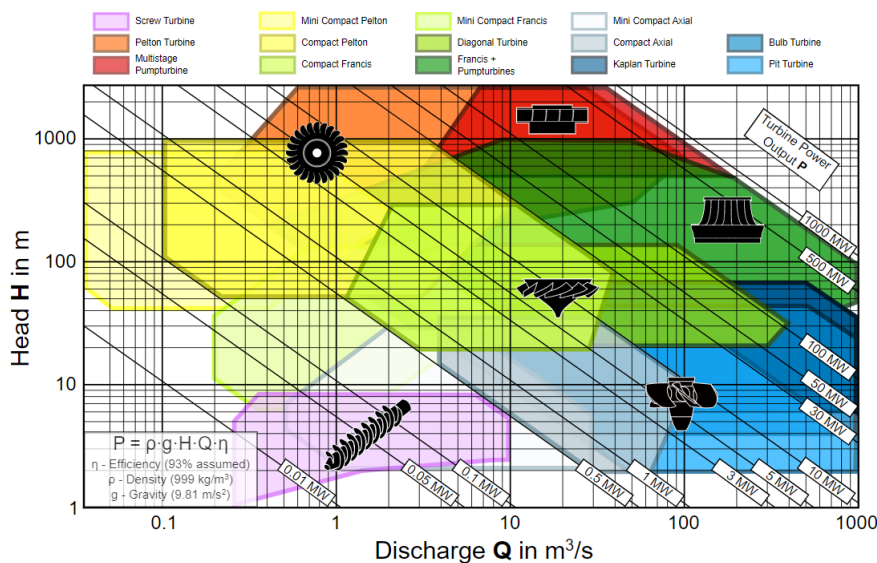


Figure 4.3: Existing hydraulic turbines and their operating range (Private communication).

4.2. Francis Turbine

In this study, cavitation is observed around the runner of a Francis turbine model. An overview of the different components of such a turbine is illustrated in Figure 4.4. Water enters the spiral case of the turbine at location *I*, indicating the high-pressure region of the turbine. This case reduces in size before it enters the stay vanes. This is to ensure that the pressure inside the spiral case remains constant [76]. After the spiral case, the flow is controlled by both stay and guide vanes. The stay vanes are fixed blades that reduce the circulation in the flow, which is caused by the radial motion of water inside the spiral casing, thereby increasing the efficiency of the turbine. In contrast to the stay vanes, the direction of the guide vanes can be controlled by changing their AOA. Changing the AOA makes it possible to change the mass flow in the turbine, thereby altering the efficiency of the turbine [75]. After the runner

blades, which are rotated by the developed torque, water leaves the runner axially via the diffuser. The outlet of the turbine is characterised with \bar{I} , indicating the low-pressure region of the turbine.

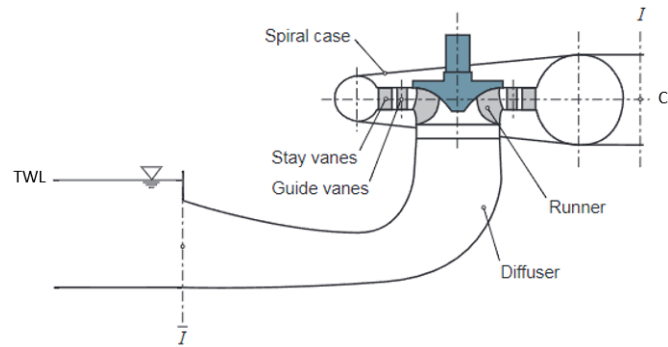


Figure 4.4: Overview of the different components inside a Francis turbine. I and \bar{I} represent the inlet spiral, the high-pressure side and the outlet of the draft tube, the low-pressure side of the turbine. Modified from Nicolet [76]

4.3. Operating conditions of hydraulic turbines

Hydraulic turbines can operate at different operating points. These points are indicated by the runner's speed, the discharge of water through the turbine and the net head. To compare the performance of turbines, a non-dimensional speed and discharge factor are introduced [74]:

$$n_{ED} = \frac{n_{pt} D_{pt}}{60 \cdot (gH_{pt})^{0.5}} \quad (4.3)$$

$$Q_{ED} = \frac{Q_{pt}}{D_{pt} \cdot (gH_{pt})^{0.5}} \quad (4.4)$$

where n_{ED} and Q_{ED} are the non-dimensional runner's speed and discharge factor, respectively. Here, the subscript pt denotes the prototype. Based on these factors, the operating profile of a hydraulic turbine changes to either a pump or turbine mode. The operating regimes of the turbine are characterised by a four quadrants diagram, illustrated with Figure 4.5. Here, all quadrants except quadrant I indicate that the turbine operates in a pump mode, also known as a pump turbine. However, in this study, the focus lies on turbines operating in quadrant I.

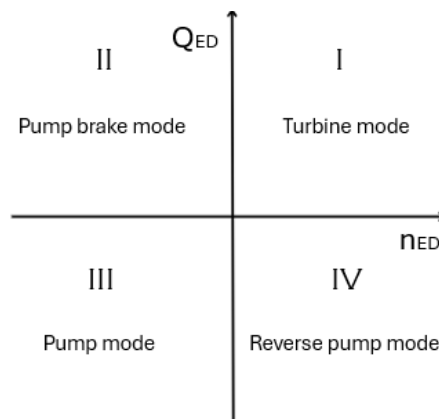


Figure 4.5: Four quadrant characteristics of turbines adjusted from International Electrotechnical Commission [74]

4.4. Hillchart

To indicate the performance of a hydraulic turbine under different conditions, propeller efficiency curves are developed during model testing. For each curve, the efficiency of the turbine is determined as a

function of the AOA of the guide vanes and thus as a function of Q_{ED} , while n_{ED} is kept constant. For the Francis RD-188 Type, a propeller efficiency curve at $n_{ED}=0.2234$ is illustrated with Figure 4.6. By measuring the efficiency of the turbine at different Q_{ED} , a diagram can be developed showing the performance of the turbine for every condition. For the turbine mode specifically, this can be illustrated with a Hillchart. An example of this is shown in Figure 4.7. Around the best efficiency point (BEP) indicated by the blue dot inside the shaded region representing the normal continuous operating range of the turbine, isocurves of efficiency are shown by the black curves. The green curves show different guide vane openings. The Hillchart in Figure 4.7 was developed before performing propeller efficiency curves on the RD-188 Type and thus only gives an indication of the performance of this model. These preliminary Hillcharts are developed for each project from data from a previous project and adjusted to predict the performance of the new model.

The operating range of a hydraulic turbine is constrained by the onset of cavitation. The edges of the operating area (Figure 4.7) mark the transition from operating the turbine in a cavitating-free zone inside the shaded area to a cavitating zone outside this region. The blue dots at the edge of the operating region indicate critical points of the turbine. At these critical points, cavitation around the runner of the turbine is observed during model tests.

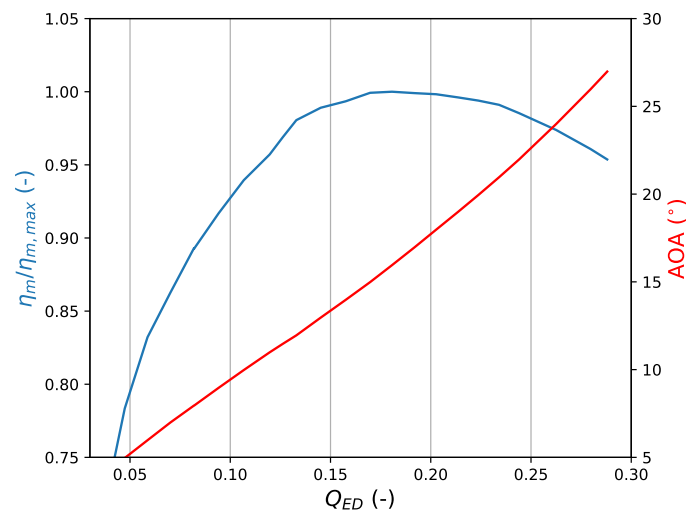
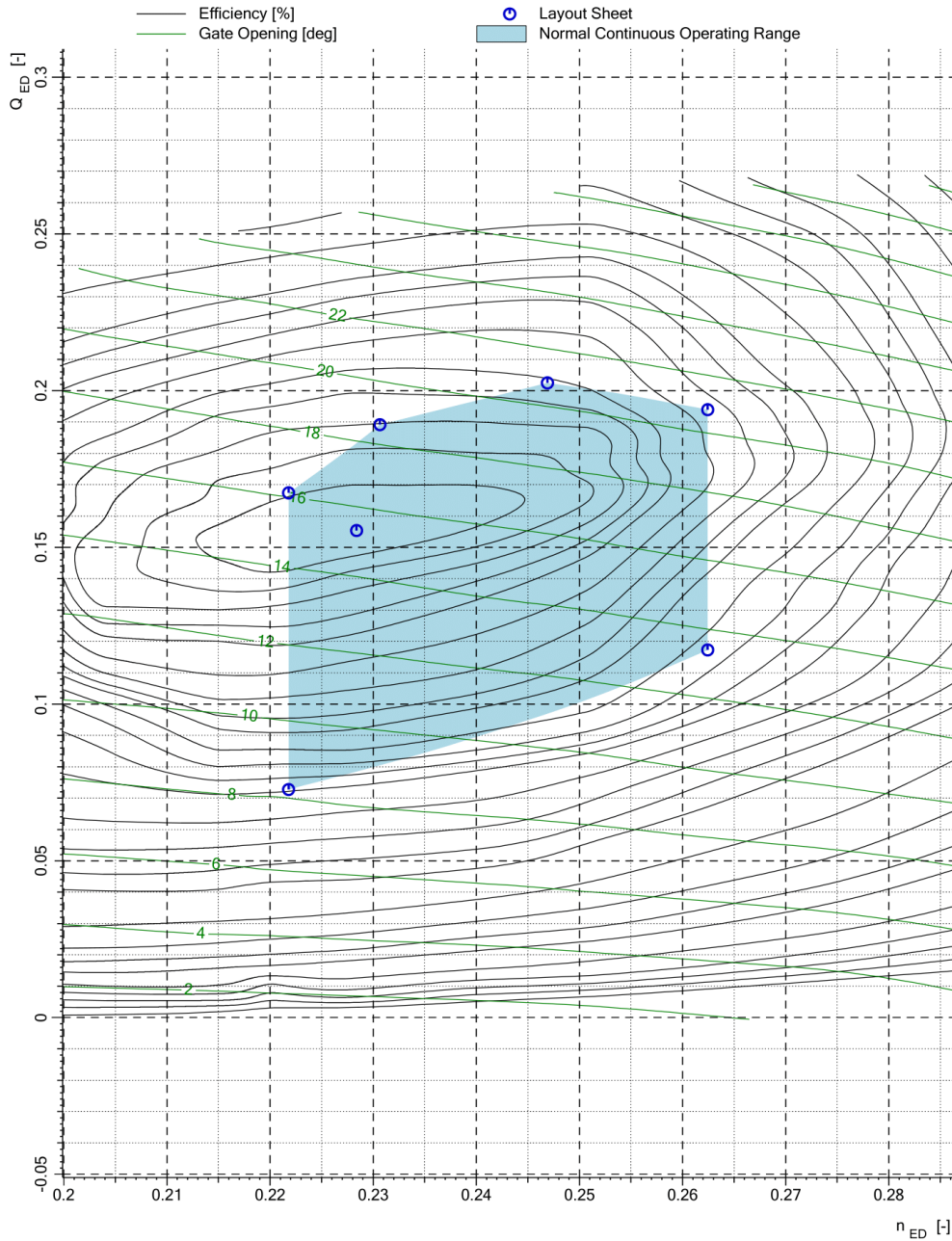


Figure 4.6: Propeller efficiency curve at $n_{ED} = 0.2234$. The blue and red curves represent the normalised efficiency and the AOA, respectively. For each propeller curve diagram, the efficiency of the turbine can be determined as a function of the AOA of the guide vanes and thus the Q_{ED} .

Type188_2022_T3

Adapted Model Hillchart

Target 3



v1s fr01 - E	D ₂ = 0.31030 [m]	ρ = 999.1 [kg/m ³]	Prep.	Date
	D _{min} = 0.31030 [m]	g = 9.80840 [m/s ²]	Läufer	05-July-2024
	Site El. = 0.00 [m]	Re _{D2} = 7.000E6 [-]	Checked	Dwg.
	n = 1393.49 [rpm]			

Figure 4.7: Predicted Hillchart of the Francis RD-188 Type. The blue dots around the normal continuous operating range show the operating points of the Francis RD 188-Type where cavitation is predicted. The best efficiency point (BEP) of the turbine is indicated by the dot inside the turbine's normal continuous operating range. The values for the BEP and the isocurves for efficiency are not shown for confidential reasons.

4.5. Model testing

During model testing, different measurements are performed to study the performance of hydraulic turbines. One of these measurements focuses on the performance of the turbine at the critical points on the Hillchart. With these measurements, sigma break curves are developed showing the relation between η_m and σ . With these curves an indication of σ_i and $\sigma_{\eta,1}$ can be made. The value of η_m is determined from the torque developed by the model, while the cavitation number of the turbine depends on the following terms [74]:

$$\sigma_{tm} = \frac{\frac{p_a - p_v}{\rho g} - H_s + H_{L,dt}}{H_m} \quad (4.5)$$

where p_a , p_v and $H_{L,dt}$ denote the ambient pressure, vapour pressure and the draft tube losses inside the test rig. For each sigma break curve, only H_s is varied. For each point on the sigma break curve, the time-averaged value of these parameters is used to determine σ_{tm} . To determine the vapour pressure at every timestep, the water temperature inside the test rig is measured. For $0^\circ\text{C} \leq T_w \leq 40^\circ\text{C}$, the vapour pressure can be estimated as [74]:

$$p_v = 10^{(2.7862 + 0.031 \cdot 2T_w - 0.000104T_w^2)} \quad (4.6)$$

It should be noted that the kinematic viscosity also depends on the water temperature, meaning that Re also slightly varies during the measurements.

Because the head of the turbine cannot be scaled down to the model size based on the height difference between the water reservoir and the turbine, the head of the model is obtained differently. For the model, the specific energy is determined by Bernoulli's law, while the height difference is obtained from the turbine's inlet and outlet. An example of this height difference is illustrated in Figure 4.4 by I and \bar{I} . This results in the following relation [74]:

$$H_m = \frac{\Delta p}{\bar{\rho}g} + \frac{\Delta V^2}{2g} + \Delta z \quad \text{with} \quad \bar{\rho} = \frac{\rho_1 + \rho_2}{2} \quad (4.7)$$

where V and Δz are the velocity of the flow and the height difference between the in and outlet of the turbine, respectively. The subscript m denotes the model. For a compressible flow, losses inside the turbine have to be taken into account as well. The head of the model is generally referred to as the *Net head* p_{12} (Figure 4.8a).

Another important term in Equation 4.5, is the suction head of the model H_s . This parameter is controlled by a tank downstream of the turbine model, where the amount of vacuum and pressurized air can be controlled. Controlling the water level in this tank, changes H_s as follows:

$$H_s = CL - TWL \quad (4.8)$$

Here, CL and TWL denote the centerline of the turbine and the tailwater level (water level of the tank) (Figure 4.8b). The TWL of the tank is controlled by the pressurised air and vacuum system, which are connected to this tank. By controlling the pressurised air and the vacuum applied to this tank, the pressure can be controlled, thereby controlling the TWL . Hence, if the TWL is solely controlled by the pressurized air, the pressure inside the tank will increase, and thus, the TWL will increase. As the water level inside the tank can be above the centerline of the runner as a result of the pressurised air applied to the system, a negative value for H_s is applied to the system. Due to the sign convention of the hydraulic industry, an increase in the pressure inside the facility is found at negative values of H_s . In contrast, applying a vacuum to the tank will result in a decrease in the water level and, thus, a decrease in the pressure, as the value of H_s becomes positive.

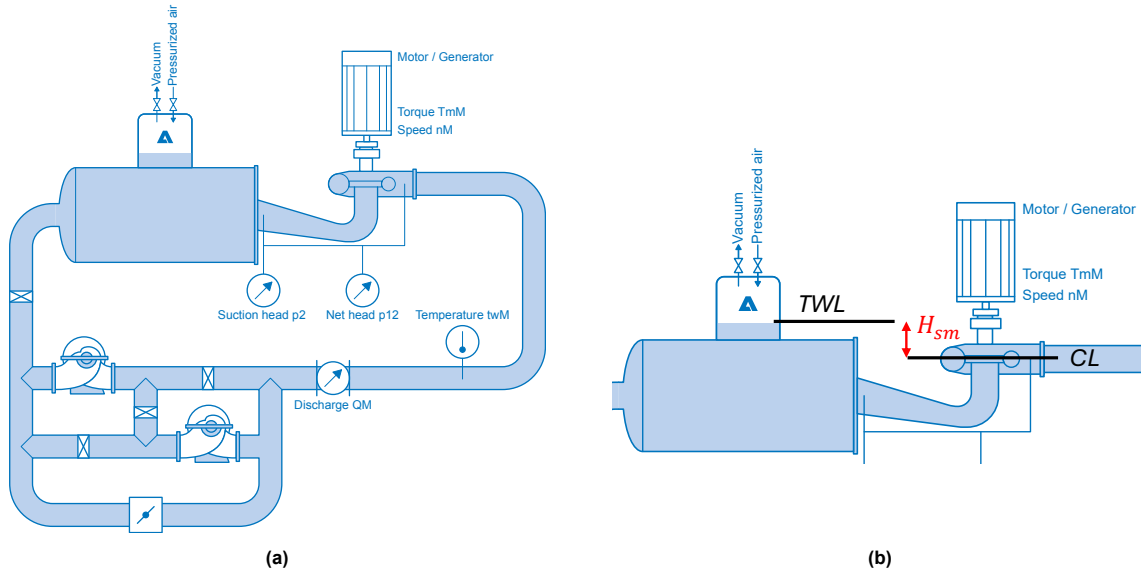


Figure 4.8: a) Schematic of a radial test rig used to conduct the measurements in this study, b) Close-up of the turbine model and tank downstream of the turbine. The suction head H_s is controlled by the water level TWL , which is controlled by vacuum and pressurised air. Both of these systems can be controlled by valves above the tank.

Since the vacuum power applied to the tank is limited by the design of the vacuum pump connected to this tank, the maximum value that can be achieved for H_s is limited. Therefore, controlling the value of the TWL is limited, thereby limiting the pressure range at which model tests can be performed to approximately 1.5 bars. Conducting measurements at a larger pressure range is possible by changing the head of the model. To maintain the working point of the turbine and thus the performance of the turbine, the values for n_{ED} and Q_{ED} should remain constant. However, this results in a change in the runner's speed accordingly:

$$n_m = \frac{60n_{ED}}{D_m} \cdot \sqrt{gH_m} \quad (4.9)$$

Since the runner speed of the turbine correlates to the head of the turbine, the runner speed also influences the cavitation number of the turbine. Substitution of Equation 4.9 into Equation 4.5 result in the following relation between n_m and σ_{tm} :

$$\sigma_{tm} = \left(\frac{p_a - p_v}{\rho} - g \cdot (H_s - H_{L,dt}) \right) \cdot \left(\frac{60n_{ED}}{n_m D_m} \right)^2 \quad (4.10)$$

From Equation 4.10 it follows that the cavitation number of the turbine is inversely proportional to n_m^2 , thereby indicating that measurements performed under identical test conditions at higher runner speeds will result in a decrease in the cavitation number of the turbine. It should be noted that the runner speed also affects Re of the turbine.

4.6. Cavitation on model scale

During model testing, cavitation around the runner of a turbine is observed visually. Depending on the working point of the turbine and thus the position in the Hillchart, different forms of cavitation are observed around the runner of a Francis turbine (Figure 4.9). In this study, two working points of the turbine are considered: critical and non-critical working points. These points are located at the edge of the continuous operating range and inside the operating range, respectively. This range is illustrated by the area enclosed by the black curves in Figure 4.9. It should be noted that the cavitation regimes illustrated in Figure 4.9 can differ depending on the type of Francis runner.

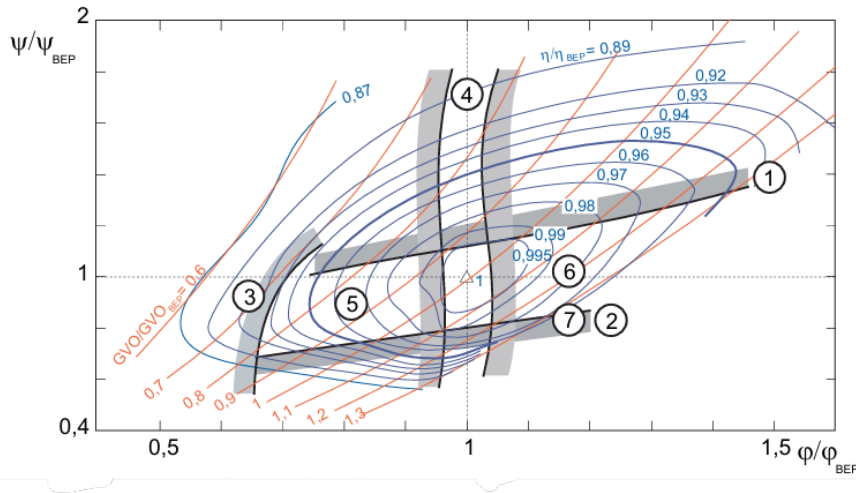


Figure 4.9: Different regimes in a standard Hillchart of a Francis turbine indicating the different forms of cavitation: 1) inlet edge suction side, 2) inlet edge pressure side, 3) inter blades vortices, 4) cavitating vortex free zone, 5) part load cavitating vortex, 6) full load cavitating vortex, 7) bubble cavitation at the outlet edge suction side. Here, Ψ , ϕ and GVO denote the n_{ED} , Q_{ED} and the guide vane opening, respectively. These parameters are normalised to the turbine's BEP.

In general, cavitation in Francis turbines is observed around the outlet of the runner, the runner blades and the gap between the runner and the stationary tube of the turbine (Figure 4.10). In the continuous operating regime of the turbine, the turbine is in a rope-free zone, i.e., no cavitating vortex appears at the outlet of the runner (Figure 4.11a). In contrast, outside this zone, a cavitating vortex appears at the outlet of the runner (Figure 4.11b). This form of cavitation develops from vortices caused by circulation in the flow and contains vapour bubbles in the core of the vortex [10]. Depending on the pressure of the surrounding liquid around the runner, the cavitating core of the vortex changes in size [10]:

$$p_{\infty} - p_v = \frac{\rho\Gamma}{8\pi^2 a_c^2} \quad (4.11)$$

where Γ and a_c denote the circulation and the cavitating core of a vortex, respectively. During model testing, the cavitation number is reduced, i.e., the pressure around the model is reduced, thereby increasing the cavitating core of the vortex. Although this form of cavitation is generally found at higher cavitation numbers than other forms observed around the runner, it is not considered the most critical form of cavitation in the hydraulic industry. This is because it does not cause erosion on the runner blades. However, the pressure fluctuations caused by a cavitation vortex can generate noise and vibrations on the runner [77].

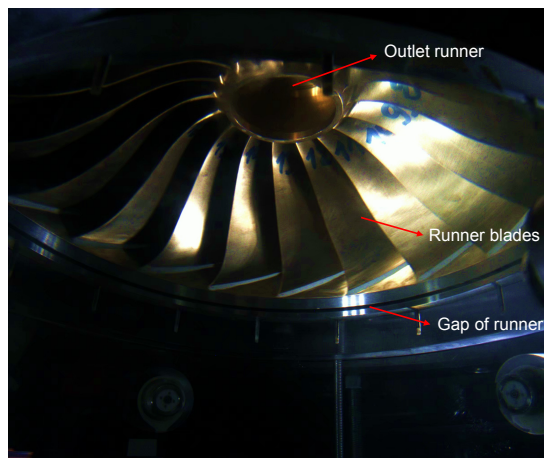


Figure 4.10: Runner of a Francis RD-188 Type model showing the different components where different forms of cavitation can be observed.

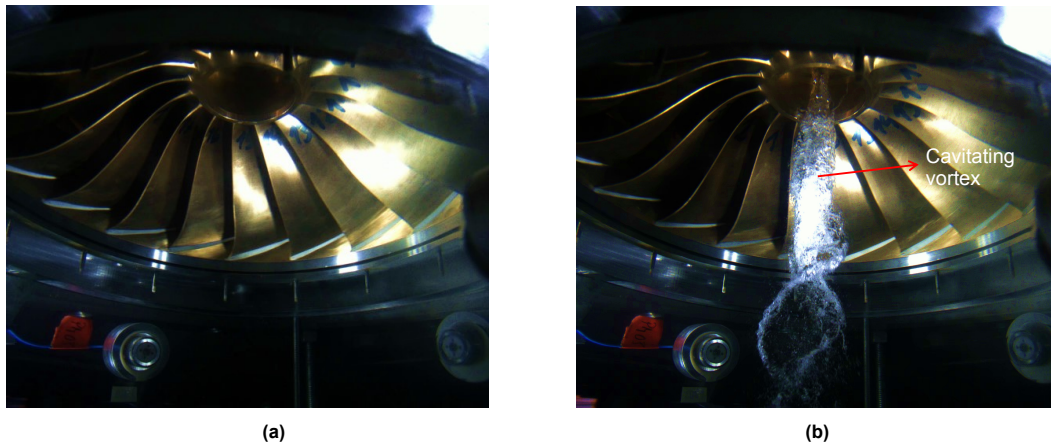


Figure 4.11: Francis RD-188 Type runner a) free of a cavitating vortex, b) with a cavitating vortex appearing at the outlet of the runner

The second form of cavitation observed in Francis turbines, called gap cavitation, occurs both at the critical and non-critical points considered in this study. This form of cavitation is heavily influenced by labyrinth seals located between the runner and the stationary casing of the turbine. These seals are illustrated with the yellow areas in Figure 4.12. While these seals reduce the leakage flow between the runner and the casing of the turbine, a low-pressure region is observed at the outlet of the labyrinth. Due to the interaction between the low-pressure region found at the downside of the runner blades and the low-pressure region at the outlet of the labyrinth, large vapour volume fractions are observed at the outlet of the labyrinth compared to the surrounding geometry. As a result, vapour bubbles are observed at the gap of the runner (Figure 4.13). Since the flow is not uniform around the labyrinth seals, the vapour volume fraction changes significantly over time, resulting in a dynamic evolution of the vapour bubbles observed at the gap of the runner [78].

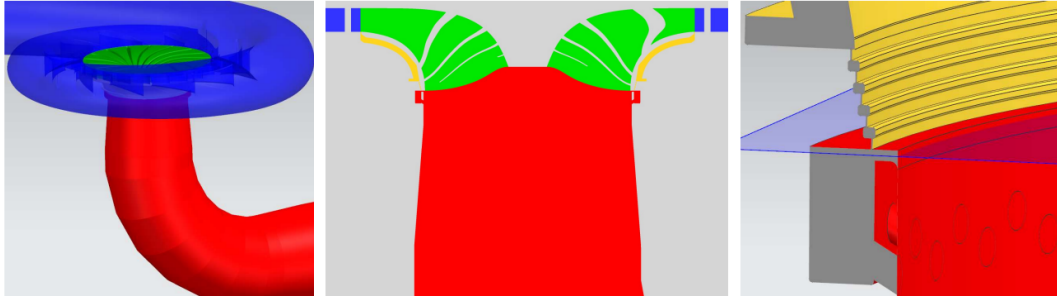


Figure 4.12: Schematic overview of a total Francis model (left), close-up of a Francis model from the front (middle), and close-up of the outer edge of the Francis turbine (right). The different components of the Francis turbine are as follows: spiral casing (blue), runner blades (green), labyrinth (yellow), and the draft tube (red). The labyrinth exit is located in the blue plane (right) [78].

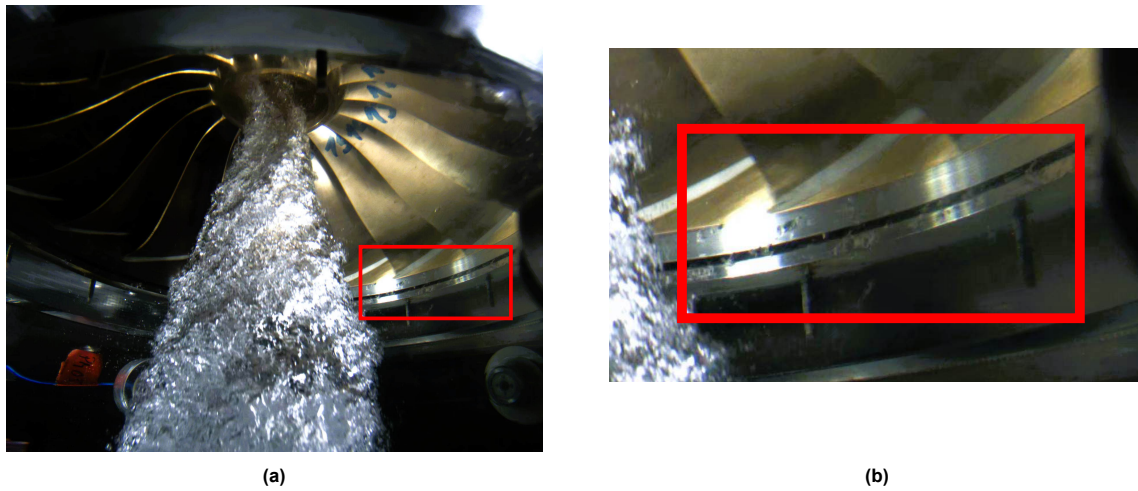


Figure 4.13: a) Francis RD-188 Type model, showing a cavitating vortex in the outlet of the runner and vapour bubbles at the gap of the runner, marked with the red box. b) Close-up of a part of the gap showing the first vapour bubbles.

Depending on the working point of the turbine, different forms of surface cavitation can be observed around the runner blades. However, in this study, surface cavitation is only observed at low values of σ , where a developed cavitating vortex and gap cavitation make it complex to study surface cavitation with the cavitation videos. Hence, this study only focuses on the cavitating vortex and gap cavitation.

5

Methodology

In this chapter the methodology of this study is described. This starts by performing a camera calibration, which is described in Section 5.1. Thereafter, an overview of the test plan, setup and methodology of IPI measurements is given in Section 5.2

5.1. Camera calibration

According to Méès *et al.* [31], the diameter of microbubbles is inversely proportional to the collection angle of the camera (Equation 3.5). Because this angle depends on the settings of the camera lens, a camera calibration should be performed to determine the value of α . The methodology for this calibration was proposed by Stigter *et al.* [67].

5.1.1. General arrangement

Figure 5.1a shows the general arrangement of the calibration setup. On the right, a Photron Nova S6 high-speed camera with a ZEISS Milvus 2/100M lens is fixed to an aluminium profile. For this calibration, the aperture and the focal distance of the lens are set to $f/2.0$ and 440 mm, respectively. In front of the camera, a 32 mm planar polymethyl methacrylate (PMMA) window is positioned. This window is later located at the measurement position and functions as the camera window. More information regarding this setup can be found in Section 5.2.1. Behind the window, a Thorlabs R2L2S3P4 fixed grid distortion target plate is located. An illustration of this target plate is shown in Figure 5.1b. The target plate contains dots with a size of 0.500 mm and a spacing of 1.000 mm. In contrast to the camera, the target plate can be shifted over the aluminium profile as it is mounted to a MicroStager, which can freely move in the direction of the profile. In addition, the top plate of the MicroStager, where the target plate is located, can be moved further with a precision of $1.0 \cdot 10^{-3}$ mm.

With this setup, it is possible to change the position of the target plate with respect to the camera. Thus, images of the target plate at different locations can be taken, from which α can later be calibrated. More information on these steps is provided in Sections 5.1.2-5.1.5. The calibration starts by shifting the target plate to the focal plane of the camera. Once this position is found, the target plate can be shifted away from this position in both directions: towards the camera and further to the left end of the aluminium profile. During this calibration, images of the target plate are taken at an interval of ± 10.0 mm, with a step size of 0.50 mm. For every image, the distance between the camera chip and the frontal surface of the target plate is measured for further processing.

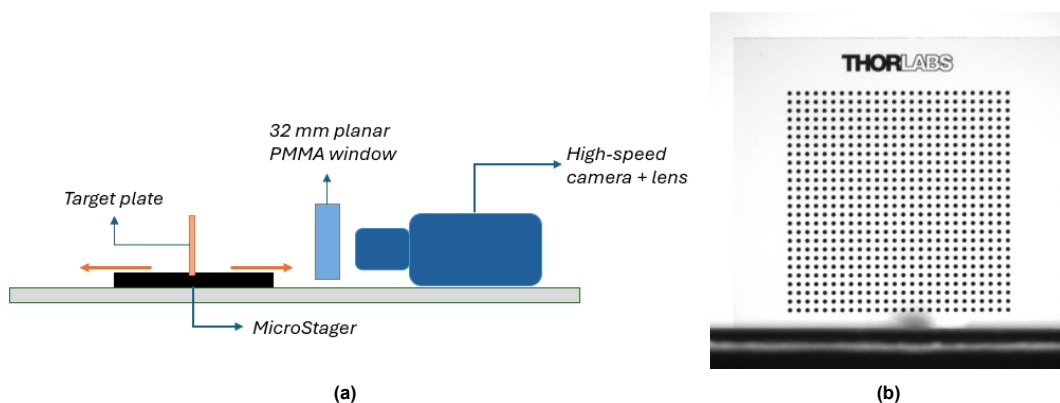


Figure 5.1: Illustration of a) the general arrangement of the camera calibration, and b) an R2L2S3P4 Thorlabs fixed grid distortion target plate.

5.1.2. Circle detection

From the images of the target plate, it is possible to determine the collection angle of the camera. This starts by determining the image size of the dots on the target plate using a circle detection method. The first step of this method involves the subtraction of a mean filter from the images. Thereafter, an intensity threshold is applied to these images, making it possible to only select the dots on the target

plate for further processing. Because the dots have a low intensity relative to the remainder of the images, the following statement should hold to detect them:

$$I \leq I_{Th} \quad (5.1)$$

where I_{Th} is the intensity of the applied threshold. An example of detected dots on the target plate by applying an intensity threshold is shown in Figure 5.2. From the regions that satisfy this condition, the dots on the target plate have to be detected. This is achieved by setting another constraint:

$$A_{min} \leq A \leq A_{max} \quad (5.2)$$

where A_{min} and A_{max} are the minimum and maximum areas of the region that are accepted, respectively. In this study, A_{min} and A_{max} are set to 30 and 1000 px, respectively.

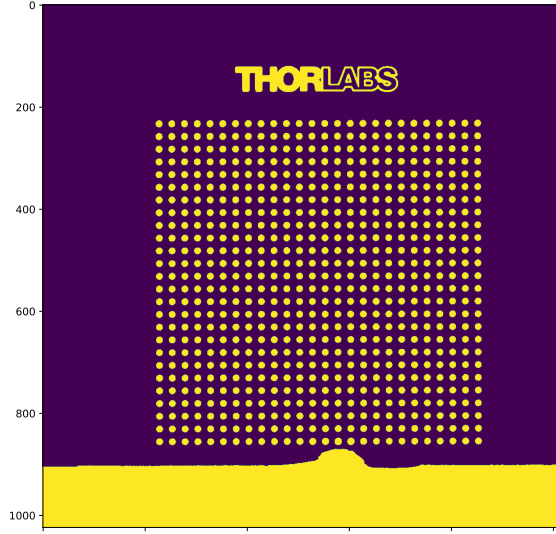


Figure 5.2: Application of an intensity threshold to an image (Figure 5.1b) of the R2L2S3P4 Thorlabs grid distortion plate. The regions with an intensity above the intensity threshold are marked with purple, while those with an intensity below the threshold are marked with yellow. Circles are detected within the yellow regions only.

After identifying the dots on the target plate, an additional method based on the principles of Shadowgraphy is applied to detect the size of these circles for more precision. This is because the size of the detected dots is influenced by edge blur and contrast, which is not considered in the previous method. To determine the size of the dots, it is important to determine the contrast between the dots and the background, whereas the amount of edge blur is used to determine the out-of-focus distance of the target plate for every image. The contrast in the images is determined by considering the minimum and maximum intensities in the images:

$$C = \frac{1 - I_{min}/I_{max}}{1 + I_{min}/I_{max}} \quad (5.3)$$

where I_{min} and I_{max} are the minimum and maximum intensity within an image, respectively.

It is also possible to describe the contrast in an image with the contrast coefficient τ and normalised radius \tilde{a} :

$$C = \frac{(1 - \tau) \cdot (1 - e^{-\tilde{a}^2})}{2 - (1 - \tau) \cdot (1 - e^{-\tilde{a}^2})} \quad \text{with} \quad \tau = \min\left(\frac{I_{min}}{I_{max}}\right) \quad (5.4)$$

Here, every microbubble is considered in the calculation for τ , but only the minimum value of the dataset is considered. The value of τ ranges between zero and one, depending on the type of particle. For perfectly opaque particles (zero light transmission), τ goes to zero.

In most of the images, it is not sufficient to solely determine C . This is because a part of the contrast can get lost in the process, due to the setup of the used optics. However, this can be accounted for by considering the normalised contrast C_0 [61]:

$$C_0 = \frac{C}{(1 - \tau) \cdot (1 + C) - C} \quad (5.5)$$

In the focal plane of the camera, it is possible to determine the size of dots directly from the contrast. However, moving the target plate out-of-focus introduces edge blur, which affects C_0 . To account for this, a polynomial p_l is introduced. To find the size of the dots, only a multiplication with the size of a px, L_{px} , should be added [67]:

$$D = 2r_l p_l(C_0) L_{px} \quad (5.6)$$

Here, r_l is defined as the radius of the dots in px. The index l represents the intensity level that is considered. This intensity level lies between I_{min} and I_{max} and is defined as [61]:

$$I_l = I_{min} + l \cdot (I_{max} - I_{min}) \quad (5.7)$$

The radii of these dots are best defined at $l=0.61$, whereas the edge width Δr should be between the levels 0.25 and 0.77 [61]. At the given level, the radii of the dots are found by considering all px with an intensity lower than I_l . For every dot, this results in an area, which can be divided over π , resulting in r_l^2 .

5.1.3. Focal plane

During the camera calibration, the target plate is set at different positions from the camera, both in and outside the focal plane of the camera. For each position of the target plate, the distance to the lens of the camera can be defined by the parameters z_1 and z_0 , which are defined as the distance between the lens and focal plane of the camera and the distance between this plane and the position of the target plate (Figure 5.3). Hence, $z_0=0$ mm corresponds to a target plate positioned in the focal plane of the camera.

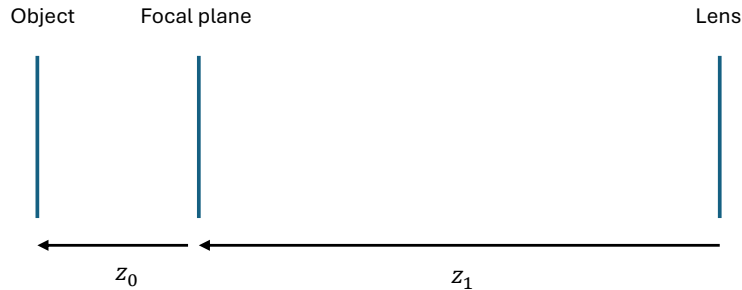


Figure 5.3: A schematic overview of the position of an object with respect to the lens and focal plane of the camera. Here, z_1 and z_0 denote the distance between the lens and focal plane and the distance between the focal plane and object, respectively. For an object positioned in the focal plane, $z_0=0$ mm.

Depending on the value of z_0 , the edge blur of the dots changes. As the effects of edge blur are minimal when the target plate is positioned in the focal plane of the camera, it is possible to find the location of the focal plane ($z_0=0$ mm). The relation between the edge blur and this z_0 can be described with the Point Spread Function (PSF), which describes the effects of optics on blurring in the image [79]. In case of incoherent and non-monochromatic light, as is used during the camera calibration, the PSF can be described by a 2D Gaussian function [79]. With a 2D Gaussian function, the edge blur can be directly related to z_0 by considering the width of the Gaussian χ_{PSF} [61]:

$$\chi_{PSF} = \frac{\Delta r}{p_r(C_0)} \quad \text{with} \quad \Delta r = r_{0.77} - r_{0.25} \quad (5.8)$$

Here, Δr is defined as the edge width based on the difference in the radius for the intensity levels $l=0.25$ and $l=0.77$. To correct for the sharpness and transparency of the dots on the target plate, a third-order polynomial p_r is used to fit the data.

For every dot on the target plate, χ_{PSF} can be calculated using Equation 5.8. For each image, this results in a list of values for χ_{PSF} . From this list, the median and standard deviation (std) are calculated and plotted as a function of the out-of-focus distance z_0 , as illustrated in Figure 5.4. At the lowest value of χ_{PSF} , the edge blur is minimal, which corresponds to the focal plane of the camera ($z_0=0$ mm). From this, it follows that the focal point is found at a distance of 446 mm away from the chip of the camera. It is worth noting that the relation between the edge blur and z_0 works well when objects are positioned close to the focal plane of the camera but becomes less accurate if z_0 increases. This can, for example, be seen at $z_0 \geq 4$ mm, where multiple distortions in the graph appear (Figure 5.4).

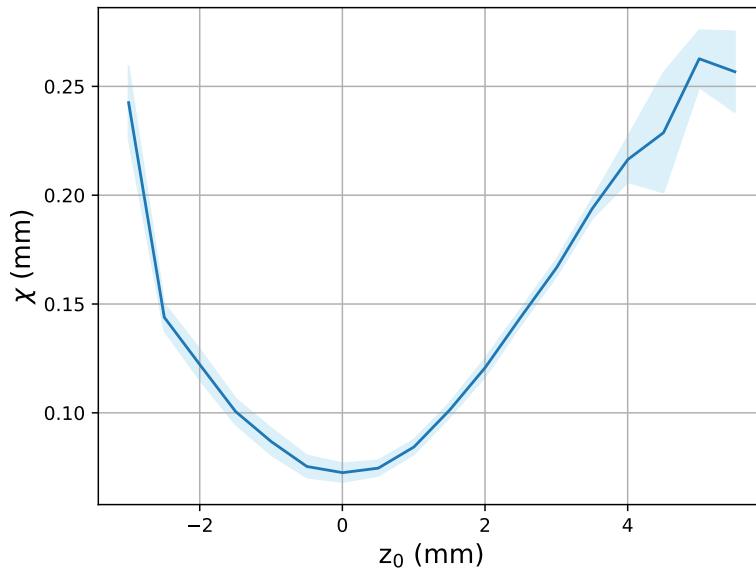


Figure 5.4: Relation between the out of focus distance z_0 and the width of the 2D Gaussian χ . At the minimum of this function, the edges of the dots are the most sharp, which can be found when the target plate is positioned in the focal plane of the camera.

5.1.4. Magnification

The final step of the calibration of α relates to the magnification of the images. From this step, it is possible to determine z_1 (Figure 5.3), necessary to determine α .

First of all, the magnification of the camera is determined for each image. This starts by calculating the distance between the dots on the target plate on the images. For every dot, the horizontal and vertical distance to neighbouring dots is calculated. For every image, the mean and std from these distances are considered. Dividing the actual dot distance of the target plate (1.00 mm) by the number of pixels represented by the mean and std, results in a pixel size. To obtain the magnification of the camera, this size should be divided by the pixel size of the camera (20 μm):

$$M = \frac{N_{px} \cdot L_{px}}{s} \quad (5.9)$$

Here, N_{px} and s represent the calculated distance between the dots in px and the actual distance between the dots specified by the manufacturer in μm . It is important to mention that it is not possible to determine the magnification directly from the dot size. This is because the dot size is influenced by the edge blur, resulting in larger dots when the target plate is positioned out of the focal plane.

The magnification that is found for the different images is illustrated in Figure 5.5. The magnification

is only shown for z_0 close to the focal point for visibility reasons. This is because large jumps in the magnification are found outside the region shown in Figure 5.5, which are caused by a decrease in contrast when the target plate is positioned further away from the focal point.

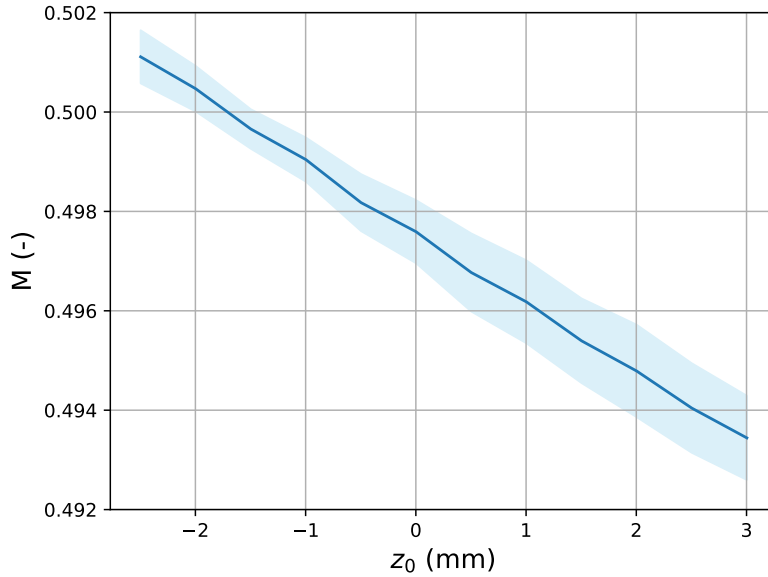


Figure 5.5: Relation between the magnification of the camera and z_0 . The curve and shaded areas represent the mean and std of the magnification. For $z_0 = 0$ mm, the target plate is positioned in the focal plane of the camera.

The magnification as shown in Figure 5.5 can be described as a function of z_0 [67]:

$$M(z_0) = M_0 \frac{z_1 n}{z_1 n + z_0} \quad (5.10)$$

where M_0 and n are the magnification at $z_0 = 0$ mm and the refractive index of the medium, respectively. Since the camera calibration is performed in air, a refractive index of 1.0 is used here. During the IPI measurements, the microbubbles are detected in a different medium: water. To account for this, the value of z_1 found in air should be multiplied by the refractive index of water.

To determine z_1 , the derivative of Equation 5.10 to z_0 can be taken:

$$\left. \frac{dM}{dz_0} \right|_{z_0} = -M_0 \cdot \left(\frac{z_1 n}{(z_1 n + z_0)^2} \right) \quad (5.11)$$

For $2.5 \text{ mm} \leq z_0 \leq 4 \text{ mm}$, a second-order polynomial is fitted through the data points with the *curve fit* function from the *Scipy* library in Python. From this fit, the pixel size and slope at z_0 are found, from which M_0 and z_1 can be calculated. The values of these parameters are 0.498 and 351.17 mm, where M_0 nearly matches the magnification of the ZEISS Milvus 2/100M of 0.50. The std of both parameters is determined by taking the square root of the diagonals of the covariance matrix corresponding to the curve fit. This results in a std of $M_{0,std} = 2.64 \cdot 10^{-4}$ and $z_{1,std} = 26.66$ mm. The std in z_1 is relatively high, which is driven by two factors. The main factor is that there has been a small rotation in the position of the target plate, resulting in larger dots detected on one side of the plate. Secondly, the curve fit is made from a small set of data points, resulting in a larger variance in the different constants of the second-order polynomial and thus a larger std of z_1 .

5.1.5. Collection angle and disk diameter

For a given z_1 , it is possible to determine the collection angle of the camera. Additionally, it is possible to relate the image disks of the dots (D_i) to z_1 . This results in the following equations for D_i and α :

$$D_i(z_0) = \left| M_0 D_a \frac{z_0}{z_1 n + z_0} \right| \quad \text{with} \quad D_a = \frac{f}{N} \quad (5.12)$$

$$\alpha(z_0) = 2 \arctan \left(\frac{D_a/2}{z_1 n + z_0} \right) \quad (5.13)$$

Here, N is set to 2.0, which corresponds to the f-number of the camera. Combined with a focal length of 100 mm, the aperture of the lens is set to 50 mm.

For the camera calibration, it is only relevant to consider α as the size of the dots on the images was already calculated to obtain z_1 . At $z_0 = 0$ mm, α is set to 8.10° . During the IPI measurements, the microbubbles will not be located at solely one position z_0 from the focal point (Figure 5.6). This means that the image disk size and the collection angle of the microbubbles will vary. This means that for every microbubble, the distance z_0 should be determined based on their disk size, from which the collection angle can be determined for every microbubble.

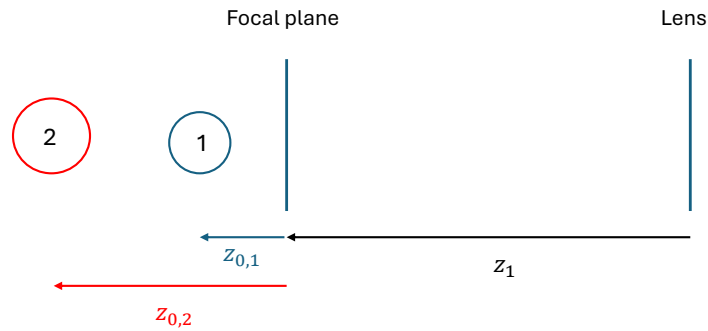


Figure 5.6: Schematic overview of the position of microbubbles with respect to the focal plane. For increasing z_0 , the image size of a microbubble increases.

5.2. IPI measurements

The IPI measurements are performed upstream of the model in the basement of a test rig of Andritz Hydro. More information on the specific location of these measurements is described in Section 5.2.1. The setup positioned at this location is described in Section 5.2.2. Due to unforeseen issues related to the output power of the laser, some changes were made to the setup. These changes are mentioned in Section 5.2.3, followed by the measurement procedure in Section 5.2.4.

5.2.1. Test location

The setup for the IPI measurements is positioned in the basement in front of a pipe segment of one of the test rigs. Because the test rig has no windows at this position, it is not possible for a laser beam to enter the facility and make recordings of the microbubbles with the high-speed camera. Therefore, a part of the pipe has been replaced by a pipe segment containing three PMMA windows. This segment including the windows is illustrated in Figure 5.7. At the bottom and top of this pipe, two windows with a diameter of 50 mm are located, which are used for the inlet and outlet of the laser beam. The third window is positioned at an angle of 90° from both of these windows and is used as an opening for the high-speed camera. The diameter of this window is 150 mm.

All three windows are planar instead of curved. This is because the windows act as lenses that deform the light. For the camera, this means that the images will deform if a curved window is used. Considering the laser, it is desired to not alter the shape of the laser beam as this will affect the measurement volume in which the microbubbles are located.

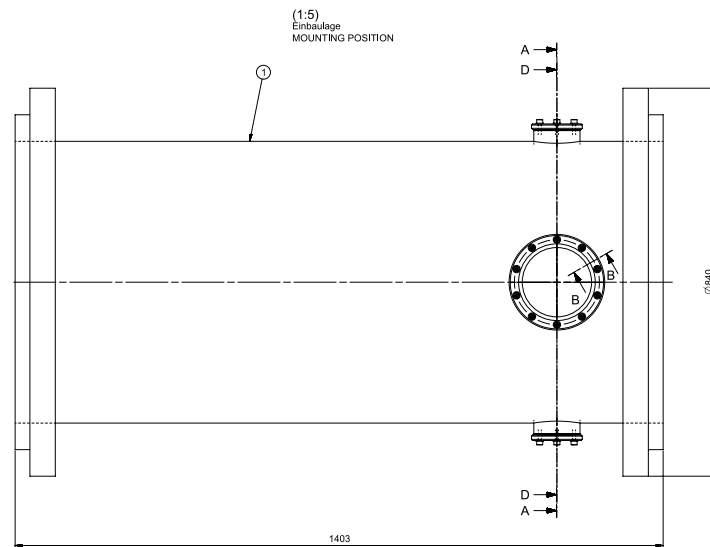


Figure 5.7: Schematic of the pipe segment used for the IPI measurements. The laser beam enters the pipe segment via the bottom window and leaves via the top window. The front window functions as an opening for the high-speed camera. The laser windows have a diameter of 50 mm, while the camera window has a diameter of 150 mm.

5.2.2. General arrangement

In front of the pipe segment shown in Figure 5.7, the setup for the IPI measurements is positioned. This is illustrated in Figure 5.8a. Initially, a diode-pumped solid-state (DPSS) 532nm continuous wave (cw) laser with a maximum output power of 10W was installed. Above this laser, a Photron Nova S6 high-speed camera with a Zeiss Milvus 2/100 M lens is mounted to the framework. The same settings for the lens are used as for the camera calibration (aperture= $f/2.0$, focal length=440 mm), such that the collection angle only changes due to a change in the medium. The camera and lens are first positioned so that microbubbles observed by the camera are in focus. After that, the camera and lens are shifted away from the pipe segment, thereby observing microbubbles out of focus. For more precision, the camera and lens can be shifted using the MicroStage, which is mounted to the camera.

The laser beam leaving the laser is altered by sheet optics positioned between the laser and the inlet window for the laser. An overview of these optics is illustrated in Figure 5.8b. Since the laser beam is mainly parallel polarised, while a perpendicular polarisation is desired, the polarisation of the laser beam is converted using a Zero-Order Half Wave Plate (ZOHWP). After that, the remainder of the parallel polarised light is reflected into a beam trap, while the perpendicular polarised light is transmitted to the coated mirror. Due to the rotation of this mirror, the direction of the laser beam is shifted with 90° , thereby allowing the laser beam to enter the inlet window.

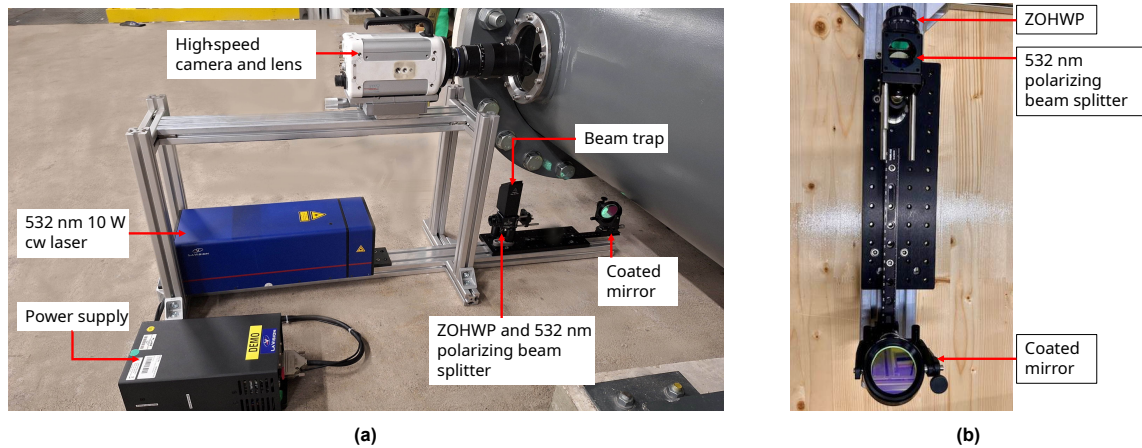


Figure 5.8: Overview of the a) total intended IPI setup and b) small optical components mounted on a breadboard.

5.2.3. Adapted arrangement

Due to unforeseen issues with the LaVision DPSS 532 nm cw 10 W laser, a different laser has been used during the measurements of this study. This replacement is an air-water-cooled 532 nm cw 18 W laser from Coherent. Figure 5.9 shows the position of the laser and its power supply and chiller in the setup. The laser is cooled via the cooling plate, connected to a chiller via the blue tubes. On top of the laser outlet window, a beam trap is positioned to collect the laser beam. During this study, the output power of the laser was set to 13 W, and the aperture and focal distance of the camera were set to $f/2.0$ and 440 mm, respectively.

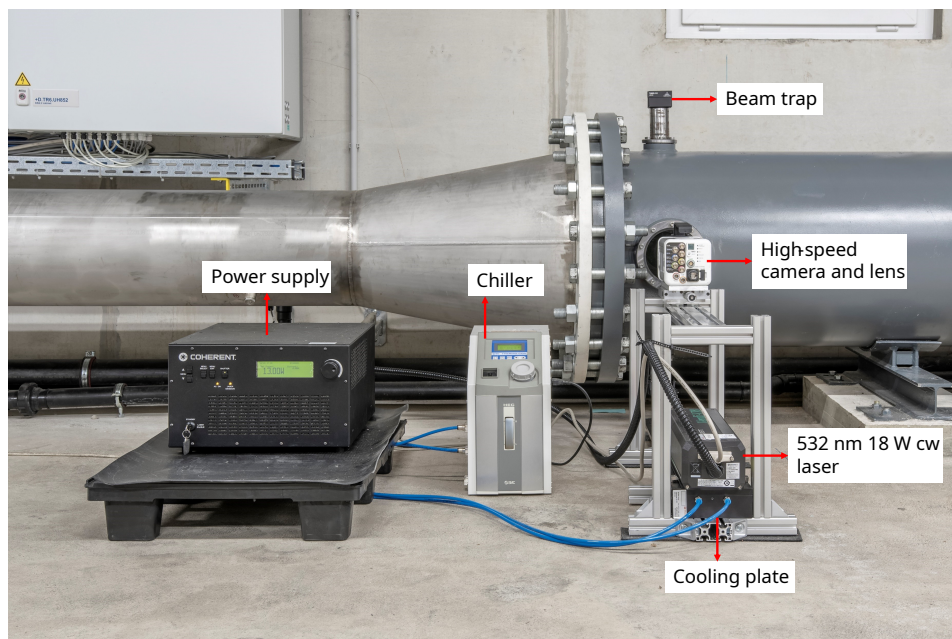


Figure 5.9: Overview of the different components of the reversed IPI setup. Demineralised water can be circulated with the blue tubes, causing the cooling plate, and indirectly the laser, to drop in temperature. The sheet optics are located behind the laser and cooling plate but are not visible here. A close-up of these components is shown in Figure 5.10

Since the laser beam of the 532 nm cw 18 W coherent laser is mostly perpendicular polarised (P-Polarisation: S-Polarisation = 100:1), the ZOWHP and polarising beam splitter are removed from the setup. Instead, a LaVision sheet optic housing is added to the setup in front of the coated mirror to increase the width of the laser beam (Figure 5.10). This housing consists of a plano concave spherical and meniscus lens (Figure 5.11). Increasing the distance between these lenses increases the laser

beam width. By increasing the distances between these lenses, the centre of mass of the sheet optic housing is shifted towards the coated mirror (Figure 5.10a). Due to the instabilities in the set-up of the housing causing vibrations in the laser beam as this distance was increased, it was impossible to set the distance between the lenses inside the sheet optic housing to its maximum.

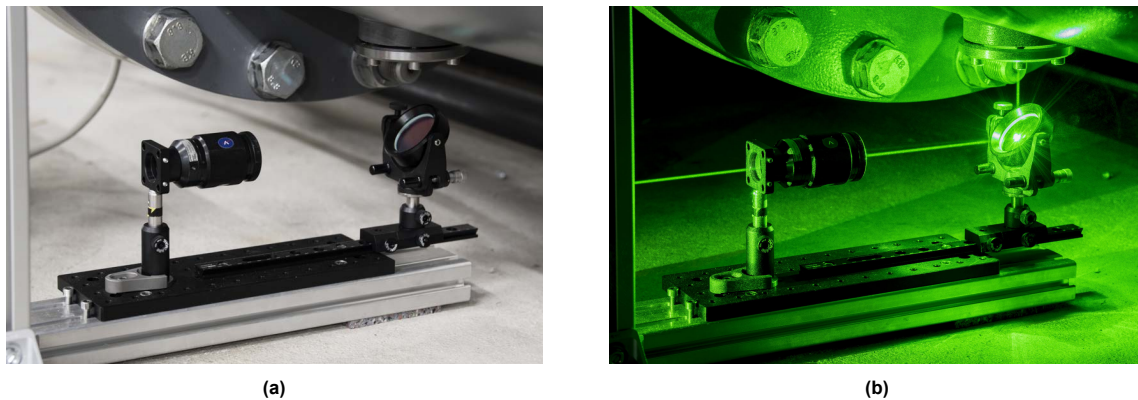


Figure 5.10: Close up of the sheet optics when a) the laser is not operating, b) the laser is operating. The laser beam first enters the sheet optics housing and is then projected into the bottom window of the pipe segment by a coated mirror.

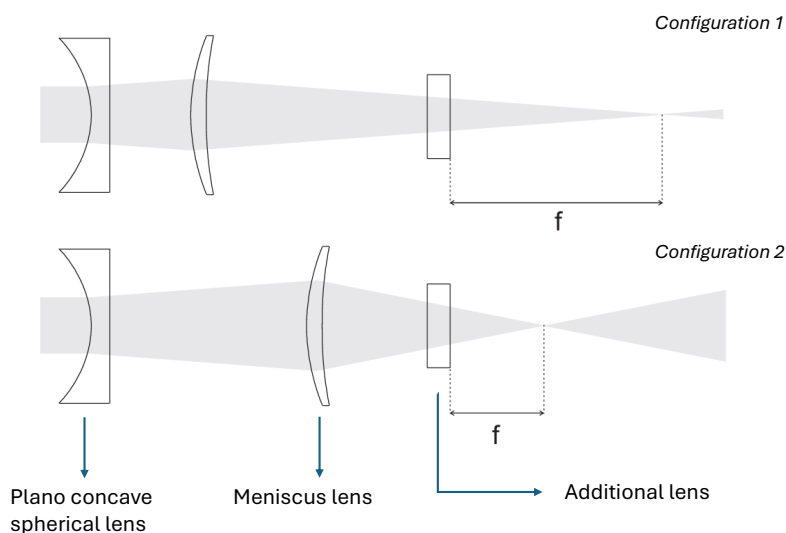


Figure 5.11: Schematic overview of two configurations of the sheet optic housing consisting of a plano concave spherical and meniscus lens. Since the plano concave spherical lens diverges lights, increasing the distance between the plano concave spherical and meniscus lens increases the laser beam width. An additional lens can be mounted to the sheet optic housing to manipulate the laser beam. Modified from LaVision GmbH [80]

5.2.4. Measurement procedure

During this study, the influence of microbubbles on cavitation around the blades of an RD-188 type Francis is studied. Microbubbles are measured with IPI at a location upstream of the turbine model. In Figure 5.12, this position is referred to as the *Measurement position*. By positioning the setup upstream of the model, the hypothesis is that mostly air bubbles will be observed instead of cavitation bubbles. From this, a relation between these air bubbles and the cavitation observed around the blades can be found.

Cavitation is observed around the runner of a Francis turbine model indicated by the red cross in Figure 5.12 using a stroboscope positioned underneath the runner. Additionally, a flow meter, measuring the discharge of water, and an absolute pressure sensor are located next to the IPI set-up. From the

discharge and cross-sectional area of the pipe segment, it is possible to determine the velocity of the fluid at the measurement position (U_{IPI} (m/s)), thereby determining the fps of the camera:

$$fps_{IPI} = \frac{1}{M_0} \cdot \frac{U_{IPI}}{N_{px} \cdot L_{px}} \quad (5.14)$$

where N_{px} is the number of px on the images. Here, L_{px} is $20 \mu\text{m}$, and M_0 follows from the camera calibration. For a maximum velocity of 2.0 m/s and images with a size of $1024 \times 1024 \text{ px}$, the camera's maximum frame rate is roughly 41. Since this frame rate cannot be installed, a fps of 60 was used for the measurements in this study. Secondly, the shutter speed of the camera is set such that the amount of blur in the images is minimal, such that the fringe patterns can be analysed. In this study, a motion blur of 1 px is desired, equivalent to a px size of $40 \mu\text{m}$. From this, the shutter speed of the camera can be determined as follows:

$$t_s = \frac{MB}{U_{IPI}} \quad (5.15)$$

where t_s , MB and U_{IPI} are the shutter time in μs , motion blur in μm and the flow velocity in $\mu\text{m}/\mu\text{s}$.

During every measurement, the absolute pressure at the measurement location is measured. This pressure consists of the following terms:

$$p_{ml} = p_a + \rho_w g \cdot (H_m + H_s + \Delta h) + p_{loss} \quad (5.16)$$

where p_{ml} , Δh and p_{loss} are the absolute pressure at the measurement location, the height difference between the centre of the model turbine runner and the measurement position and the pressure losses, respectively. The height difference between the turbine runner and the measurement position is approximately 5 m, resulting in an additional 0.5 bars measured by the pressure sensor. During the measurements, the model head H_m is set, while the suction head H_s is varied, thereby changing σ (Section 4.5). The pressure losses p_{loss} consist of all losses in the test rig. For each pressure term, the average value during a measurement is considered for further processing.

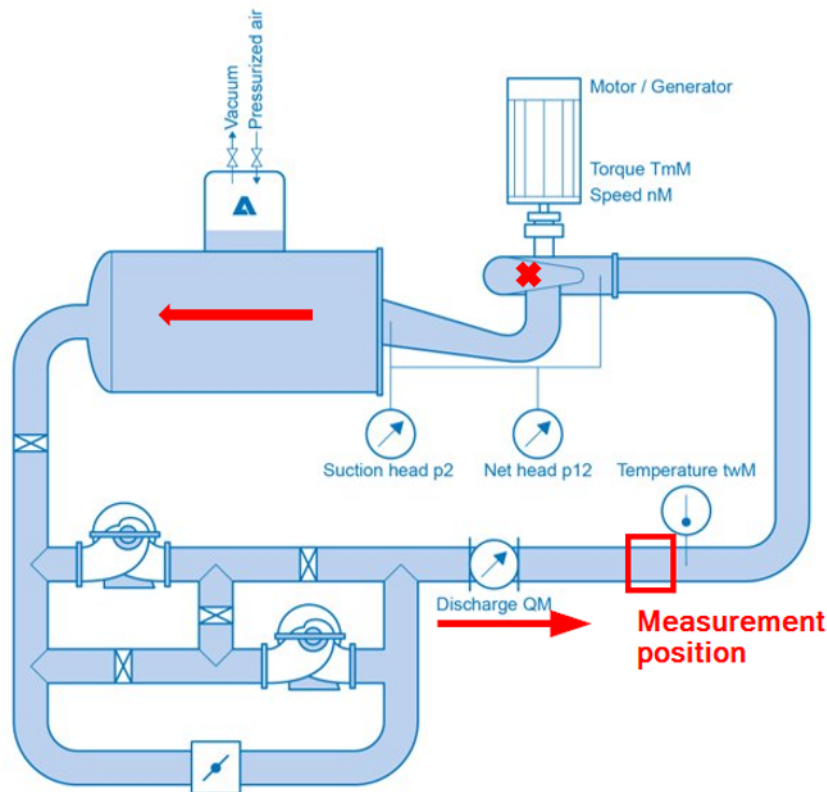


Figure 5.12: Schematic of the test rig of Andritz Hydro located in Linz. The red cross and red arrows indicate the location of the turbine's runner and the flow direction, respectively

In this study, IPI measurements are conducted at two different working points of the Francis RD-188 Type turbine. One of these points is considered a critical point of the turbine, as it is observed at the edge of the continuous operating range of the turbine in the Hillchart (Figure 4.7). At this point ($n_{ED}=0.2234$, $Q_{ED}=0.2293$ and $AOA=20.3^\circ$), a cavitating vortex is observed at the outlet of the runner (Figure 4.11b). The second working point ($n_{ED}=0.2234$, $Q_{ED}=0.1773$ and $AOA=15^\circ$) that is considered is found in the vortex rope free zone of the turbine, i.e. no cavitating vortex appears at the outlet of the runner (Figure 4.11a).

For both working points, the different measurements considered in this study are illustrated in Table 5.1. For measurements 1 and 2, the cavitation number (Equation 4.5) is lowered for different DO concentrations, thereby relating the microbubble content in the test rig to cavitation observed around the runner. This includes the relation between the microbubble content and σ_i and $\sigma_{\eta,1}$. The goal of comparing the two measurements is to find a relation between the cavitating vortex and the microbubble content measured with the IPI technique. During measurement 3, a small air concentration is injected in a low-pressure region above the runner to observe. During measurement 4, measurement 2 is repeated with fresh tap water. In contrast to measurement 4, all measurements are performed with old storage water in the test rig. The goal of measurement 4 is to observe the relation between the microbubble content and the change in water quality. The goal of measurement 5 is to observe the change in microbubble content over time, thereby affecting the cavitation observed around the runner.

Table 5.1: Overview of the measurements performed during this study. The amount of air injected (measurement 3) is a function of the discharge at model scale (Q_m). All measurements, except for measurement 4, are performed with storage tank water, while measurement 4 is conducted with fresh tap water.

Measurement type	DO concentration
a. Presence of a cavitating vortex $(n_{ED}=0.2234, Q_{ED}=0.2293, AOA=20.3^\circ)$ 1. DO variation	3.5, 5.5 and 8.5 mg/L
b. Absence of a cavitating vortex $(n_{ED}=0.2234, Q_{ED}=0.1773, AOA=15^\circ)$ 2. DO variation 3. Air injection 4. Freshwater replacement 5. Repeatability tests	3.5, 5.5 and 8.5 mg/L Initially 3.5 mg/L with injection of 0.5 % and 1.0% of Q_m 3.5, 5.5 and 8.5 mg/L 5.5 mg/L

For all measurements, the cavitation number is decreased by increasing the suction head H_s , following the principles of sigma break curves (Section 4.5). Due to the limited power of the vacuum pump, microbubbles can only be measured at a small pressure range under identical test conditions. This is because the pressure difference between the runner and the tank downstream of the turbine, indicated by H_s , cannot exceed an absolute vacuum of 1 bar. Measuring the microbubble content under a larger pressure range is possible by changing the head of the model, thereby changing the runner speed (Equation 4.9). The different runner speeds and corresponding test rig parameters used for the measurements are illustrated in Table 5.2.

Table 5.2: Operating conditions for the sigma break curves for $n_{ED}=0.2234$ and $Q_{ED}=0.2293$. The subscript m denotes the model scale.

n_m (rpm)	H_m (m)	Re_m
800	28.65	$3.54 \cdot 10^6$
1000	44.76	$4.42 \cdot 10^6$
1200	64.45	$5.30 \cdot 10^6$

Simultaneously with the IPI measurements, cavitation around the turbine model's runner is observed visually. In this study, a cavitating vortex is observed at the critical working point ($n_{ED}=0.2234, Q_{ED}=0.2293, AOA=20.3^\circ$), while gap (and surface) cavitation are observed at both working points. Although the cavitating vortex appears at higher cavitation numbers compared to the other forms of cavitation observed in this study, it does not erode the runner blades. Hence, the microbubble content is related to gap cavitation to determine σ_i and $\sigma_{\eta,1}$ of the runner. For all forms of cavitation observed, the microbubble content is also related to the dynamics of cavitation.

6

Post processing of IPI data

In this chapter, the different steps necessary to post-process the IPI data are described. First of all, an overview of the different steps necessary to detect microbubbles and determine the spatial frequency of their fringes is given in Section 6.1. Thereafter, this data is post-processed in order to determine the microbubble content. This includes the calibration of the IPI technique and a determination of the resolution and the concentration as described in Sections 6.2.1-6.2.3.

6.1. Bubble detection

To detect microbubbles, the images recorded by the high-speed camera need to be processed. The steps involved in this process are listed in Table 6.1a and follow the methodology of Stigter *et al.* [67]. Figure 6.1b shows an IPI image of the dataset on which the steps inside Table 6.1a have been performed in this section.

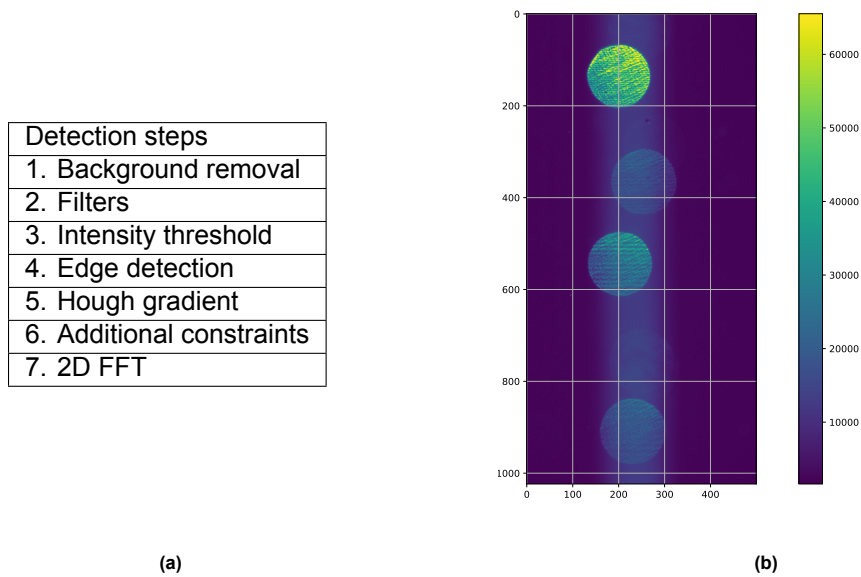


Figure 6.1: a) Chronological order of steps that are used to detect microbubbles. b) Example IPI image.

The first six steps of the bubble detection method applied to the example IPI image (Figure 6.1b) are illustrated in Figure 6.2. The process starts by removing the background from the images to make the particles in the images more visible (Figure 6.2a). The background is removed by subtracting an image of the laser beam with a minimum of particles visible from the images in a dataset. The elimination of the laser makes it easier to detect microbubbles. Next, a mean filter, also known as a Gaussian filter, is applied to the images to blur them. This filter uses a 5x5 px kernel. More information regarding kernel filters can be found in Section A.1. The result of this filter is illustrated in Figure 6.2b. Thereafter, an intensity threshold I_{th} is applied to the images. Only the parts of the images with an intensity above I_{th} are used for further image processing. The minimum value should be chosen so that particles are recognised without accepting too much of the remainder of the image (Figure 6.2c). Setting I_{th} too low makes circle detection using the Hough gradient method challenging, while setting it too high reduces the number of microbubbles detected by the Hough gradient method.

Using a Canny edge detection, the edges of accepted regions are found (Figure 6.2d). These edges serve as a basis for the Hough gradient method. More information on the principles behind this technique can be found in Section A.2. Throughout data processing, most parameters of this method remained constant, including R_{min} and R_{max} . These parameters were set to 65 and 85 px, respectively. This interval is chosen to account for the variation in the position of microbubbles, which results in a different image disk size (Figure 5.6). Another parameter, D_{min} , is set to 25 px but lowered in some datasets to detect more overlapping particles. dp , $p1$ and $p2$ were set to 2.8, 10 and 80, respectively.

The results of the Hough gradient are illustrated by Figure 6.2e. Although the Hough gradient method is an effective method to detect particles, more circles are often detected by this method than desired. Two additional constraints are applied to reduce the number of these circles. First of all, the area of a particle must be at least 60 % of the circle found by the Hough gradient method. Secondly, the difference between the centre of the circles (Figure 6.2e) and the centre of mass of the yellow areas (Figure 6.2c) must be less than 0.05. Circles that meet these criteria are marked with a blue edge (Figure 6.2f) and are further analysed.

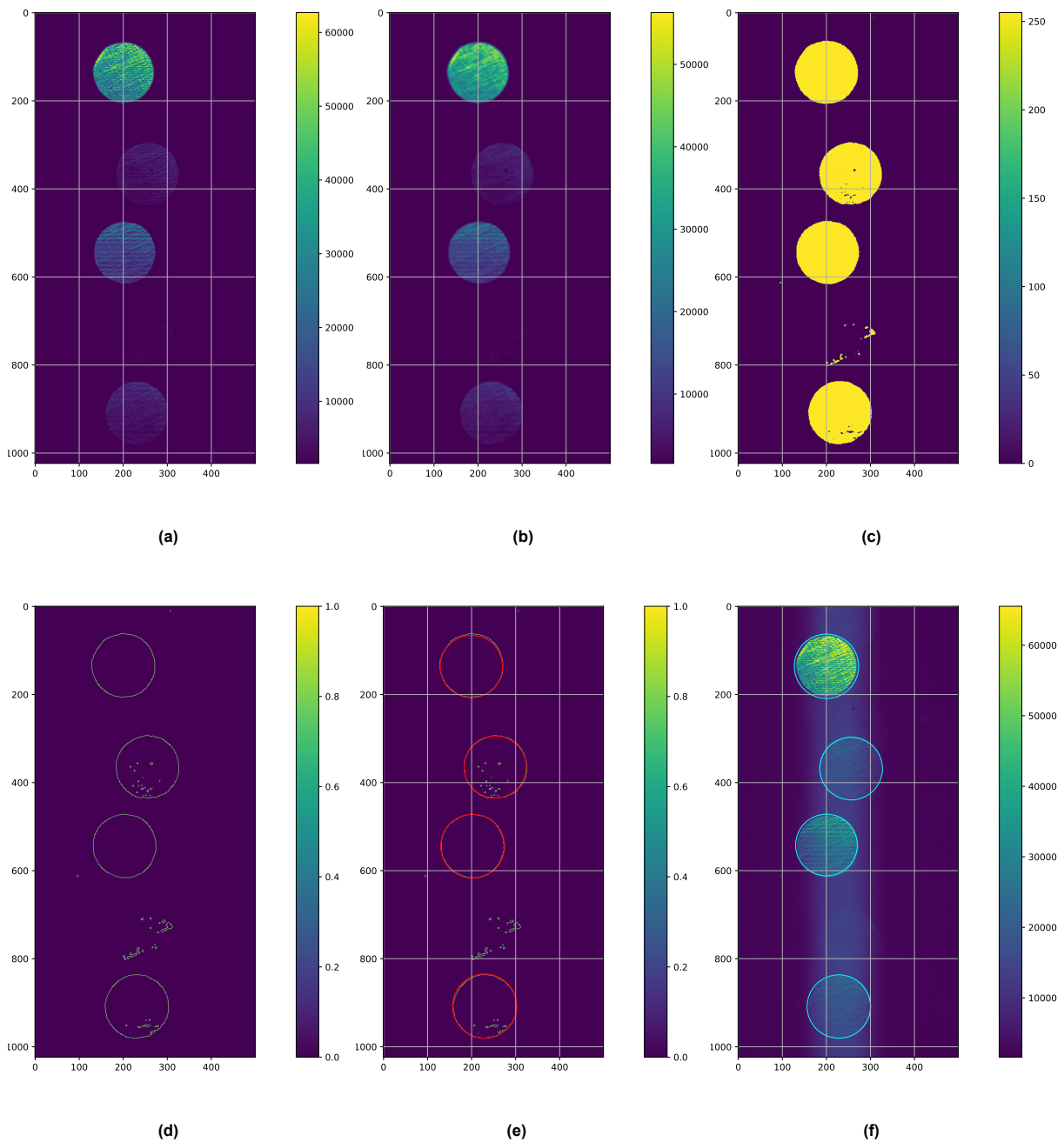


Figure 6.2: Image processing steps that are used to detect circular image disks. In chronological order: a) background removal, b) filter application, c) intensity threshold, d) edge detection, e) Hough gradient, f) Accepted circles after additional constraints. Figures 6.2a-6.2b and 6.2f have identical legends representing the intensity of the px in the figures. The range of the legend of Figure 6.2c is smaller due to the application of the intensity threshold. Finally, Figures 6.2d-6.2e show an equivalent legend with a maximum corresponding to the maximum value of the Canny edge detection.

The final step of the image processing involves the application of a 2D FFT to determine the spatial frequency of the fringes visible on the disks. With this information, it is possible to determine the size of the microbubbles (Equation 3.5). However, a few steps must be executed before applying a 2D FFT, which follow the procedure described by Stigter *et al.* [67]. Some of these steps are illustrated in Figure 6.3. If disks on the images overlap (step 1), the overlap should be removed (step 2). For both disks, the largest possible rectangle that fits the non-overlapping region is drawn (step 3). In this region, a

2D FFT is applied. This step is also applied if microbubbles are not overlapping, as this also prevents the edge of the disks from being considered in the analysis. This is because the gradient between the background of the image and the edge of the disks results in an additional spatial frequency found by the 2D FFT. After step 3, a 2D Hann filter is multiplied to the rectangular areas to reduce the amount of spectral leakage. More information on 2D Hann filters can be found in Section A.1. Finally, a 2D FFT is applied, which results in a PSD of spatial frequencies. From this, the fringe frequency of a microbubble follows.

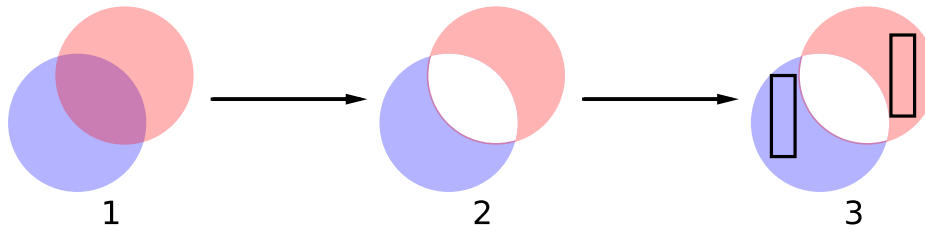


Figure 6.3: Circle modifications performed on particles before applying a 2D FFT. If particles overlap (step 1), the overlap is removed (step 2). From the remains of these particles, the largest possible rectangle is drawn (step 3). This step is also performed when there is no overlap between particles. The edges are excluded from these rectangles as the FFT will find an additional spatial frequency coming from the gradient between the edges of the circles and the background. After these steps, a 2D Hann and a 2D FFT are applied.

6.2. Postprocessing of microbubble data

After applying the steps shown in Table 6.1a, the size of every microbubble inside the measurement volume can be determined. To determine the size and concentration of these microbubbles measured, some additional steps must be performed. This includes calibrating the IPI data and determining the resolution and concentration of the microbubbles. This aligns with the method described by Stigter *et al.* [67].

6.2.1. IPI calibration

The parameters in Equation 3.5 should be calibrated before determining the size of the measured microbubbles. These parameters are κ , α and D_{px} , where the last two are a function of z_0 . Additionally, parameters related to the laser illumination should be calibrated to determine the concentration of microbubbles. This includes the width of the laser beam δ_{beam} and the proportionality constant \tilde{I}_0 .

To calibrate κ for $\theta=90^\circ$, a fringe pattern can be simulated over a wide range of diameters with a Mie Scattering algorithm, such as implemented in the python library *PyMieScatt*. This results in a relation between the diameter of microbubbles and κ , as illustrated in Figure 3.4. Depending on the wavelength of the light source, the value for κ changes. During this study, the results from the calibration of Russell *et al.* [17] are used, as the same scattering angle and wavelength were used. For microbubbles with a diameter larger than $30 \mu\text{m}$, κ has a value of $39.32 \mu\text{m}/^\circ$ with a deviation of $0.22 \mu\text{m}/^\circ$. At smaller diameters, the uncertainty in κ is higher. However, it is expected that most of the microbubbles have a diameter larger than $30 \mu\text{m}$.

The calibration of α is performed by means of a camera calibration, as discussed in Section 5.1. Due to a change in the medium between the camera calibration and the IPI measurements, the value of α is reduced as the refractive index of water is higher than of air. However, there is not a single α that describes the entire range of microbubbles measured. This is because the microbubbles are not all positioned at the same distance from z_1 . Instead, α should be determined as a function of z_0 for every microbubble. This can be achieved by rewriting Equation 5.12 to find z_0 corresponding to the image

disk diameter of the microbubble considered:

$$z_0 = \frac{z_1 n D_{px}}{M_0 D_a - D_{px}} \quad (6.1)$$

For known z_0 , it is possible to determine α with Equation 5.13.

The remaining parameters that need to be calibrated focus on the illuminated intensity of the measured microbubbles. Instead of directly considering the intensity of the microbubbles, a part of the microbubbles is removed from the dataset. Microbubbles and other particles discarded from the calibration do not satisfy the constraints listed in Table 6.1. Here, a , b , α_{tf} and I_{BD} denote the x and y coordinates of the centre of a particle, the tilt in a fringe pattern and the bit depth of the camera, respectively. For large datasets, 20 to 30 % of the particles are discarded from the dataset, caused mainly by an orientation in the fringe pattern. For small datasets, this can lead up to 95% of particles discarded. This is mainly due to the relatively large number of other particles measured with the IPI technique at low DO concentrations and high values of σ . To illustrate this, from a large dataset containing 15416 particles, 75.5% of the particles satisfied the conditions from Table 6.1, with 61% of the particles discarded by a tilt in the fringe pattern. In contrast, for a smaller dataset containing 1323 particles, only 5% of the particles satisfied the conditions from Table 6.1, with 98.4% of the particles discarded by a tilt in the fringe pattern.

Table 6.1: Overview of the parameters constraining the number of microbubbles selected to determine the microbubble content. Here, a , b , x_{edge} and y_{edge} represent the centre coordinates of a circular disk and the px values of the x and y edges of the IPI images. α_{tf} denotes the tilt in the fringe pattern. Microbubbles that satisfy all constraints are used to estimate the microbubble content.

Parameter	Constraint
(a, b)	$ x_{edge} - a \geq 85 \text{ px}, y_{edge} - b \geq 85 \text{ px}$
$SNRN$	$SNRN \leq 15 \text{ dB}$
α_{tf}	$\alpha_{tf} \leq \pm 0.05 \text{ rad}$
I	$I \geq I_{th}$ and $I \leq I_{BD}$

From the set of accepted microbubbles, the normalised intensity of each microbubble is computed. Normalising the intensity removes the effect of larger image disks being darker, as the light has to be spread over a larger area. This can be accounted for as follows:

$$\tilde{I} = I \left(\frac{D_{px}}{D} \right)^2 \quad (6.2)$$

where \tilde{I} and I are the normalised and given intensity of a microbubble. For a given D_{px} , α and λ , it is possible to write Equation 6.2 as:

$$\tilde{I} = I \left(\frac{\alpha \lambda}{\kappa} \right)^2 \quad (6.3)$$

For every microbubble, the normalised intensity can be plotted against its position in the image. It is expected that the normalised intensity of these microbubbles can be described by a Gaussian distribution. This is due to the intensity profile of a laser, which normally follows a Gaussian distribution as well. This distribution is obtained by first developing a histogram of the microbubbles. For every bin of the histogram, the 95th percentile is calculated based on the intensity of the microbubbles in the bin. From this, a Gaussian distribution of the normalised intensity is derived:

$$\tilde{I}_s = \tilde{I}_0 \exp \left(-\frac{(x - x_0)^2}{\delta_{beam}^2} \right) \quad (6.4)$$

where x_0 and x are the centre of the laser beam and the distance from the centre of the microbubbles to the centre of the laser beam, respectively. The centre of the laser beam is found by taking the mean value of the image disk sizes and using this to determine z_0 with Equation 6.1

From the out-of-focus distance, it is also possible to determine the magnification corresponding to that distance. With the magnification, the distance x is converted to mm. With these parameters, the Gaussian distribution for larger datasets is developed. An example of this is shown in Figure 6.4a. Here, the red dots represent the microbubbles that are accepted from the dataset, while the black and blue curves represent the 70th percentile line and Gaussian distribution, respectively. From Figure 6.4a it can be concluded that almost all microbubbles are located near the centre of the laser beam and do not entirely follow a Gaussian distribution. This is caused by the laser beam, whose intensity does not follow a Gaussian distribution itself (Figure 6.4b).

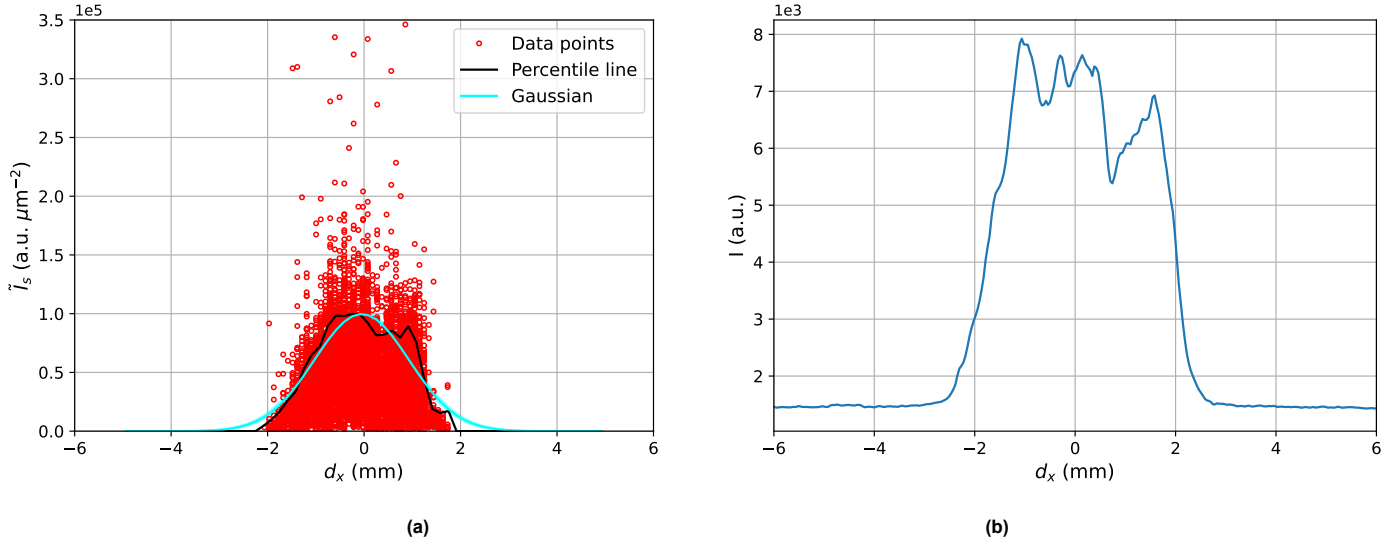


Figure 6.4: Intensity profile from a) a dataset of microbubbles as a function of the distance from the laser beam centre in the x-direction, b) the laser beam as a function of its centre. From the dataset of microbubbles, the 70th percentile for different distances d from the beam centre in the x-direction is determined, from which a Gaussian distribution is obtained. The set of microbubbles does not entirely follow a Gaussian distribution caused by the shape of the laser beam.

6.2.2. Resolution

As described in Section 3.2.3, the range of microbubbles that can be measured with IPI is limited. The lower limit D_{min} is found by considering the minimum number of fringes in a disk (Equation 3.7). For every microbubble in the dataset, it is possible to determine α as a function of z_0 and thus calculate the diameter of the microbubble. In this study, a minimum diameter of $11.2 \mu\text{m}$ was found. The upper limit D_{max} follows from the Nyquist frequency (Equation 3.8) and is $505.5 \mu\text{m}$. However, the size of the image disks depends on z_0 and thus affects the size of the microbubbles. As the image disks become larger far away from the focal plane, the largest microbubble that can be measured is located as far from the focal plane as possible. However, the distance to the focal plane and thus the maximum bubble size is limited by the applied intensity threshold. This can be accounted for by relating the bubble size to its image intensity. Although the intensity of the laser beam itself does not follow a Gaussian distribution, the intensity of the microbubbles is estimated with a Gaussian as follows [67]:

$$I(\delta) = \tilde{I}_0 \cdot \exp\left(-\left(\frac{\delta}{\delta_{beam}}\right)^2\right) \cdot \frac{D^2}{D_{px}^2} \quad \text{with} \quad \delta = z_0 - r_0 \quad (6.5)$$

where δ and r_0 are defined as the distance between the laser beam centre and the focal plane, and to the position of a microbubble. Equation 6.5 shows that the intensity is proportional to the bubble size and inversely proportional to the image disk size. This is because a larger bubble can scatter more light and will thus be brighter, whereas a larger image disk size means that the intensity of the laser has to be spread over a larger area [81]. For unknown bubble sizes, D can be rewritten with Equation 3.5. Because α in Equation 3.5 depends on z_0 , α can be rewritten with Equation 5.13. Substituting these terms in Equation 6.5 results in:

$$I(\delta) = \tilde{I}_0 \frac{\kappa^2}{4\lambda^2} \cdot \left(\tan^{-1} \left(\frac{D_a/2}{z_1 n + \delta + r_0} \right) \right)^{-2} \cdot \exp \left(- \left(\frac{\delta}{\delta_{beam}} \right)^2 \right) \quad (6.6)$$

To find the maximum microbubble diameter free of aliasing, the Nyquist frequency should be applied to Equation 6.6 by substituting $\lambda = 2$ px. Setting Equation 6.5 equal to I_{th} and solving this for δ , gives an estimation for δ . At a position closest to the camera, the maximum collection angle and largest disk size are found. Both D_{px} and α can be found by replacing z_0 with $\delta + r_0$ in Equations 5.12 and 5.13, respectively. For a given dataset, this results in an α_{max} of 7.1° , a $D_{px,max}$ of 192.6 px and a corresponding D_{max} of 536.4 μm . These values differ slightly depending on the dataset.

Between the lower and upper size limits of microbubbles that can be measured with IPI, a part of these bubbles cannot be analysed. The lower limit of this region is formed by the intensity of the smallest bubbles. As the amount of scattering light reduces for smaller microbubbles, the intensity of these bubbles is rather low. As an intensity threshold is applied to each dataset, these microbubbles with an intensity below the threshold are not selected. Hence, the minimum microbubble size based on the intensity can be found as follows:

$$D_{min,I} = D_{px} \cdot \sqrt{\frac{I_{th}}{\tilde{I}_0}} \quad (6.7)$$

The upper limit is defined by I_{BD} and indicates the saturation in an image. In the case that a large microbubble is positioned at or near the laser beam centre, such a microbubble can get too bright to analyse the fringe pattern inside the disk. The size of a microbubble where this can be observed is determined by:

$$D_{max,I} = D_{px} \cdot \sqrt{\frac{I_{BD}}{\tilde{I}_0}} \quad (6.8)$$

It should be noted that both limits depend on \tilde{I}_0 , which follows from the Gaussian distribution of the normalised intensity of the microbubbles. As it becomes more difficult to develop a Gaussian from small datasets, only large datasets are considered to determine $D_{min,I}$ and $D_{max,I}$. From these datasets, $D_{min,I}$ and $D_{max,I}$ are found to be 18.2 and 140.2 μm , respectively.

6.2.3. Concentration estimation

The concentration of microbubbles measured in each data set can be determined as a function of the number of bubbles and the measurement volume:

$$c = \frac{N_b}{V} \quad (6.9)$$

where N_b and V are the number of microbubbles and the measurement volume in cm^3 , respectively. The first parameter is found by setting some constraints to the microbubbles found by the bubble detection method, described in Section 6.1. These constraints are illustrated in Table 6.1. Microbubbles that satisfy all conditions are used for further postprocessing. The second parameter, the measurement volume, can be determined as follows:

$$V = AL_b N_{img} \quad (6.10)$$

where A , L_b and N_{img} are the effective cross-sectional area, the length of the laser beam and the number of images within the dataset, respectively. The number of images follows directly from the datasets and the length of the laser beam can be calculated by multiplying the size of a px with the length of the images in the direction of the laser. However, it is not possible to determine A directly from the images. This is because A is altered by the presence of microbubbles. First of all, from Equation 6.5 it follows that the width of the laser beam is proportional to D^2 . Secondly, A is lowered by the effects of saturation, which occur when large microbubbles are measured. This is because the amount of light that can be scattered by a microbubble increases with the size of that microbubble. If these

microbubbles are positioned near the centre of the laser beam, saturation can occur. To account for both effects, A is calculated in the following way [67]:

$$A = A_c - A_s \quad (6.11)$$

where A_c and A_s are the cross-sectional area and saturation areas of the laser beam based on the size of microbubbles that are measured.

With this data, the concentration of microbubbles is calculated for different microbubble sizes, resulting in a concentration distribution. However, some of the parameters necessary to calculate this have an uncertainty. An overview of these parameters is shown in Table 6.2. The uncertainty from the Gaussian parameters is a result of fitting a Gaussian distribution through the percentile line of the normalised intensity of the microbubbles, whereas the uncertainty of the other parameters follows from the measurements. Multiple iterations are performed using a Monte Carlo algorithm to determine the concentration distribution of the microbubbles in each dataset. In this study, 500 iterations are performed to make sure that the solution converges. Although it is possible to determine the sample size of microbubbles with this algorithm for each dataset, obtaining the measurement volume per bin becomes more difficult as the size of a dataset decreases. Since the measurement volume does not drastically change between the datasets, the measurement volume of a larger dataset is used to estimate the distributed concentration of microbubbles in smaller datasets.

Table 6.2: Overview of parameters and their uncertainty that are used to calculate the size and concentration of microbubbles.

Parameter	Uncertainty
λ	$\lambda^2 \cdot \sigma_f$ (Equation 3.9)
D_{px}	$\sigma_{D_{px}}$ (Equation 3.10)
κ	Std from Russell <i>et al.</i> [17]
z_1	Std from camera calibration (Section 5.1.4)
M_0	Std from camera calibration (Section 5.1.4)
Gaussian parameters \tilde{I}_s, x_0 and σ	$\tilde{I}_{s,std}, x_{0,std}$ and σ_{std}

For every iteration, a distribution of the number of microbubbles and the measurement volume is obtained. An illustration of the measurement volume is shown in Figure 6.5. From this graph, it can be concluded that the measurement volume increases as a function of the microbubble size until saturation occurs. The microbubble size corresponding to saturation is calculated with the I_{BD} of the camera, as shown in Equation 6.8. After saturation, the measurement volume remains constant until the microbubble size reaches the Nyquist limit. This shows that the maximum microbubble diameter limits the measurement volume. Between the datasets, a similar trend in the measurement volume is observed, although the values for $D_{max,I}$ and D_{max} vary slightly.

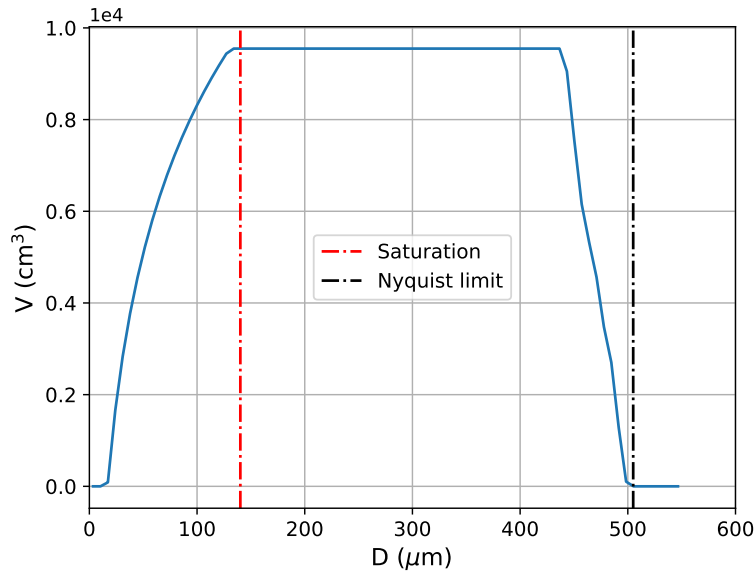


Figure 6.5: Relation between the measurement volume and the diameter of microbubbles. The volume increases until microbubbles are saturated, starting at $D=140.2 \mu m$. The measurement volume goes to zero around the Nyquist limit, which is found at $D=505.8 \mu m$. These values are found at the critical working point ($n_{ED}=0.2234$, $Q_{ED}=0.2293$, $AOA=20.3^\circ$) at $n=1000$ rpm, $DO=8.5$ mg/L and $H_s=7.30$ m and vary slightly for different datasets.

The microbubble concentration distribution from the same dataset as used for the illustration of the measurement volume (Figure 6.5) is illustrated with Figure 6.6. Here, the mean concentration of all iterations of the Monte Carlo simulation is indicated by the blue curve, while the 5th to 95th percentile interval is indicated with the shaded area. The uncertainty in the concentration is caused by uncertainties in both the estimation of the microbubble size and volume as well as the uncertainty in the statistics used [67]. Here, the uncertainty in the first two contributors is caused by the uncertainty in parameters listed in Table 6.2. The uncertainty in the microbubble size plays an important role for small microbubbles, whereas the uncertainty in the measurement volume is more significant over the entire spectrum [67]. The uncertainty in statistics is significant when the number of microbubbles is small, which is mostly the case for relatively small and large microbubble diameters [67]. Furthermore, this effect is visible over the entire range of measured microbubbles measured when the DO concentration is low, resulting in small datasets.

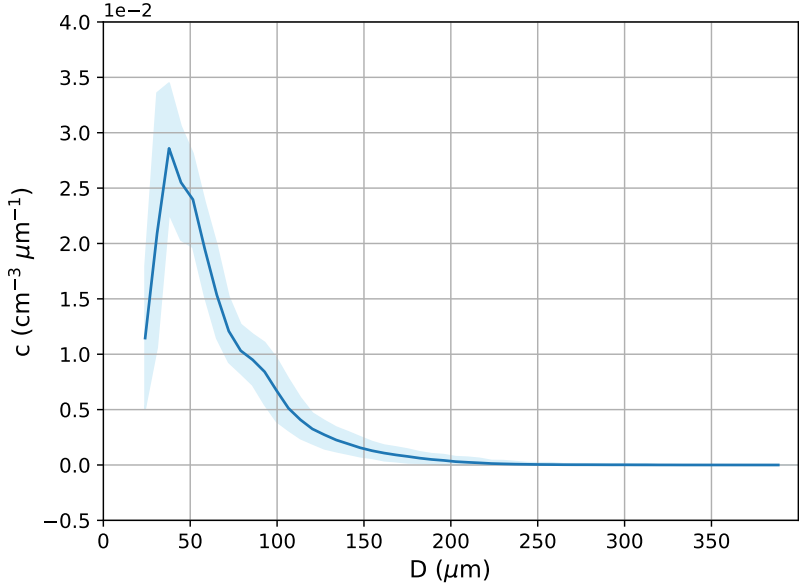


Figure 6.6: Concentration distribution of microbubbles measured at the critical working point ($n_{ED} = 0.2234$, $Q_{ED} = 0.2293$, $AOA = 20.3^\circ$) at $n = 1000$ rpm, $DO = 8.5$ mg/L and $H_s = 7.30$ m. The curve shows the mean concentration of all iterations of the Monte Carlo algorithm, while the shaded area is the 5 to 95th percentile interval of these iterations.

7

Results

In this chapter, the results of the IPI measurements are described. First of all, more information on the regulation of the DO concentration inside the test rig is given in Section 7.1. Next, the effects of different parameters on the microbubble content is given in Section 7.2. Lastly, the role of microbubbles on cavitation observed around the runner of a hydraulic turbine model is discussed in Section 7.3.

7.1. Variation in DO concentration

For all measurements, IPI measurements and cavitation observations were made under different values of σ . For each measurement, the cavitation number was decreased to determine σ_i and $\sigma_{\eta,1}$. The latter follows from the efficiency drop of the turbine's model illustrated with a sigma break curve (Section 4.5). For these curves, the cavitation number is reduced by changing the suction head (H_s) of the test rig (Equation 4.5). For each curve, the goal is to maintain a DO concentration to find a correlation between the DO concentration and the microbubble content. This is, however, impossible as the DO concentration significantly decreases at large values of H_s (Figure 7.1a). Here, the changes in the three DO concentrations (3.5, 5.5 and 8.5 mg/L) are illustrated for different runners' speeds at the critical working point (measurement type 1, Table 5.1). The crosses indicate the inception point of gap cavitation for each curve. From Figure 7.1a some observations can be made. First of all, the drop in DO concentration becomes more pronounced with increasing initial DO concentration. Secondly, for every DO concentration, the drop is observed at higher H_s for lower runner's speeds. For larger DO concentrations, this drop starts once the inception point of gap cavitation is reached, while this is less clear for lower concentrations. This trend is also illustrated in Figure 7.1b, which illustrates the evolution of the DO concentration as a function of H_s in the absence of a cavitating vortex (measurement type 2, Table 5.1).

The trends observed in Figures 7.1a-7.1b are driven by two main mechanisms. First of all, increasing the value of H_s does not only decrease the cavitation number but also increases the vacuum applied to the tank downstream of the turbine model (Figure 4.8b), thereby reducing the DO concentration inside the test rig. This reduction is only possible if the water is saturated with oxygen under the applied operating condition, while oxygen will dissolve in undersaturated water (Section 2.3.3). By increasing the value of H_s , the pressure in the test rig is reduced, thereby lowering the saturated DO concentration c_{sat} . At high DO concentrations, the water will be saturated at a higher pressure compared to low DO concentrations, while oxygen will dissolve at these pressure levels at low DO concentrations. Hence, the effects of the applied vacuum are more pronounced at higher DO concentrations. Secondly, cavitation emphasizes this process, as oxygen can diffuse into cavitation bubbles, thereby increasing their size and decreasing the DO concentration further. At lower DO concentrations, the relation between σ_i and the decrease in DO concentration is less significant because fewer microbubbles are available to act as nuclei and thus initiate cavitation. Although the same principles hold for the different working points, the reduction in the DO concentration is observed at higher values of H_s at the non-critical working point ($n_{ED}=0.2234$, $Q_{ED}=0.1773$, $AOA=15^\circ$), under the same operating conditions of the test rig. This amplifies the relation between the reduction in the DO concentration and the inception point of the turbine.

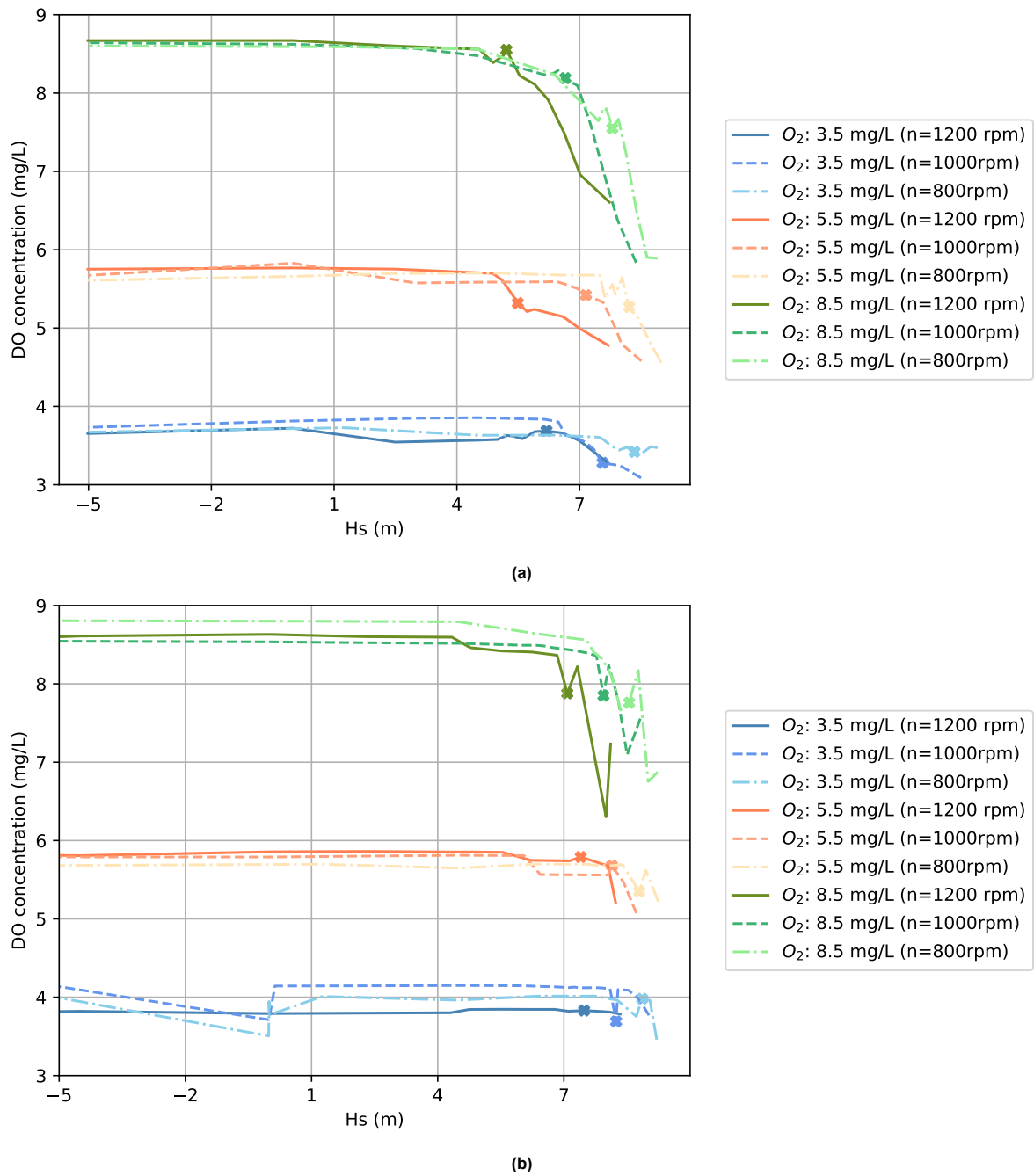


Figure 7.1: Time-averaged DO concentration for different values of H_s at different runner speeds of the Francis 188 RD Type for a) condition 1: the presence of a cavitating vortex, b) condition 2: the absence of a cavitating vortex. The crosses indicate the inception point of gap cavitation for the different conditions. At higher H_s , a vacuum is created downstream of the turbine model, which causes a decrease in the DO concentration. This drop significantly increases once the inception point is reached.

7.2. Microbubble content

For all measurements listed in Table 5.1 the microbubble content measured at the *Measurement position* (Figure 5.12) is analysed according to the procedure described in Chapter 6. The outcome of this procedure for the different measurements can be found in Sections 7.2.1-7.2.5.

7.2.1. DO variation at the critical working point

The first and most extensive part of the measurements consisted of measuring the microbubble content in the presence of a cavitating vortex ($n_{ED}=0.2234$, $Q_{ED}=0.2293$, $AOA=20.3^\circ$) at different runner

speeds and DO concentrations. For each data point, the microbubble concentration distribution was calculated using Equation 6.9. To account for the uncertainty in parameters listed in Table 6.2, the microbubble concentration distribution is calculated multiple times using a Monte Carlo simulation. The total concentration for each data point is found by integrating the microbubble concentration distribution over the microbubble diameter, resulting in a concentration in cm^{-3} :

$$c_t = \int_{D_1}^{D_2} c_{dis} dD \quad (7.1)$$

where D_1 , D_2 and c_{dis} are the minimum and maximum microbubble diameters considered in the microbubble concentration distribution and the concentration distribution, respectively. Equation 7.1 is solved numerically using the Simpson's rule. As this integration is performed on each iteration of the Monte Carlo simulation, a mean concentration and std follow for each data point. For the critical working point, this is illustrated in Figure 7.2 for different runner's speeds and DO concentrations. Here, the dashed lines represent the average concentration of microbubbles, while the shaded areas represent the std in each data point. The black symbols indicate the inception point of gap cavitation.

In general, higher DO concentrations result in a higher concentration of microbubbles, especially at lower values of σ . Moreover, the increase in microbubble concentration is observed at higher values of σ for higher DO concentrations. For example, at $n=800$ rpm, the microbubble concentration increases significantly at $\sigma \approx 0.3$ at a DO concentration of 8.5 mg/L, whereas a similar increase is observed at $\sigma \leq 0.1$ for a DO concentration of 3.5 mg/L (Figure 7.2a). The hypothesis is that this increase is caused by a cavitating vortex appearing at the outlet of the runner. As discussed in Section 2.4.2, the relation between σ_i of TVC and C_L of a hydrofoil is affected by the nuclei content. Following this relation, the cavitation inception at the core of vortices appearing in hydraulic machinery is delayed at lower DO concentrations, as fewer microbubbles are available to act as nuclei. This is because cavitation inception at the core of these vortices is strongly related to the time necessary for nuclei to reach the vortex core, which can be achieved by an axial or radial motion of nuclei [10]. The characteristic time scale necessary to capture nuclei in the vortex core for an axial and radial motion is defined as [10]:

$$\tau_a \approx \frac{1}{n\pi^2 a V} \quad (7.2)$$

$$\tau_r = \frac{3}{4} \frac{\nu}{\omega^2 R^2} \left(\frac{r_0}{a}\right)^4 \quad \text{with} \quad r_0 \approx \frac{2}{3} \frac{1}{\sqrt{\pi n c}} \quad (7.3)$$

where

- τ_a is the characteristic time scale of axial feeding
- n is the nuclei density
- a is the radius of a vortex core
- V is the freestream axial velocity
- τ_r is the characteristic time scale of radial capture
- ω is the rotation rate of a vortex
- R is the radius of a nucleus
- r_0 is the initial position of a nucleus
- c is the chord length of the geometry

For both conditions, the characteristic time scale is inversely proportional to the nuclei density. Hence, at higher DO concentrations and thus a larger concentration of microbubbles, the characteristic time scales are smaller and thus, the cavitation inception at the core of a vortex should be observed at higher values of σ .

Another increase in the microbubble concentration is observed after the onset of gap cavitation, indicated by the black symbols in Figure 7.2. This suggests that cavitation bubbles observed around the gap of the runner appear at the *Measurement position* (Figure 5.12). Usually, these bubbles dissolve in a high-pressure region of a facility (resorber) [7]. At Andritz Hydro, however, test rigs do not contain

a resorber, allowing cavitation bubbles to recirculate in the test rig. It should be noted that although the term cavitation bubbles is used, it is not possible to examine the chemical content of the bubbles measured at the *Measurement position*. However, according to Brennen [7], the vapour inside cavitation bubbles usually condenses at high-pressure regions of a facility, which could result in small air microbubbles measured at the measurement position.

Moreover, for each runner's speed, a small decrease in microbubble content is observed at the data points at the lowest values of σ with a DO concentration of 8.5 mg/L. For smaller DO concentrations, this trend is less visible. Since the DO concentration and microbubble concentration are strongly correlated, it is concluded that the drop in the DO concentration (Figure 7.1a), caused by the vacuum applied to the system and the diffusion of oxygen into cavitation bubbles, causes a drop in the microbubble concentration.

Additionally, for a DO concentration of 3.5 mg/L, only a general increase in microbubble content is observed as a function of σ at a runner speed of 800 rpm. In this study, no link was found between the difference in the evolution of the microbubble concentration over changing σ at different runner speeds for a DO concentration of 3.5 mg/L. A possible cause is a difference in the operating settings of the test rig at different runner speeds, causing a difference in cavitation around the runner and, thereby, a difference in the concentration of cavitation bubbles. However, as the cavitation videos do not show a significant difference in cavitation around the runner, more research into cavitation should be conducted. Simultaneously, the effects of the operating conditions, including the suction head, on cavitation should be considered.

Finally, a large concentration of microbubbles was measured at the data point with the following properties: $n=1000$ rpm, $DO=8.5$ mg/L, $\sigma=0.3324$. The hypothesis is that this significantly large concentration follows from the measurement procedure considered in this study. To elaborate, this data point was the first point taken during that specific measurement day. Before a measurement day, the DO concentration inside the test rig can increase, as the test rig is a closed system. In contrast, in most facilities the DO concentration decreases over time as the systems are open. To reduce the DO concentration, the test rig was degassed to reach the desired DO concentration inside the test rig. This is achieved by increasing H_s , thereby applying a vacuum to the system while simultaneously lowering σ . Hence, by strongly degassing the test rig, cavitation is observed around the runner, resulting in cavitation bubbles observed at the *Measurement position*. Since the time interval between degassing and conducting the IPI measurements was approximately a few minutes, and the characteristic time scale necessary for microbubbles to dissolve is in the order of seconds, another parameter must be causing this large concentration of microbubbles. The hypothesis is that there is a memory effect, indicating that nucleation is more likely to occur if a system contained gas in the past compared to a system without this history [82]. This would indicate that microbubbles are more easily formed in the test rig due to the larger DO concentration before conducting the measurements.

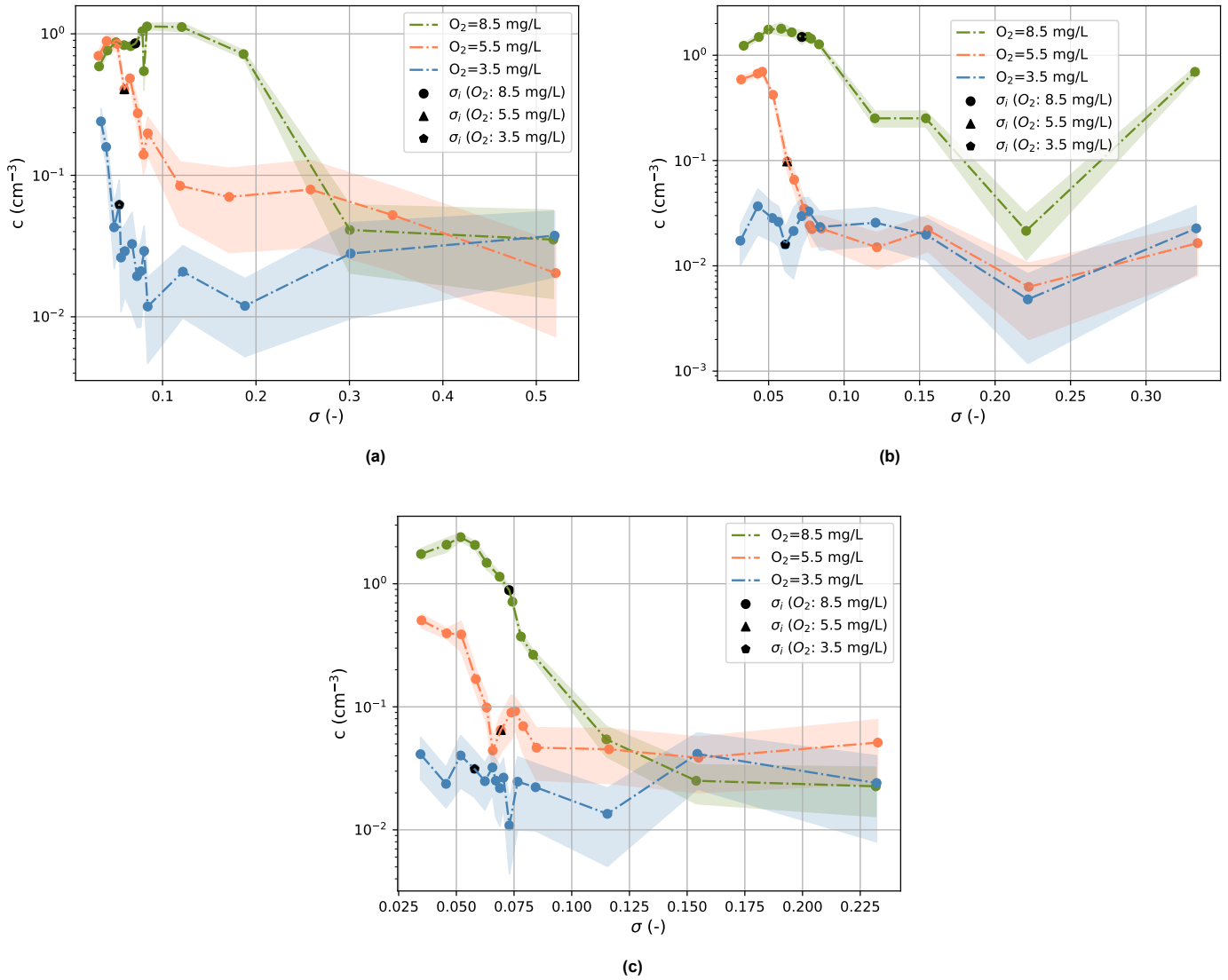


Figure 7.2: Total microbubble concentration as a function of σ at the critical working point ($n_{ED}=0.2234, Q_{ED}=0.2293, AOA=20.3^\circ$) for a) $n=800$ rpm, b) $n=1000$ rpm, c) $n=1200$ rpm. The dashed lines represent the mean concentration obtained by integrating over all Monte Carlo simulations, while the shaded areas represent the standard deviation of this integration. For each curve, the inception point of gap cavitation is illustrated by the black symbols.

In addition to the microbubble concentration, the size distribution of the microbubbles measured at every data point was determined. For each DO concentration, the average microbubble concentration distribution that follows from the Monte Carlo simulation for different σ values for $n=800$ rpm is illustrated in Figure 7.3. The distributions at higher runner speeds can be found in Figure B.1. The number of data points slightly increases as the DO concentration decreases because more measurements were taken near the inception point of the runner. However, it was not known beforehand what the change in σ_i would be as a result of lowering the DO concentration.

Figure 7.3 shows an overall increase in the microbubble concentration distribution as the DO concentration increases. This increase is mostly observed for microbubbles with $D \leq 75 \mu\text{m}$. Moreover, an increase in the microbubble concentration is observed for decreasing σ for each DO concentration. Along with that, larger microbubbles are observed as the pressure at the *Measurement position* is decreased. In contrast to Russell *et al.* [33], a decrease in σ does not always show an increase in the microbubble content. In contrast, the microbubble concentration distribution reduces over the entire range of microbubble diameters for both a DO concentration of 5.5 and 8.5 mg/L when the value for σ is reduced to 0.0314 and 0.0834, respectively. Similar to the drop in microbubble concentration ob-

served in Figure 7.2a, this decrease is caused by a combination of the degassing of the test rig by the vacuum pump and the diffusion of air into cavitation bubbles. It should be noted that the reduction in the microbubble content also occurs before the cavitation inception point. For example, at $n=800$ rpm, $DO=8.5$ mg/L, a reduction in the microbubble content is observed around $\sigma=0.0834$ (Figure 7.3c), while $\sigma_i=0.0708$. This seems to indicate that the onset of cavitation occurs earlier than was determined during the measurements.

Furthermore, the possible effects of the cavitating vortex on the microbubble concentration distribution can be observed by comparing the first two curves ($\sigma=0.5182$ and $\sigma=0.3004$) with the other curves in Figure 7.3c, showing a significant increase in the microbubble concentration. Whereas for the first two curves, a very small concentration of only small microbubbles ($25 \mu\text{m} \leq D \leq 50 \mu\text{m}$) is observed, the concentration of microbubbles is significantly increased over the entire range of microbubble diameters after the onset of a cavitating vortex.

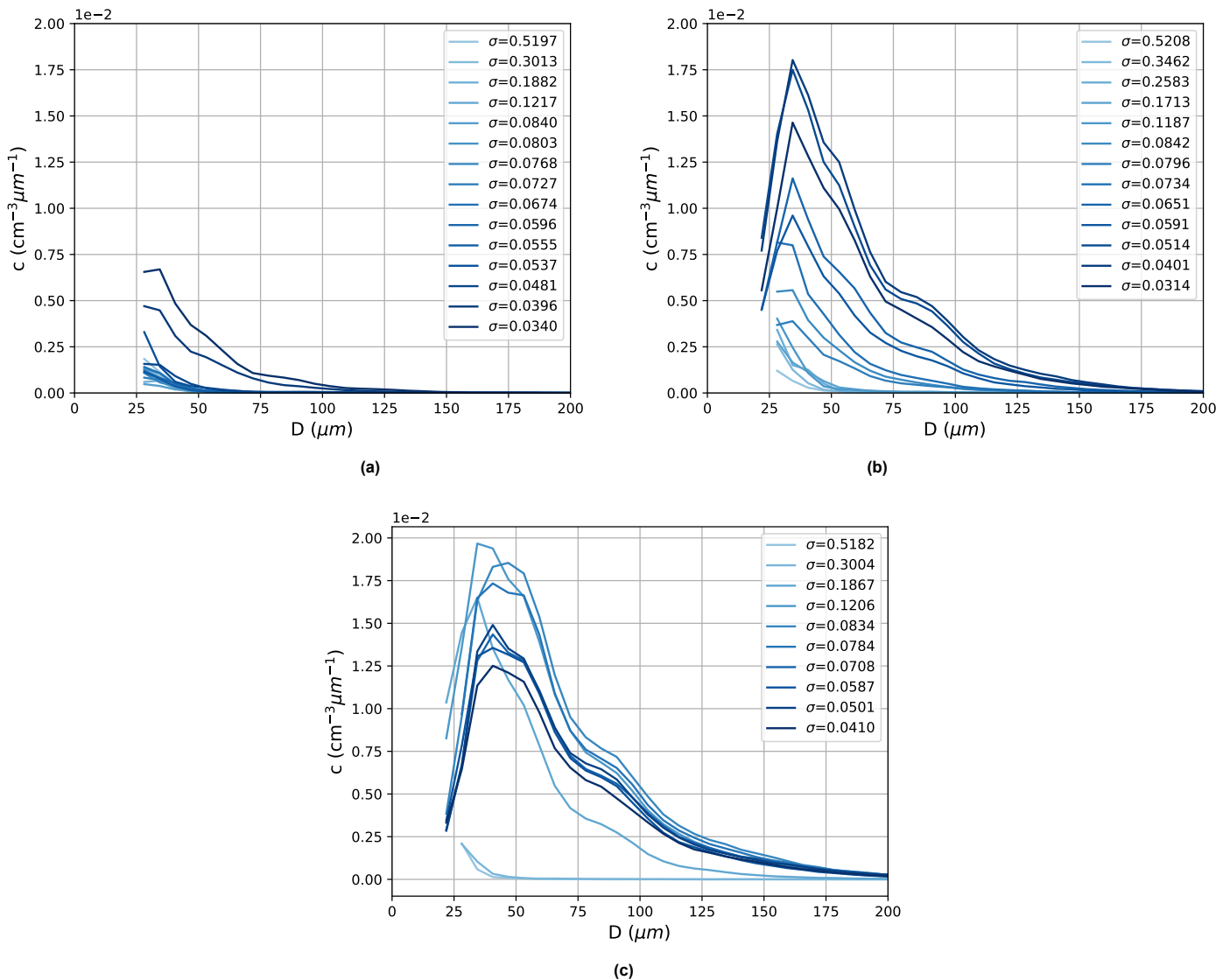


Figure 7.3: Microbubble concentration distribution obtained for different values of σ for the non-critical working point ($n_{ED}=0.2234$, $Q_{ED}=0.2293$, $AOA=20.3^\circ$) at $n=800$ rpm for a) $DO=3.5$ mg/L, b) $DO=5.5$ mg/L, c) $DO=8.5$ mg/L. All curves represent the mean concentration distribution obtained from the Monte Carlo simulation. The uncertainty of these distributions is not shown to enhance visibility.

7.2.2. DO variation at a non-critical working point

To confirm the hypothesis that a cavitating vortex increases the microbubble content in the test rig, additional measurements were performed under the second working point ($n_{ED}=0.2234$, $Q_{ED}=0.1773$, $AOA=15^\circ$) to quantify the microbubble concentration at different runner speeds and DO concentration in the absence of a cavitating vortex. During the measurements, the main focus was to study the effects of the cavitating vortex solely for a runner speed of 800 rpm due to time restrictions. However, the inception point of gap cavitation was determined for each runner's speed and DO concentration. Around the inception point, multiple IPI measurements were conducted to relate the microbubble content to cavitation inception.

To examine the influence of a cavitating vortex on the microbubble content, the content should be compared at both working points of the turbine before σ_i of gap cavitation is reached to avoid the influence of other parameters on the microbubble content measured. Figure 7.4a illustrates the difference in the microbubble concentration distribution for both working points at $\sigma=0.187$, corresponding to the value of σ where a significant increase in microbubble concentration was measured at the critical working point (Figure 7.2a). From Figure 7.4a, it can be concluded that the microbubble concentration is significantly reduced in the absence of a cavitating vortex. Similar to the critical working point, the microbubble concentration increases as the value of σ is lowered (Figure 7.4b). This increase is mostly observed for small microbubbles ($25 \mu\text{m} \leq D \leq 50 \mu\text{m}$). Similar to the critical working point, a reduction in the microbubble content is observed around the cavitation inception point ($\sigma=0.0450$). Although the microbubble concentration shows an increase at lower values of σ , the concentration is significantly lower in the absence of a cavitation vortex (Figure 7.5). Although a cavitating vortex significantly influences the microbubble content, it should be noted that a change in the working point results in a difference in cavitation observed around the runner between the points at identical values of σ .

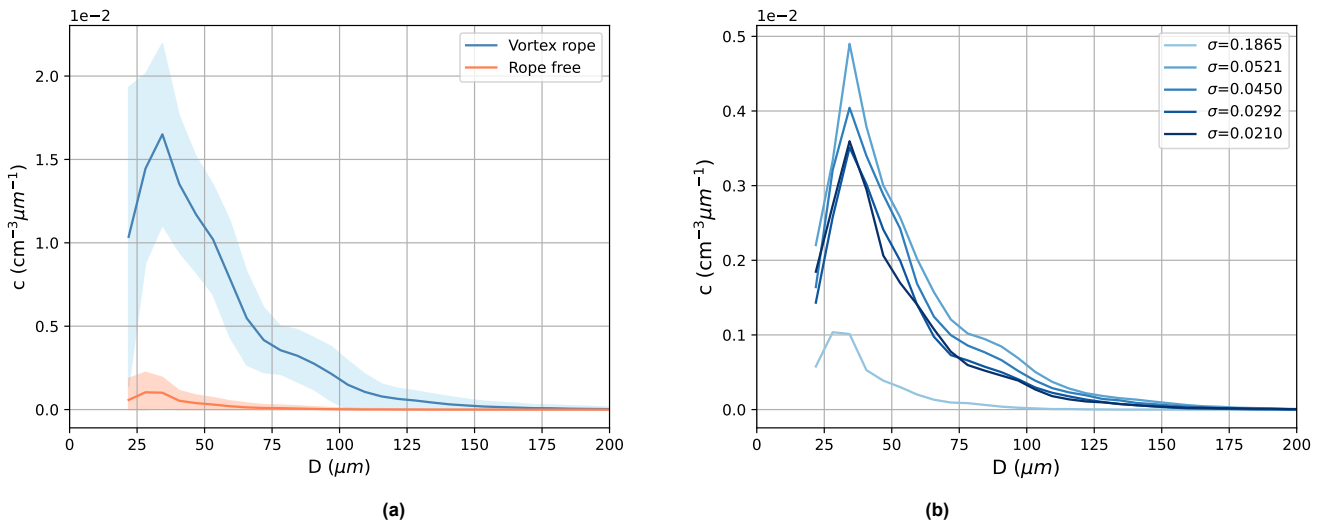


Figure 7.4: Microbubble concentration distribution comparison for a) rope (presence of a cavitating vortex) and rope-free (absence of a cavitating vortex) conditions at $\sigma=0.187$, b) the rope-free (absence of a cavitating vortex) condition for different values of σ . All curves represent the mean concentration distribution obtained from the Monte Carlo simulation. The uncertainty in the concentration distributions is not shown in Figure 7.4b to enhance visibility.

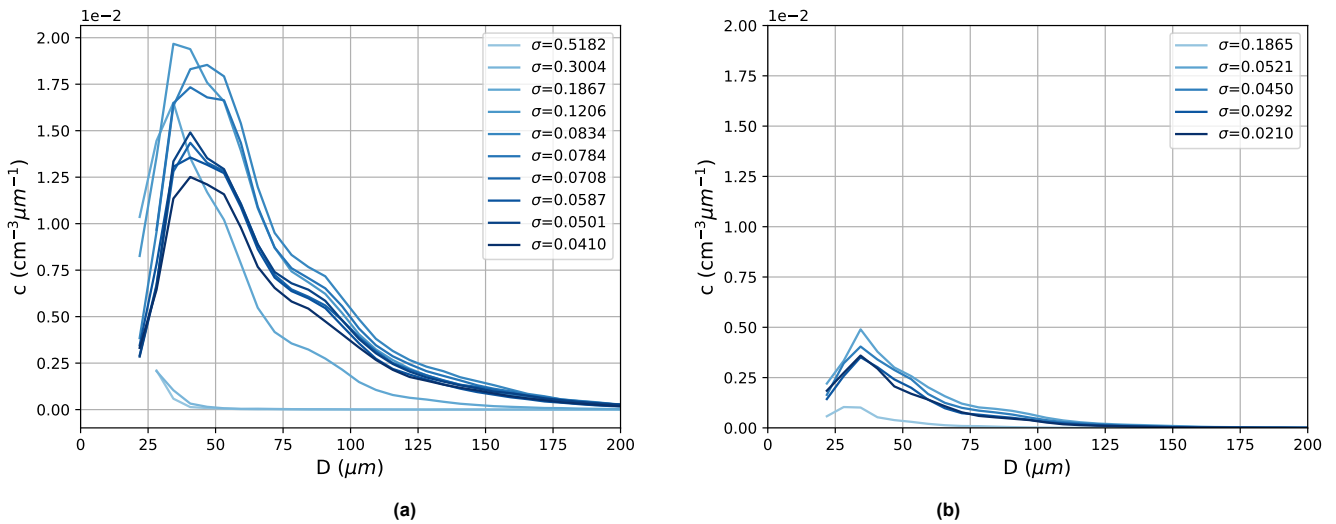


Figure 7.5: Microbubble concentration distribution for a) the critical working point ($n_{ED}=0.2234$, $Q_{ED}=0.2293$, $AOA=20.3^\circ$), i.e., in the presence of a cavitating vortex, b) the non-critical working point ($n_{ED}=0.2234$, $Q_{ED}=0.1773$, $AOA=15^\circ$), i.e., in the absence of a cavitating vortex. The uncertainty in the concentration distributions is not shown to enhance visibility.

7.2.3. Air injection

In the test rig of Andritz Hydro, a sensor is installed to solely measure the DO concentration in the water. Injecting additional air into the system could lead to an increase in the microbubble content without significantly affecting the DO concentration, thereby mimicking possible leakages in the test rig. Air was injected with a volumetric rate of 0.5 and 1.0% of Q_m at different runner speeds, such that the relative flow rate of air is identical at different runner speeds. As a reference, a data point of a sigma break curve at the non-critical working point (absence of a cavitating vortex) at a DO concentration of 3.5 mg/L for each runner speed was chosen.

The average DO concentration measured with the sensor for all cases is listed in Table 7.1, while the microbubble concentration distribution of these measurements is illustrated in Figures 7.6-7.7 for a runner speed of 800 and 1000 rpm, respectively. For both runner speeds but mostly for $n=1000$ rpm, an increase in the concentration of small microbubbles is observed with respect to the reference case. This is because the microbubble concentration measured at $n=1000$ rpm is relatively low compared to $n=800$ rpm, which might be caused by the pressure difference at the measurement position for the two cases. Specifically, the absolute pressure was 4.46 bar at 800 rpm and 6.04 bar at 1000 rpm.

Furthermore, whereas the injections of air were performed in a small time window of approximately an hour, the IPI measurements of the reference cases were not executed consecutively. Instead, the reference case at $n=800$ rpm was measured at the beginning of a working shift, while the reference case at $n=1000$ rpm was measured at the end of the same working shift. A large time window between these measurements could result in a change in the water quality and thus the microbubble content, as will be discussed in Section 7.2.5.

It should be noted that there is an exchange of oxygen between the water and the injected air. It is expected that microbubbles will form from a part of the injected air, while the remainder of air will form a layer above the water or dissolve in the water. Hence, the DO concentration inside the test rig should be affected by the air injection as well. For a runner speed of 1000 rpm, a small increase in the DO concentration is observed, while larger variations are observed at a runner speed of 800 rpm (Table 7.1). The offset in DO concentration at an injection of 0.5% of Q_m at $n=800$ rpm is likely caused by an inaccuracy in the measurements. However, although a lower DO concentration is measured at this point, an increase in the microbubble concentration is observed, showing that external parameters, such as leakages, could influence the microbubble content inside the test rig.

Table 7.1: Average DO concentration measured by the sensor positioned in the test rig for a reference point ($n_{ED}=0.2234$, $Q_{ED}=0.1773$, $AOA=15^\circ$, $DO=3.5$ mg/L) and different volumes of air injections.

Condition	DO concentration (mg/L)	
	n=800 rpm	n=1000 rpm
Reference case	3.78	3.71
Injection: 0.5% of Q_m	3.59	3.84
Injection: 1.0% of Q_m	3.95	3.80

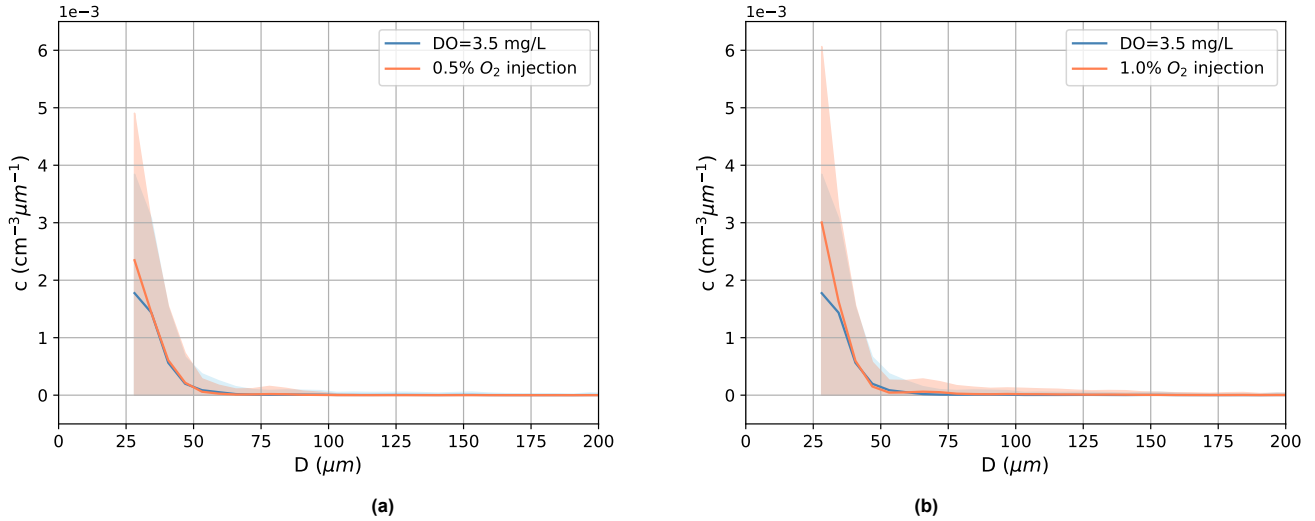


Figure 7.6: Comparison of the microbubble concentration distribution ($n=800$ rpm, $\sigma=0.342$) between an initial DO concentration of 3.5 mg/L and an air injection of a) 0.5% of Q_m , b) 1.0% of Q_m . All measurements were performed at the non-critical working point ($n_{ED}=0.2234$, $Q_{ED}=0.1773$, $AOA=20.3^\circ$). All curves illustrate the mean concentration distribution obtained from the Monte Carlo simulation, while the shaded areas represent 2-std

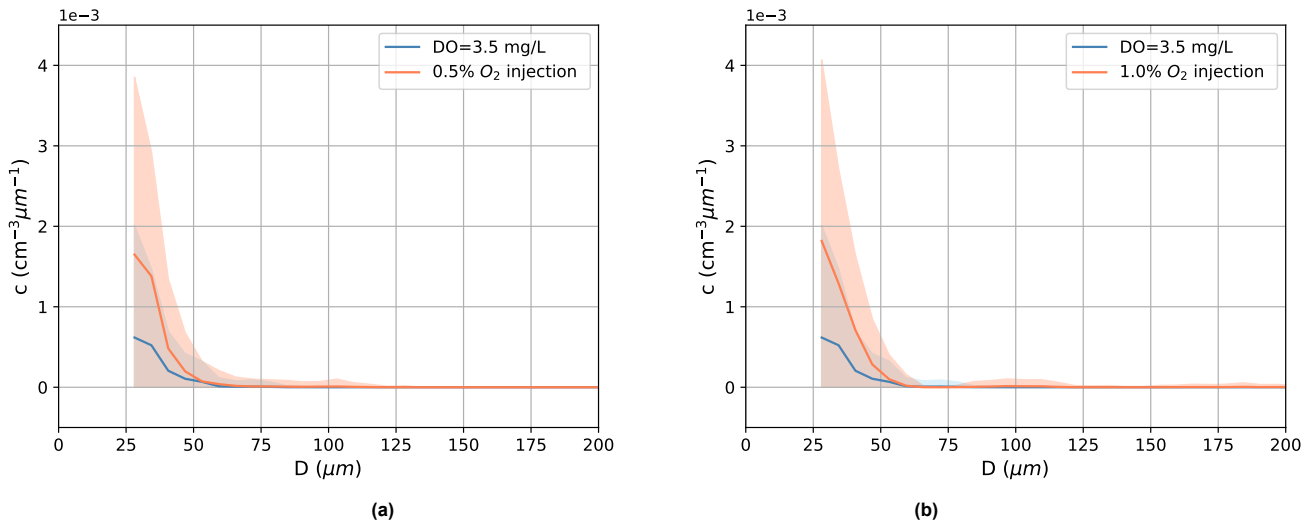


Figure 7.7: Comparison of the microbubble concentration distribution ($n=1000$ rpm, $\sigma=0.220$) between an initial DO concentration of 3.5 mg/L and an air injection of a) 0.5% of Q_m , b) 1.0% of Q_m . All measurements were performed at the non-critical working point ($n_{ED}=0.2234$, $Q_{ED}=0.1773$, $AOA=20.3^\circ$). All curves illustrate the mean concentration distribution obtained from the Monte Carlo simulation, while the shaded areas represent 2-std

7.2.4. Freshwater replacement

For measurement type 4 (Table 5.1), the water in the test rig (storage tank water) was replaced with fresh tap water. Although this tap water originates from the same source as the storage tank water,

there are some differences. First, storage tank water is used for several months without regular refills. During this time, interactions between the water, test rig and environment could affect the quality of the water. Second, the salt NaCl is added to the water for decarbonisation. Lastly, an additive called KW1830 is added to prevent corrosion inside the test rig. This additive consists of phosphoric acids and organic inhibitors that bond to water molecules. This could also affect the water quality. KW1830 also increases the viscosity of the water as it has a dynamic viscosity of 20 mPa·s at a temperature of 20°C, whereas water has a dynamic viscosity of 1.00 mPa·s. Due to the interaction of molecules of the different liquids, the viscosity of a mixture cannot be determined from a weighted average of the liquids [83]. Hence, a water sample of the water inside the test rig containing KW1830 and NaCl was taken to analyse the properties. In contrast to the water inside the test rig, fresh tap water was added without these substances. To compare the water quality, also a sample of the freshwater was taken.

Subsequently, IPI measurements were performed at the non-critical working point ($n_{ED}=0.2234$, $Q_{ED}=0.1773$, $AOA=15^\circ$) for different DO concentrations at $n=800$ rpm. The difference in microbubble concentration for both DO=5.5 and 8.5 mg/L is illustrated in Figure 7.8. For both measurements, a small difference in microbubble concentration is observed between the two types of water. However, due to the large uncertainty, especially at lower concentrations (Figure 7.8a), it is inconclusive whether the replacement of the water inside the test rig affects the microbubble content. It should be noted that there is not a significant difference in the DO concentration between the measurements performed with storage and freshwater, except for the data point at $\sigma \approx 0.025$. From the analysis of the water samples, only a significant difference in the parameters listed in Table 7.2 was found. Although the concentration of calcium and sodium ions significantly differs between the two samples, the order of magnitude of these concentrations does not significantly influence physical parameters, such as the viscosity and surface tension of water. However, it should be noted that these physical parameters were, in the end, not analysed by the lab, and thus, these conclusions are based on the chemical decomposition of the water and the observed microbubble content.

Table 7.2: Comparison of the water quality of storage tank and fresh tap water. The absence of NaCl only results in a reduction of Na, thereby increasing the hardness of the water (Ca).

Parameter	c (mg/L)	
	Storage tank water	Fresh tap water
Ca	22.6	90.7
Na	163	35.4

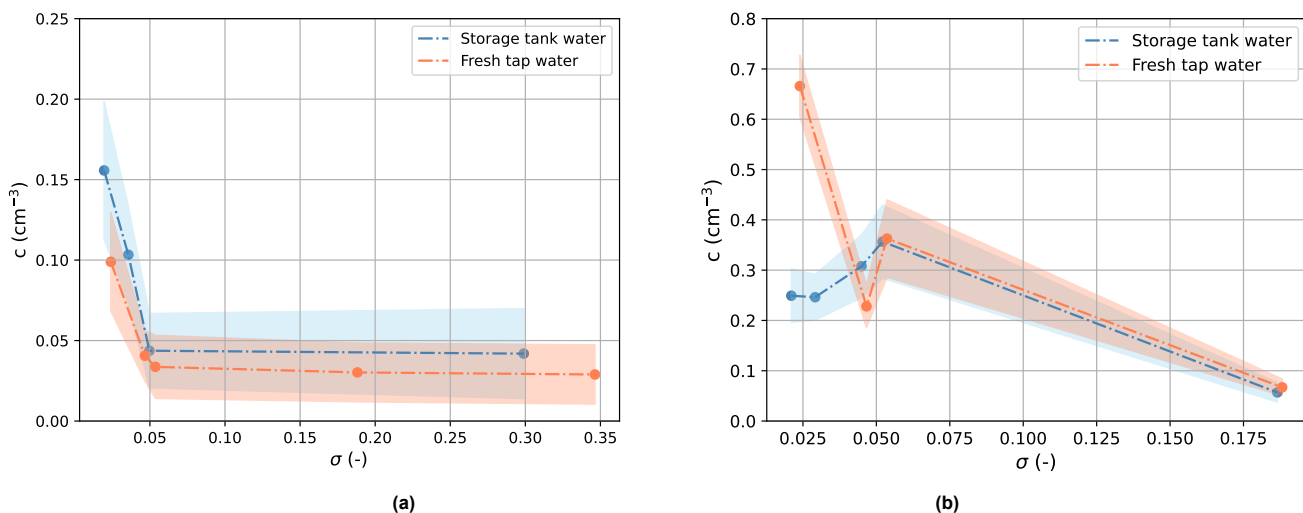


Figure 7.8: Comparison of microbubble concentration between storage tank water and fresh tap water at the non-critical working point ($n_{ED}=0.2234$, $Q_{ED}=0.1773$ and $AOA=15^\circ$) at a) $n=800$ rpm, $\text{DO}= 5.5$ mg/L, b) $n=800$ rpm, $\text{DO}= 8.5$ mg/L

7.2.5. Repeatability of IPI measurements

Microbubbles were measured at different times but under the same test conditions to indicate the repeatability of IPI measurements in a test rig. For these measurements, three data points on a sigma break curve with the following characteristics were chosen: $n_{ED}=0.2234$, $Q_{ED}=0.2293$, $AOA=20.3^\circ$ and $DO=5.5$ mg/L. The microbubble content was measured at $H_s=2.50$ m, 5.50 m and 7.00 m, such that the repeatability of measurements can be determined for different concentrations of microbubbles depending on H_s and thus σ . Measuring the microbubble content at a DO of 8.5 mg/L was not considered, because it is rather difficult to maintain a high DO concentration inside the test rig, which could affect the results. In contrast, repeatability tests at a DO concentration of 3.5 mg/L were not conducted as the microbubble content would be relatively low for each value of H_s .

Figure 7.9 illustrates the difference in the microbubble concentration distribution between the measurements performed at the start and end of a shift for all three data points. For every data point, the trend in the concentration distribution is similar at both times, with a linear decrease over time. A similarity in the distribution is mostly observed when the concentration of microbubbles increases, as shown in Figure 7.9c. For smaller concentrations (Figure 7.9a, 7.9b), the shift in the mean concentration distribution is only visible for a smaller range of microbubble diameters, as these datasets almost only contain small microbubbles.

During this measurement day, measurements were conducted at $DO=5.5$ mg/L at the beginning of the shift, followed by measurements conducted at $DO=3.5$ mg/L at the end of the shift. Thereafter, some of the measurements conducted at $DO=5.5$ mg/L were repeated. All measurements conducted at $DO=5.5$ mg/L were under the critical working point ($n_{ED}=0.2234$, $Q_{ED}=0.1773$ and $AOA=20.3^\circ$) at $n=1200$ rpm. Before the start of the shift, the test rig was degassed by increasing H_s , thereby reducing σ , to reach the desired DO concentration inside the test rig. Hence, by degassing the system, cavitation is observed around the runner. At the end of the shift, pressurised air was added to the system to increase the DO concentration from 3.5 to 5.5 mg/L. Although the DO concentration measured by sensors in the test rig is equivalent at the start and end of a shift, a reduction in the microbubble concentration is observed, indicating that a different parameter influences the microbubble concentration. The hypothesis is that a memory effect affects the microbubble concentration. Due to the memory effects, microbubbles can more easily form at the start of the shift as the DO concentration was high ($DO=9.0$ mg/L) before degassing the test rig. In contrast, microbubbles are less easily formed at the end of the shift as the DO concentration was significantly lower (3.5 mg/L) before conducting the repeated measurements.

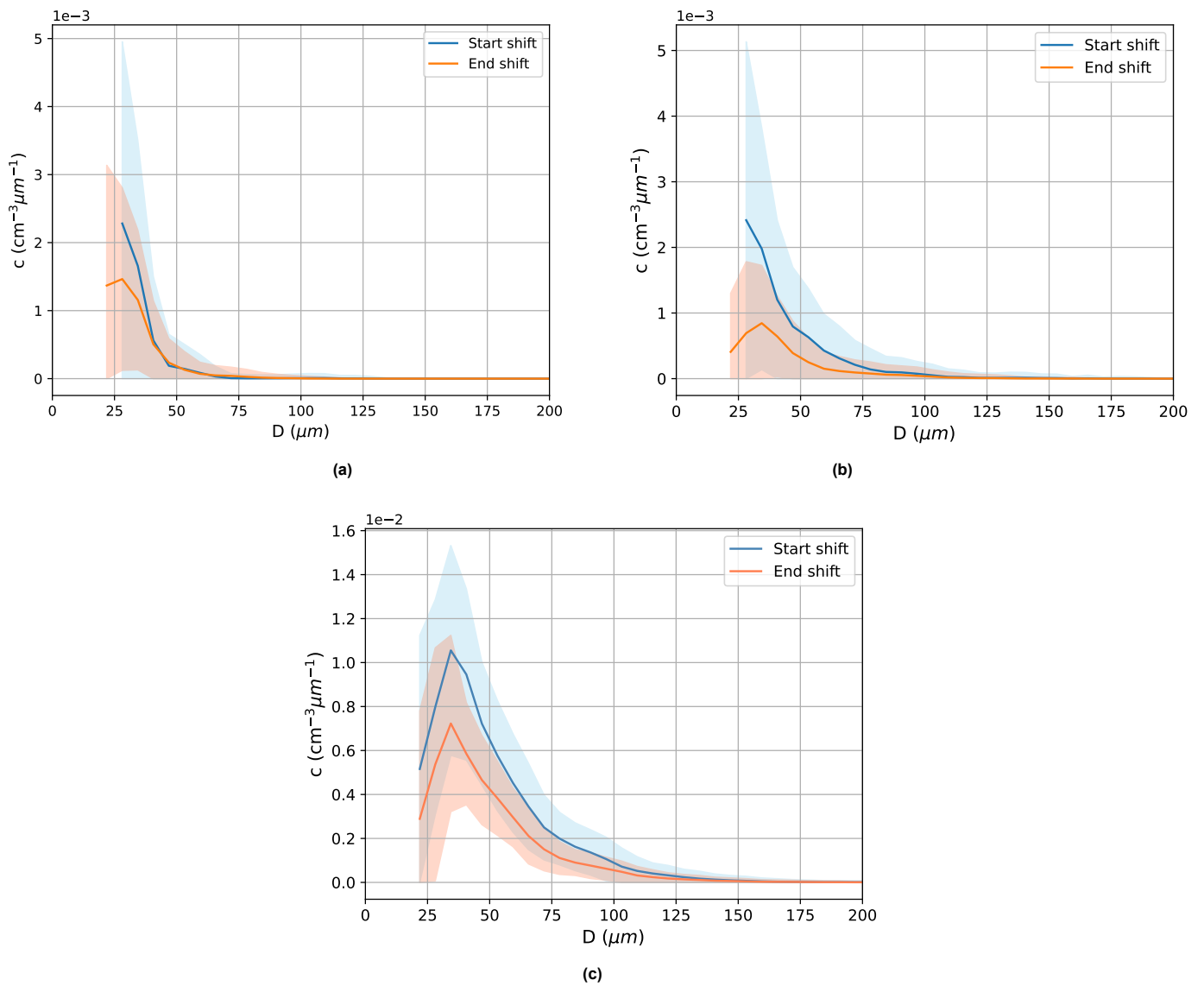


Figure 7.9: Concentration distribution of microbubbles measured at the beginning and end of a working shift under the same conditions ($n_{ED}=0.2234$, $Q_{ED}=0.2293$, $AOA=20.3^\circ$, $DO=5.5$ mg/L) at an H_s of a) 2.50 m, b) 5.50 m and c) 7.00 m. Here, the curves represent the mean concentration of all iterations of the Monte Carlo simulation, while the shaded area represents twice the std. For every value of H_s , a similar distribution of microbubbles is observed between the start and end of a shift, with a decrease in the mean value at the end of a shift. This effect is observed at a larger range of microbubble diameters for increasing H_s .

7.3. Microbubbles and cavitation

In this section, the influence of the microbubble content on cavitation is described. This starts with an overview of the changes in the inception point as a function of the DO concentration in Section 7.3.1. Thereafter, more information regarding the turbine efficiency and the development of different forms of cavitation are highlighted in Sections 7.3.2 and 7.3.3, respectively.

7.3.1. Gap cavitation inception

Although a cavitating vortex appearing at the outlet of the runner is observed at a higher value of σ , compared to other forms of cavitation, this form of cavitation is not considered to be critical for erosion on the runner blades. In contrast, gap cavitation, observed after the onset of a cavitating vortex, is critical for turbines. Hence, the influence of microbubbles on cavitation inception was studied for gap cavitation. For each measurement, the cavitation inception point was determined by observing vapour bubbles appearing at the gap of the runner (Figure 4.13). The cavitation inception point observed at

different runner's speeds and DO concentrations for measurements 1 and 2 (Table 5.1) is illustrated in Table 7.3. In general, at lower runner speeds, the cavitation inception number is lower, as the head of the model is reduced, resulting in lower values of σ (Equation 4.5). Moreover, it can be concluded that for each runner's speed, the cavitation inception number is lower at lower DO concentrations. This illustrates that a lack of microbubbles to act as nuclei for cavitation results in a delay of cavitation observed around a geometry. In contrast, at larger DO concentrations, more and larger microbubbles were measured with IPI. Since larger bubbles have a critical pressure close to the vapour pressure, it is easier for these bubbles to nucleate.

Although the recordings for different runner speeds and DO concentrations were compared to predict the onset of gap cavitation more accurately, human errors remain part of this process. Possible errors are, for instance, shown in measurement 1 at $n = 1200$ rpm and $DO = 3.5$ mg/L, and in measurement 2 at $n = 800$ rpm and $DO = 8.5$ mg/L in Table 7.3. Although σ_i is expected to increase with higher runner speeds at the same DO concentration, these points deviate from this pattern. Apart from these points, the effects of microbubbles seem to decrease slightly with increasing runner speeds. Whether this observation is caused by errors in σ_i or parameters not considered, such as Re , in this study influencing the nucleation rate remains inconclusive. For future research, a parameter study could be performed to determine the influence of other parameters on cavitation inception.

Table 7.3: σ_i of gap cavitation for both considered working points: measurement 1: critical working point ($n_{ED}=0.2234$, $Q_{ED}=0.2293$, $AOA=20.3^\circ$) and measurement 2: non-critical working point ($n_{ED}=0.2234$, $Q_{ED}=0.1773$, $AOA=15^\circ$) for different runner speeds and DO concentrations.

Condition	DO concentration (mg/L)	σ_i (-)		
		n=800 rpm	n=1000 rpm	n=1200 rpm
Measurement 1	3.5	0.0537	0.0610	0.0579
	5.5	0.0591	0.0623	0.0693
	8.5	0.0708	0.0720	0.0729
Measurement 2	3.5	0.0331	0.0353	0.0367
	5.5	0.0356	0.0376	0.0379
	8.5	0.0450	0.0426	0.0430

7.3.2. Turbine efficiency drop

After finding σ_i for each runner's speed and DO concentration, the value of H_s was increased, thereby decreasing σ to determine $\sigma_{\eta,1}$. Here, $\sigma_{\eta,1}$ denotes the cavitation number corresponding to a 1% efficiency drop of the turbine model. For each value of σ , the efficiency of the turbine (η_m) is determined from the average measured torque developed by the runner. As discussed in Section 4.5, the relation between σ and η_m can be illustrated with a sigma break curve. Figure 7.10 illustrates the sigma break curves of the critical working point ($n_{ED}=0.2234$, $Q_{ED}=0.2293$, $AOA=20.3^\circ$) at $n=1200$ rpm for all DO concentrations considered in this study (3.5, 5.5 and 8.5 mg/L). Here, σ_i of gap cavitation for the different DO concentrations is illustrated with the black symbols. The efficiency η_m is normalised by the maximum efficiency of the turbine ($\eta_{m,max}$). As the onset of gap cavitation is observed in an earlier stage at higher DO concentrations due to a larger concentration of microbubbles, the efficiency drop should also be observed in an earlier stage at higher DO concentrations. This also follows from the difference in sigma break curves in the region $0.025 \leq \sigma \leq 0.050$ in Figure 7.10, illustrating a shift in the efficiency drop to the left of the graph for lower DO concentrations.

Since Andritz Hydro observed a difference in $\sigma_{\eta,1}$ at different test locations under the same test conditions (Section 1.1), the effects of the microbubble content on $\sigma_{\eta,1}$ were studied. However, accurately quantifying $\sigma_{\eta,1}$ is complex due to the large fluctuations in η_m measured in the relatively large time window of the IPI measurements compared to the regular time window of the cavitation measurements performed by Andritz Hydro itself. These fluctuations are mostly observed around the initiation of the efficiency drop, as it is challenging to remain at a constant H_s in this region. This is because the vacuum applied to the system in this region is close to the limits of the vacuum pump. thereby causing

fluctuations in H_s . Moreover, other parameters, including the water temperature, influence the efficiency of the model, as the measured torque increases at higher temperatures. Finally, although not frequently observed, there is an offset in the system behind the measurement once the test rig is operating for a long period. Such an offset is shown in Figure 7.10 by the drop in efficiency at $\sigma \approx 0.075$. The combination of these parameters makes it difficult to determine $\sigma_{\eta,1}$ accurately.

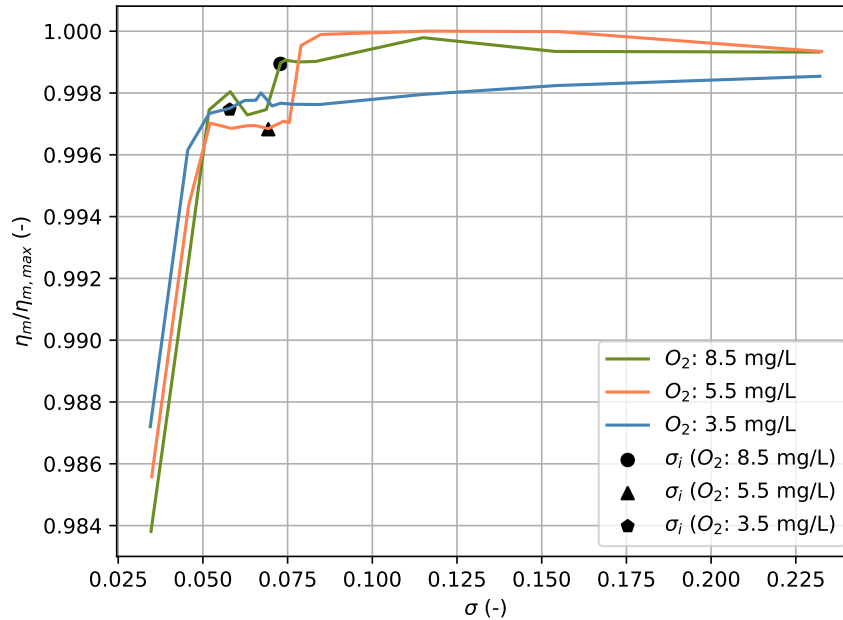


Figure 7.10: Sigma break curves showing the normalised efficiency for different values of σ for different DO concentrations at the critical working point ($n_{ED}=0.2234$, $Q_{ED}=0.2293$, $AOA=20.3^\circ$) at $n=1200$ rpm. σ_i of gap cavitation for each DO concentration is marked with the black symbols.

7.3.3. Cavitation development

In this study, the effects of microbubbles on the dynamics of the different forms of cavitation observed around the runner of the Francis turbine model were analysed using cavitation videos. From these videos, not only a delay in the onset of the different forms of cavitation was observed at low DO concentrations, but also a change in the development of these forms of cavitation compared to higher DO concentrations. The differences in cavitation observed around the runner for a DO concentration of 3.5 and 8.5 mg/L for different values of σ are illustrated in Figure 7.11. The main observations and associated hypotheses are:

- More developed gap cavitation at high DO concentration:** Comparison of Figures 7.11a and 7.11b with Figures 7.11c and 7.11d shows an increase of vapour bubbles at larger DO concentrations. While only separate vapour bubbles are observed at a low DO concentration (Figures 7.11a and 7.11b), both separate vapour bubbles and clusters of vapour bubbles forming sheets around the gap of runner are observed (Figures 7.11c and 7.11d). It is expected that an increase in the DO concentration, which results in a larger concentration of microbubbles, results in a larger vapour volume fraction at the outlet of the labyrinth seal (Section 4.6), resulting in a more continuous supply of cavitation bubbles around the gap of the runner. It should be noted that for each DO concentration gap cavitation changes periodically as the vapour volume fraction at the outlet of the labyrinth seal is not stationary;
- Larger vortex core at high DO concentration:** Comparing Figures 7.11a and 7.11c shows a difference in the width of the cavitating vortex between the two DO concentrations. The core of the cavitating vortex seems to increase with increasing DO concentrations. However, Equation 4.11 implies that the cavitating core of a vortex depends on the pressure of the surrounding liquid, rather than the microbubble content. However, it is possible that the vortex shown in Figures

7.11a and 7.11c, is not fully cavitating but is a mixture of vapour and water [84], [85]. For example, there might be interference between other forms of cavitation, such as surface and gap cavitation, with the cavitating vortex appearing at the interface of the vortex and the surrounding liquid. Since gap cavitation is observed around a larger area of the runner, there might be more interference between cavitation bubbles coming from the gap of the runner compared to low DO concentrations. However, the core of the cavitating vortex changes over time, making it complex to analyse the behaviour from cavitation videos only. Additional measurements, including acoustic measurements or the use of pressure sensors near the labyrinth, could give more insight into the dynamics of the different forms of cavitation and, thereby, the interference between different forms of cavitation. Some of these measurements were also conducted by Brandner *et al.* [53];

- **Higher rotation rate of cavitating vortex at high DO concentration:** Comparing Figures 7.11b and 7.11d shows a difference in the rotation of the cavitating vortex. At a low DO concentration, the cavitating vortex only seems to have a large rotation further away from the outlet of the runner, while at a high DO concentration, a rotation in the cavitating vortex is observed over the entire visible length of the cavitating vortex. Since the dynamics of a cavitating vortex observed in Francis turbines is complex and not yet fully understood, it is complex to determine the role of microbubbles in the observation made. In addition, as the shape of the cavitating vortex changes over time, the behaviour of the cavitating vortex needs to be compared for a larger set of images. However, this makes the analysis more difficult. Hence, the role of microbubbles in the rotation of the cavitation vortex remains inconclusive, and further research into the dynamics of the cavitating vortex and the microbubble content is necessary. The dynamics of the cavitating vortex can be studied using CFD models and experiments. In these experiments, the use of pressure sensors and/or hydrophones can contribute to a better understanding of for example, the pressure fluctuations in the runner or the draft tube. Linking these observations to the cavitation videos could result in a deeper understanding of the dynamics of vortex cavitation in Francis turbines and the role of microbubbles.

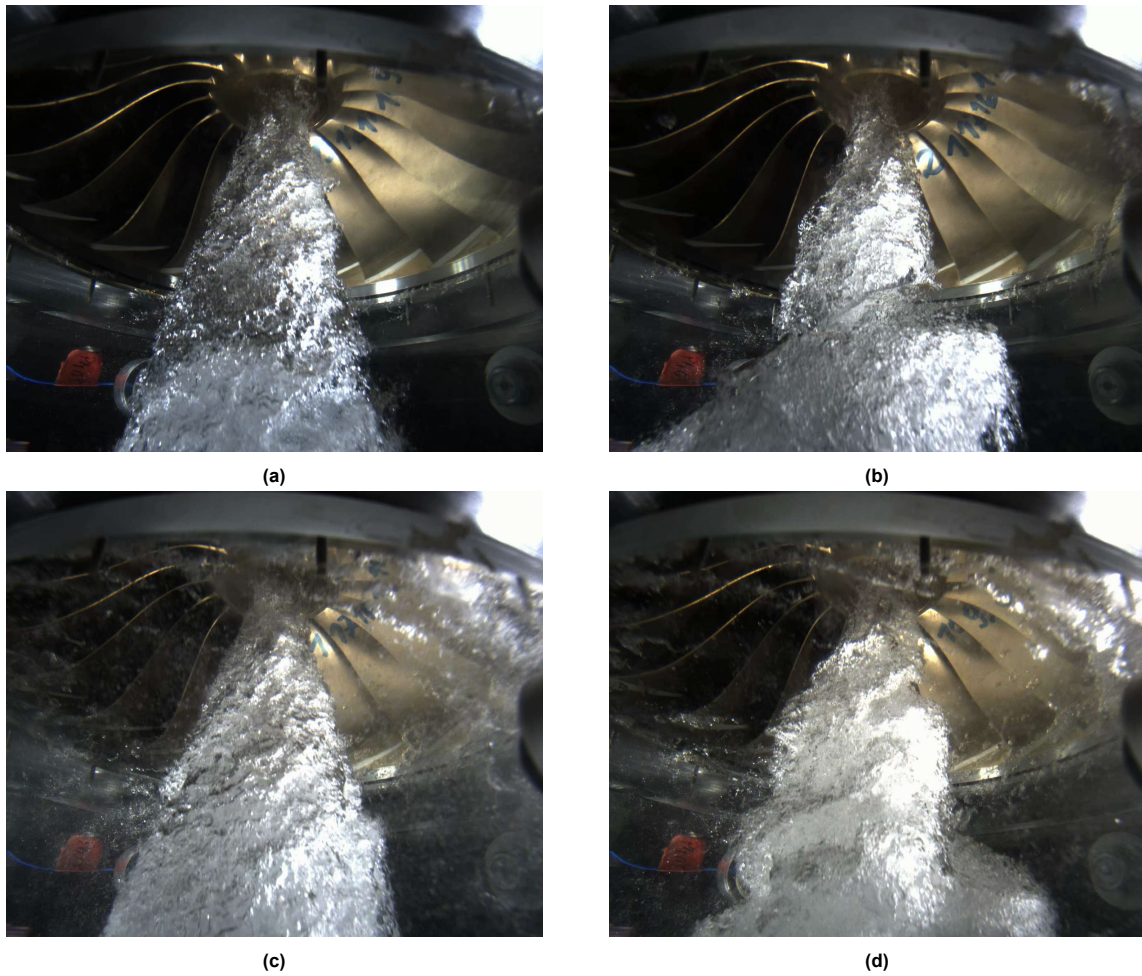
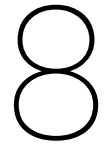


Figure 7.11: Cavitation observed around the runner of a Francis RD-188 Type model at the critical working point ($n_{ED}=0.2234$, $Q_{ED}=0.2293$, $AOA=20.3^\circ$) at a) $\sigma=0.0481$, $DO=3.5$ mg/L, b) $\sigma=0.0396$, $DO=3.5$ mg/L, c) $\sigma=0.0501$, $DO=8.5$ mg/L, d) $\sigma=0.0410$, $DO=8.5$ mg/L



Conclusions

The underlying problem of this study was an offset in σ_i and $\sigma_{\eta,1}$ determined between different test locations under identical test conditions. The hypothesis was that the microbubble content plays a significant role in these differences. Hence, the objective of this study was to identify the effects of the size and concentration of microbubbles on cavitation inception and dynamics. To achieve this, microbubbles were measured in a test facility of Andritz Hydro using the IPI technique, while cavitation was observed around the runner of a hydraulic turbine model (Francis RD-188 Type). The IPI setup was positioned upstream of the model, such that solely remanent microbubbles were measured. The microbubble content in the facility was controlled by regulating the DO concentration. For these measurements, DO concentrations of 3.5, 5.5 and 8.5 mg/L at runner speeds of 800, 1000 and 1200 rpm were used. Under these conditions, sigma break curves were developed by increasing H_s , thereby reducing σ , while measuring the efficiency of the model. At different points of these curves, IPI measurements were performed and cavitation observations were made. In total, five different types of measurements were conducted, including:

- Influence of microbubble content on σ_i of gap cavitation in the presence of a cavitating vortex
- Influence of microbubble content on σ_i of gap cavitation in the absence of a cavitating vortex
- Influence of air injection on microbubble content
- Influence of water replacement on microbubble content
- Repeatability of IPI measurements

While refilling the test facility with fresh tap water does not seem to have a significant influence on the microbubble content, other parameters have shown a significant effect on the content. This includes the DO concentration, σ , and the applied vacuum to the facility.

The measurements show a strong correlation between the DO concentration and the microbubble content, as the size and concentration of microbubbles increase with increasing DO concentration. This increase is also observed in decreasing values of σ as the pressure at the measurement position is reduced. This allows for more and larger microbubbles to become stable. The increase in the microbubble concentration is not only caused by a decrease in pressure but also by the onset of cavitation. The measurements show a significant increase in the microbubble concentration after the appearance of a cavitating vortex at the outlet of the runner. The increase is observed earlier at higher values of DO, as more and larger microbubbles can act as nuclei, thereby reducing the characteristic time scale of a nucleus to be captured by a vortex. Another increase in concentration is observed after the onset of gap cavitation. These results indicate that cavitation bubbles could have been measured. This hypothesis is amplified by the absence of a resorber, allowing bubbles to appear at the measurement position. Although it is not possible to indicate the gas content of the bubbles measured, the vapour inside cavitation bubbles is most likely condensed, leaving small air bubbles at the measurement position. For $\sigma \leq \sigma_i$, a decrease in the microbubble concentration is observed over the entire range of diameters at high DO concentrations, due to a drop in the DO concentration. This is caused by the vacuum applied to the facility at low σ values and the onset of gap cavitation, as oxygen can diffuse into these cavitation bubbles. The drop in the DO concentration is more pronounced at high DO concentrations for two reasons. First of all, deaeration of water only takes place when the water is saturated with air. At high DO concentrations, the saturated oxygen level will be equal or lower than this concentration at a higher pressure compared to low DO concentrations. Secondly, since the microbubble concentrations is strongly related to the DO concentration, more vapour bubbles will be formed at a high DO concentration, thereby reducing the DO concentration faster.

A strong correlation between the microbubble content and cavitation was found. First of all, at lower DO concentrations, σ_i of gap cavitation was found at lower σ values, indicating a delay in the onset. This is caused by a lack of microbubbles in the flow that can act as nuclei to initiate cavitation. The influence of microbubbles on the inception point seems to decrease at higher runner speeds. Further research is necessary to determine whether the uncertainty in determining σ_i or other parameters result in this observation. After the onset of gap cavitation, gap cavitation is more developed at higher DO concentrations, i.e., a larger area of the runner is covered by cavitation bubbles appearing at the gap of the runner. It is expected that the higher concentration of microbubbles causes a larger vapour volume fraction at the outlet of the labyrinth, thereby inducing a more continuous supply of cavitation bubbles

around the gap of the runner. The microbubble content also seems to affect the dynamics of the cavitating vortex appearing at the outlet of the runner, as a larger core and more rotation are observed at high DO concentration. An increase in the cavitating core could result from more interference of other forms of cavitation at the liquid-vapour interface of the cavitating vortex, as other forms of cavitation are more developed at high DO concentrations. However, more research into the dynamics vortex cavitation in Francis turbines is necessary to confirm this. Additionally, this research is necessary to determine the role of microbubbles on the rotation of these vortices, as this remains inconclusive.

9

Recommendations

In this study, a first assessment of the influence of the microbubble content on cavitation around the runner of a hydraulic turbine was made. From this study, the following recommendations for future work are formulated:

- **Improvement of methodology:** Some of the steps performed during the measurement period at Andritz could be improved to reduce the uncertainty in parameters necessary to determine the microbubble concentration distribution and to increase the robustness of the IPI set-up. Here, the parameters referred to are obtained from the camera calibration. After the camera calibration, it was concluded that the grid distortion target plate was slightly rotated, causing a difference in dot size over the width of the plate detected by shadowgraphy. Moreover, the high-speed camera was able to slightly rotate in the xy plane as the mounting between the MicroStage and the aluminium profile was not stiff enough. This means that a small touch led to a shift of the laser as seen on the camera. Furthermore, a shift in the centre of mass of the sheet optic housing leading to vibrations in the laser beam could be mitigated by increasing the robustness of the mounting system;
- **Gaining knowledge on test facility:** During this study, the effects of some parameters, including the DO concentration and the effects of H_s on the microbubble content and cavitation, were determined. However, the microbubble content might be affected by other components of the test facility that were not considered in this study due to the complexity of hydraulic test rigs. For example, leakages in the system and the strength of the pumps could affect the microbubble concentration. A comparison of different test facilities could result in additional factors causing a difference in the microbubble content;
- **Improvement of water samples:** In this study, two water samples were taken from the test rig: one from old storage tank water and one from fresh tap water. An analysis was performed on these samples to indicate their chemical content. Due to the large number of chemicals, it is complex to indicate the difference in physical properties, such as the surface tension and viscosity, between the samples. For further research, an analysis of physical properties would provide a better understanding of the microbubble content. Furthermore, as only two water samples were taken during this study, the effects of physical properties on the microbubble content cannot be fully related. This would for example have been convenient during repeatability measurements. For further research, it is advised to increase the number of water samples during a measurement campaign to study the change in water quality;
- **Improvement on consistency:** Although the influence of different parameters on the microbubble content was studied by changing solely one parameter during each measurement, the complexity of the hydraulic test facility makes it complex to keep several parameters constant, including the DO concentration and H_s . Although these fluctuations are unavoidable, more awareness of these phenomena could have reduced these effects. This is, for example, illustrated in Figure 7.8b by the data point at $\sigma \approx 0.025$ showing a significant increase in the microbubble concentration due to the difference in DO concentration in comparison to the other data points. These effects could have been minimized by increasing the overall measurement procedure such that more time would be available to control these parameters;
- **Improve accuracy of cavitation observations:** Although the effects of the microbubble content on the onset of cavitation around the runner of a turbine can be determined from cavitation observations, there is an uncertainty in σ_i that cannot be quantified. The accuracy of these observations could, for example, be increased by measuring the pressure around the runner with pressure sensors and/or hydrophones, thereby relating pressure fluctuations to cavitation and thus the microbubble content;
- **Inclusion of cavitation dynamics:** In this study, an attempt was made to study the effects of the microbubble content on cavitation dynamics. However, this topic was complex to solve with only the recordings of the runner available. Because the development of cavitation plays a significant role in the determination of $\sigma_{\eta,1}$, a more extensive study on the influence of microbubbles on

the dynamics of cavitation could be performed in the future. The implementation of additional measurements, such as acoustic measurements and the use of pressure sensors, would help in these finding.

References

- [1] F. H. Lafeber *et al.*, “Prediction of underwater radiated noise from propeller cavitation during concept design,” Oct. 2022.
- [2] A. K. Lidtke *et al.*, “Predicting cavitating propeller noise in off-design conditions using scale-resolving CFD simulations,” *Ocean Engineering*, vol. 254, p. 111 176, Jun. 15, 2022, ISSN: 0029-8018. DOI: [10.1016/j.oceaneng.2022.111176](https://doi.org/10.1016/j.oceaneng.2022.111176). [Online]. Available: <https://www.sciencedirect.com/science/article/pii/S0029801822005820> (visited on 01/24/2024).
- [3] S. Gaggero *et al.*, “SHIP URN: UNIGE activities in the context of LIFE-PIAQUO project,” in Aug. 29, 2022, ISBN: 978-1-64368-296-9. DOI: [10.3233/PMST220061](https://doi.org/10.3233/PMST220061).
- [4] International Maritime Organisation, “Noise from commercial shipping and its adverse impacts on marine life,” 2009. [Online]. Available: https://sea-inc.net/wp-content/uploads/2019/10/sn_MEPC_59-19.pdf.
- [5] International Maritime Organisation, “Revised guidelines for the reduction of underwater radiated noise from shipping to address adverse impacts on marine life,” 2023.
- [6] “Introduction the main features of cavitating flows,” in *Fundamentals of Cavitation*, ser. Fluid Mechanics and Its Applications, J.-P. Franc *et al.*, Eds., Dordrecht: Springer Netherlands, 2005, pp. 1–14, ISBN: 978-1-4020-2233-3. DOI: [10.1007/1-4020-2233-6_1](https://doi.org/10.1007/1-4020-2233-6_1). [Online]. Available: https://doi.org/10.1007/1-4020-2233-6_1 (visited on 01/09/2024).
- [7] C. Brennen, “Cavitation and bubble dynamics,” *Cavitation and Bubble Dynamics*, vol. 44, 1995, ISBN: 9781107338760. DOI: [10.1017/CBO9781107338760](https://doi.org/10.1017/CBO9781107338760).
- [8] J.-P. Franc, “The rayleigh-plesset equation: A simple and powerful tool to understand various aspects of cavitation,” in *Fluid Dynamics of Cavitation and Cavitating Turbopumps*, ser. CISM International Centre for Mechanical Sciences, L. d’Agostino *et al.*, Eds., Vienna: Springer, 2007, pp. 1–41, ISBN: 978-3-211-76669-9. DOI: [10.1007/978-3-211-76669-9_1](https://doi.org/10.1007/978-3-211-76669-9_1). [Online]. Available: https://doi.org/10.1007/978-3-211-76669-9_1 (visited on 02/02/2024).
- [9] “The dynamics of spherical bubbles,” in *Fundamentals of Cavitation*, ser. Fluid Mechanics and Its Applications, J.-P. Franc *et al.*, Eds., Dordrecht: Springer Netherlands, 2005, pp. 35–56, ISBN: 978-1-4020-2233-3. DOI: [10.1007/1-4020-2233-6_3](https://doi.org/10.1007/1-4020-2233-6_3). [Online]. Available: https://doi.org/10.1007/1-4020-2233-6_3 (visited on 02/15/2024).
- [10] J.-P. Franc *et al.*, *Fundamentals of Cavitation* (Fluid Mechanics and Its Applications), red. by R. Moreau. Dordrecht: Springer Netherlands, 2005, vol. 76, ISBN: 978-1-4020-2232-6 978-1-4020-2233-3. DOI: [10.1007/1-4020-2233-6](https://doi.org/10.1007/1-4020-2233-6). [Online]. Available: <https://link.springer.com/10.1007/1-4020-2233-6> (visited on 09/28/2024).
- [11] R. E. A. Arndt *et al.*, “Water quality effects on cavitation inception in a trailing vortex,” *Journal of Fluids Engineering*, vol. 114, no. 3, pp. 430–438, 1992, ISSN: 0098-2202. DOI: [10.1115/1.2910049](https://doi.org/10.1115/1.2910049). [Online]. Available: <https://doi.org/10.1115/1.2910049> (visited on 01/30/2024).
- [12] National Oceanic and Atmospheric Administration. “What is water quality?” (), [Online]. Available: <https://floridakeys.noaa.gov/ocean/waterquality.html> (visited on 04/05/2024).
- [13] D. de Zwart, “Monitoring water quality in the future,” no. 3, 1995.
- [14] P. Russell *et al.*, “Influence of nucleation on cavitation inception in tip leakage flows,” *Physics of Fluids*, p. 35, 2023.
- [15] M. Firouzi *et al.*, “A quantitative review of the transition salt concentration for inhibiting bubble coalescence,” *Advances in Colloid and Interface Science*, Reinhard Miller, Honorary Issue, vol. 222, pp. 305–318, Aug. 1, 2015, ISSN: 0001-8686. DOI: [10.1016/j.cis.2014.07.005](https://doi.org/10.1016/j.cis.2014.07.005). [Online]. Available: <https://www.sciencedirect.com/science/article/pii/S0001868614002292> (visited on 03/27/2024).

- [16] N. A. Chang *et al.*, "Tip vortex cavitation suppression by active mass injection," *Journal of Fluids Engineering*, vol. 133, no. 111301, 2011, ISSN: 0098-2202. DOI: [10.1115/1.4005138](https://doi.org/10.1115/1.4005138). [Online]. Available: <https://doi.org/10.1115/1.4005138> (visited on 02/01/2024).
- [17] P. Russell *et al.*, "Calibration of mie scattering imaging for microbubble measurement in hydrodynamic test facilities," *Experiments in Fluids*, vol. 61, no. 4, p. 93, 2020, ISSN: 1432-1114. DOI: [10.1007/s00348-020-2927-7](https://doi.org/10.1007/s00348-020-2927-7). [Online]. Available: <https://doi.org/10.1007/s00348-020-2927-7> (visited on 01/16/2024).
- [18] P. Breeze, "Chapter 4 - hydropower turbines," in *Hydropower*, P. Breeze, Ed., Academic Press, 2018, pp. 35–46, ISBN: 978-0-12-812906-7. DOI: [10.1016/B978-0-12-812906-7.00004-1](https://doi.org/10.1016/B978-0-12-812906-7.00004-1). [Online]. Available: <https://www.sciencedirect.com/science/article/pii/B9780128129067000041> (visited on 04/25/2024).
- [19] M. Birvalski *et al.*, *Developments in microbubble measurement techniques for cavitation and PIV experiments*. 2019.
- [20] A. Karimi *et al.*, "Cavitation erosion of materials," *International Metals Reviews*, vol. 31, no. 1, pp. 1–26, Jan. 1, 1986, Publisher: Taylor & Francis_eprint: <https://doi.org/10.1179/imtr.1986.31.1.1>, ISSN: 0308-4590. DOI: [10.1179/imtr.1986.31.1.1](https://doi.org/10.1179/imtr.1986.31.1.1). [Online]. Available: <https://doi.org/10.1179/imtr.1986.31.1.1> (visited on 01/19/2024).
- [21] M. van Rijsbergen, "A review of sheet cavitation inception mechanisms," in *16th International Symposium on Transport Phenomena and Dynamics of Rotating Machinery*, Honolulu, United States, Apr. 2016. [Online]. Available: <https://hal.science/hal-01890067> (visited on 01/29/2024).
- [22] J. A. Venning *et al.*, "Nucleation effects on cloud cavitation about a hydrofoil," *Journal of Fluid Mechanics*, vol. 947, A1, Sep. 2022, Publisher: Cambridge University Press, ISSN: 0022-1120, 1469-7645. DOI: [10.1017/jfm.2022.535](https://doi.org/10.1017/jfm.2022.535). [Online]. Available: <https://www.cambridge.org/core/journals/journal-of-fluid-mechanics/article/nucleation-effects-on-cloud-cavitation-about-a-hydrofoil/0B4295192E953AD34DDFE74BDBDE2598> (visited on 01/11/2024).
- [23] B. W. McCormick Jr., "On cavitation produced by a vortex trailing from a lifting surface," *Journal of Basic Engineering*, vol. 84, no. 3, pp. 369–378, Sep. 1, 1962, ISSN: 0021-9223. DOI: [10.1115/1.3657328](https://doi.org/10.1115/1.3657328). [Online]. Available: <https://doi.org/10.1115/1.3657328> (visited on 01/26/2024).
- [24] M. van Rijsbergen *et al.*, *High-speed micro-scale observations of nuclei-induced sheet cavitation*. 2011.
- [25] D. H. Fruman *et al.*, "Effect of hydrofoil planform on tip vortex roll-up and cavitation," *Journal of Fluids Engineering*, vol. 117, no. 1, pp. 162–169, Mar. 1, 1995, ISSN: 0098-2202. DOI: [10.1115/1.2816806](https://doi.org/10.1115/1.2816806). [Online]. Available: <https://doi.org/10.1115/1.2816806> (visited on 03/05/2024).
- [26] R. E. A. Arndt *et al.*, "Viscous effects in tip vortex cavitation and nucleation," Accepted: 2009-05-06T15:53:40Z, 1994. [Online]. Available: <http://conservancy.umn.edu/handle/11299/49809> (visited on 03/05/2024).
- [27] B. H. Maines *et al.*, "Tip vortex formation and cavitation," *Journal of Fluids Engineering*, vol. 119, no. 2, pp. 413–419, Jun. 1, 1997, ISSN: 0098-2202. DOI: [10.1115/1.2819149](https://doi.org/10.1115/1.2819149). [Online]. Available: <https://doi.org/10.1115/1.2819149> (visited on 03/04/2024).
- [28] P. K. Kundu *et al.*, "Chapter 4 - conservation laws," in *Fluid Mechanics (Sixth Edition)*, P. K. Kundu *et al.*, Eds., Boston: Academic Press, Jan. 1, 2016, pp. 109–193, ISBN: 978-0-12-405935-1. DOI: [10.1016/B978-0-12-405935-1.00004-6](https://doi.org/10.1016/B978-0-12-405935-1.00004-6). [Online]. Available: <https://www.sciencedirect.com/science/article/pii/B9780124059351000046> (visited on 03/26/2024).
- [29] J. A. Venning *et al.*, "The influence of nuclei content on cloud cavitation about a hydrofoil," in *International Symposium on Transport Phenomena and Dynamics of Rotating Machinery (ISRO-MAC 2017)*, Maui, United States, Dec. 2017. [Online]. Available: <https://hal.science/hal-02342362> (visited on 01/09/2024).
- [30] E. Ebert *et al.*, "Hydrodynamic nuclei concentration technique in cavitation research and comparison to phase-doppler measurements," *Journal of Physics: Conference Series*, vol. 656, no. 1, p. 012 111, 2015, Publisher: IOP Publishing, ISSN: 1742-6596. DOI: [10.1088/1742-6596/656/1/012111](https://doi.org/10.1088/1742-6596/656/1/012111). [Online]. Available: <https://dx.doi.org/10.1088/1742-6596/656/1/012111> (visited on 01/17/2024).

- [31] L. Méès *et al.*, “Development of interferometric techniques for nuclei size measurement in cavitation tunnel,” in *28th Symposium on Naval Hydrodynamics*, Pasadena, United States, Sep. 2010. [Online]. Available: <https://hal.science/hal-02414550> (visited on 01/15/2024).
- [32] E. P. Rood, “Review—mechanisms of cavitation inception,” *Journal of Fluids Engineering*, vol. 113, no. 2, pp. 163–175, Jun. 1, 1991, ISSN: 0098-2202. DOI: [10.1115/1.2909476](https://doi.org/10.1115/1.2909476). [Online]. Available: <https://doi.org/10.1115/1.2909476> (visited on 02/02/2024).
- [33] P. Russell *et al.* “Measurement of nuclei seeding in hydrodynamic test facilities | experiments in fluids.” (2020), [Online]. Available: <https://link.springer.com/article/10.1007/s00348-020-2911-2> (visited on 01/30/2024).
- [34] M. S. Plesset *et al.*, “Bubble dynamics and cavitation,” *Annual Review of Fluid Mechanics*, vol. 9, no. 1, pp. 145–185, 1977. DOI: [10.1146/annurev.fl.09.010177.001045](https://doi.org/10.1146/annurev.fl.09.010177.001045). [Online]. Available: <https://doi.org/10.1146/annurev.fl.09.010177.001045> (visited on 02/09/2024).
- [35] A. Zdziennicka *et al.*, “Components and parameters of liquids and some polymers surface tension at different temperature,” *Colloids and Surfaces A: Physicochemical and Engineering Aspects*, vol. 529, pp. 864–875, Sep. 20, 2017, ISSN: 0927-7757. DOI: [10.1016/j.colsurfa.2017.07.002](https://doi.org/10.1016/j.colsurfa.2017.07.002). [Online]. Available: <https://www.sciencedirect.com/science/article/pii/S0927775717306519> (visited on 02/23/2024).
- [36] D. L. Hartmann, *Global physical climatology* (International geophysics series v. 56). San Diego: Academic Press, 1994, x, 411, ISBN: 978-0-12-328530-0. [Online]. Available: <http://catdir.loc.gov/catdir/toc/els032/93039578.html> (visited on 02/23/2024).
- [37] A. Asnaghi *et al.*, “Analysis of tip vortex inception prediction methods,” *Ocean Engineering*, vol. 167, pp. 187–203, 2018, ISSN: 0029-8018. DOI: [10.1016/j.oceaneng.2018.08.053](https://doi.org/10.1016/j.oceaneng.2018.08.053). [Online]. Available: <https://www.sciencedirect.com/science/article/pii/S0029801818316457> (visited on 01/29/2024).
- [38] J. Choi *et al.*, “Growth, oscillation and collapse of vortex cavitation bubbles,” *Journal of Fluid Mechanics*, vol. 624, pp. 255–279, 2009, Publisher: Cambridge University Press, ISSN: 1469-7645, 0022-1120. DOI: [10.1017/S0022112008005430](https://doi.org/10.1017/S0022112008005430). [Online]. Available: <https://www.cambridge.org/core/journals/journal-of-fluid-mechanics/article/growth-oscillation-and-collapse-of-vortex-cavitation-bubbles/B72017CE90902B59791453E4FD72C9C8> (visited on 01/31/2024).
- [39] M. T. Khoo *et al.*, “Natural nuclei population dynamics in cavitation tunnels,” *Experiments in Fluids*, vol. 61, no. 2, p. 34, Jan. 14, 2020, ISSN: 1432-1114. DOI: [10.1007/s00348-019-2843-x](https://doi.org/10.1007/s00348-019-2843-x). [Online]. Available: <https://doi.org/10.1007/s00348-019-2843-x> (visited on 01/31/2024).
- [40] K. Takahashi *et al.*, “Nuclei population dynamics in NSRC/ATLA flow noise simulator,” Japan, 2019.
- [41] N. A. Chang *et al.*, “Mechanism and scalability of tip vortex cavitation suppression,” 2009.
- [42] J. A. Venning *et al.*, “Background nuclei measurements and implications for cavitation inception in hydrodynamic test facilities,” *Experiments in Fluids*, vol. 59, no. 4, p. 71, Mar. 26, 2018, ISSN: 1432-1114. DOI: [10.1007/s00348-018-2520-5](https://doi.org/10.1007/s00348-018-2520-5). [Online]. Available: <https://doi.org/10.1007/s00348-018-2520-5> (visited on 01/09/2024).
- [43] Y. Mori *et al.*, “Effect of dissolved gas on bubble nucleation,” *International Journal of Heat and Mass Transfer*, vol. 19, no. 10, pp. 1153–1159, Oct. 1, 1976, ISSN: 0017-9310. DOI: [10.1016/0017-9310\(76\)90149-6](https://doi.org/10.1016/0017-9310(76)90149-6). [Online]. Available: <https://www.sciencedirect.com/science/article/pii/0017931076901496> (visited on 02/21/2024).
- [44] S. D. Lubetkin, “Why is it much easier to nucleate gas bubbles than theory predicts?” *Langmuir*, vol. 19, no. 7, pp. 2575–2587, 2003, Publisher: American Chemical Society, ISSN: 0743-7463. DOI: [10.1021/la0266381](https://doi.org/10.1021/la0266381). [Online]. Available: <https://doi.org/10.1021/la0266381> (visited on 02/21/2024).
- [45] X.-x. Peng *et al.*, “Study of tip vortex cavitation inception and vortex singing,” *Journal of Hydrodynamics*, vol. 31, no. 6, pp. 1170–1177, Dec. 1, 2019, ISSN: 1878-0342. DOI: [10.1007/s42241-019-0091-4](https://doi.org/10.1007/s42241-019-0091-4). [Online]. Available: <https://doi.org/10.1007/s42241-019-0091-4> (visited on 02/15/2024).

- [46] S. Laurén. “What are surfactants and how do they work?” (2018), [Online]. Available: <https://www.biolinscientific.com/blog/what-are-surfactants-and-how-do-they-work> (visited on 03/20/2024).
- [47] Y. Nakama, “Chapter 15 - surfactants,” in *Cosmetic Science and Technology*, K. Sakamoto *et al.*, Eds., Amsterdam: Elsevier, Jan. 1, 2017, pp. 231–244, ISBN: 978-0-12-802005-0. DOI: 10.1016/B978-0-12-802005-0.00015-X. [Online]. Available: <https://www.sciencedirect.com/science/article/pii/B978012802005000015X> (visited on 03/20/2024).
- [48] A. S. Pearse *et al.*, “Chapter 7: Salinity,” in *Treatise on Marine Ecology and Paleocology*, J. W. Hedgpeth, Ed., vol. 67V1, Geological Society of America, Dec. 1, 1957, p. 0, ISBN: 978-0-8137-1067-9. DOI: 10.1130/MEM67V1-p129. [Online]. Available: <https://doi.org/10.1130/MEM67V1-p129> (visited on 03/28/2024).
- [49] M. Rosen *et al.* “Surfactants and interfacial phenomena (4th edition).” (2012), [Online]. Available: <https://app-knovel-com.tudelft.idm.oclc.org/kn/resources/kpSIPE0001/toc?cid=kpSIPE0001> (visited on 03/20/2024).
- [50] K. G. Nayar *et al.*, “Surface tension of seawater,” *Journal of Physical and Chemical Reference Data*, vol. 43, no. 4, p. 043 103, Nov. 17, 2014, ISSN: 0047-2689. DOI: 10.1063/1.4899037. [Online]. Available: <https://doi.org/10.1063/1.4899037> (visited on 03/19/2024).
- [51] L. Gemello *et al.*, “Hydrodynamics and bubble size in bubble columns: Effects of contaminants and spargers,” *Chemical Engineering Science*, vol. 184, Mar. 1, 2018. DOI: 10.1016/j.ces.2018.03.043.
- [52] J. Katz, “Cavitation phenomena within regions of flow separation,” *Journal of Fluid Mechanics*, vol. 140, pp. 397–436, Mar. 1984, Publisher: Cambridge University Press, ISSN: 1469-7645, 0022-1120. DOI: 10.1017/S0022112084000665. [Online]. Available: <https://www.cambridge.org/core/journals/journal-of-fluid-mechanics/article/cavitation-phenomena-within-regions-of-flow-separation/D46B26265F84394F2AED7853AFD301FA> (visited on 01/30/2024).
- [53] P. A. Brandner *et al.*, “Nucleation effects on cavitation about a sphere,” *Journal of Fluid Mechanics*, vol. 946, A1, 2022, Publisher: Cambridge University Press, ISSN: 0022-1120, 1469-7645. DOI: 10.1017/jfm.2022.511. [Online]. Available: <https://www.cambridge.org/core/journals/journal-of-fluid-mechanics/article/nucleation-effects-on-cavitation-about-a-sphere/CEE77715DB0CDC3720DDA206837BEFA6> (visited on 01/23/2024).
- [54] M. T. Khoo *et al.*, “Nucleation and cavitation number effects on tip vortex cavitation dynamics and noise,” *Experiments in Fluids*, vol. 62, no. 10, p. 216, Oct. 1, 2021, ISSN: 1432-1114. DOI: 10.1007/s00348-021-03308-2. [Online]. Available: <https://doi.org/10.1007/s00348-021-03308-2> (visited on 01/09/2024).
- [55] H. Ganesh *et al.*, “Bubbly shock propagation as a mechanism for sheet-to-cloud transition of partial cavities,” *Journal of Fluid Mechanics*, vol. 802, pp. 37–78, Sep. 2016, ISSN: 0022-1120, 1469-7645. DOI: 10.1017/jfm.2016.425. [Online]. Available: <https://www.cambridge.org/core/journals/journal-of-fluid-mechanics/article/bubbly-shock-propagation-as-a-mechanism-for-sheettocloud-transition-of-partial-cavities/E59ABEC627ECC82E87753E514B2E17CA#> (visited on 04/02/2024).
- [56] U. U. Gawandalkar *et al.*, “Dynamics of the re-entrant jet in a cavitating venturi,” 2021.
- [57] K. L. d. Graaf *et al.*, “Spectral content of cloud cavitation about a sphere,” *Journal of Fluid Mechanics*, vol. 812, R1, Feb. 2017, ISSN: 0022-1120, 1469-7645. DOI: 10.1017/jfm.2016.819. [Online]. Available: <https://www.cambridge.org/core/journals/journal-of-fluid-mechanics/article/spectral-content-of-cloud-cavitation-about-a-sphere/2134D3B4682F0EFE4FB79E2F7B21011A> (visited on 03/08/2024).
- [58] S. M. Smith *et al.*, “The influence of fluid–structure interaction on cloud cavitation about a flexible hydrofoil. part 2.,” *Journal of Fluid Mechanics*, vol. 897, A28, Aug. 2020, ISSN: 0022-1120, 1469-7645. DOI: 10.1017/jfm.2020.323. [Online]. Available: <https://www.cambridge.org/core/journals/journal-of-fluid-mechanics/article/influence-of-fluidstructure-interaction-on-cloud-cavitation-about-a-flexible-hydrofoil-part-2/2D2E368CBA0BA0340D281C769DEBB8C6> (visited on 04/02/2024).

- [59] D. M. Oldenziel, "A new instrument in cavitation research: The cavitation susceptibility meter," *Journal of Fluids Engineering*, vol. 104, no. 2, pp. 136–141, Jun. 1, 1982, ISSN: 0098-2202. DOI: [10.1115/1.3241790](https://doi.org/10.1115/1.3241790). [Online]. Available: <https://doi.org/10.1115/1.3241790> (visited on 02/06/2024).
- [60] P. A. Naik *et al.*, "Chapter 14 - materials under intense laser irradiation," in *Materials Under Extreme Conditions*, A. K. Tyagi *et al.*, Eds., Amsterdam: Elsevier, Jan. 1, 2017, pp. 501–532, ISBN: 978-0-12-801300-7. DOI: [10.1016/B978-0-12-801300-7.00014-0](https://doi.org/10.1016/B978-0-12-801300-7.00014-0). [Online]. Available: <https://www.sciencedirect.com/science/article/pii/B9780128013007000140> (visited on 04/25/2024).
- [61] N. Fdida *et al.*, "Drop size distribution measured by imaging: Determination of the measurement volume by the calibration of the point spread function," *Measurement Science and Technology*, vol. 21, p. 025501, Dec. 22, 2009. DOI: [10.1088/0957-0233/21/2/025501](https://doi.org/10.1088/0957-0233/21/2/025501).
- [62] G. S. Settles, *Schlieren and shadowgraph techniques: visualizing phenomena in transparent media* (Experimental fluid mechanics). Berlin: Springer, 2001, xviii, 376, Section: xviii, 376 pages : illustrations (some color) ; 24 cm., ISBN: 978-3-540-66155-9.
- [63] Y. Niwa *et al.*, "Bubble sizing by interferometric laser imaging," 2000. [Online]. Available: <https://www.semanticscholar.org/paper/Bubble-Sizing-by-Interferometric-Laser-Imaging-Niwa-Kamiya/cb1e8fa0ed33ede832eac7dc450747f124f1082d> (visited on 01/15/2024).
- [64] H. C. v. d. Hulst *et al.*, "Glare points," *Applied Optics*, vol. 30, no. 33, pp. 4755–4763, Nov. 20, 1991, Publisher: Optica Publishing Group, ISSN: 2155-3165. DOI: [10.1364/AO.30.004755](https://doi.org/10.1364/AO.30.004755). [Online]. Available: <https://opg.optica.org/ao/abstract.cfm?uri=ao-30-33-4755> (visited on 02/12/2024).
- [65] H. C. v. d. Hulst, *Light Scattering by Small Particles*. Courier Corporation, Jan. 1, 1981, 502 pp., Google-Books-ID: PIHfPMVAFRcC, ISBN: 978-0-486-64228-4.
- [66] R. Boucheron *et al.*, "Comparative study of optical experimental methods for micro-bubble sizing," 2018.
- [67] R. Stigter *et al.*, "An improved calibration methodology and uncertainty assessment in measurements of microbubble size and concentration," Delft, 2024.
- [68] A. M. Kabe *et al.*, "Chapter 5 - analysis of continuous and discrete time signals," in *Structural Dynamics Fundamentals and Advanced Applications*, A. M. Kabe *et al.*, Eds., Academic Press, Jan. 1, 2020, pp. 271–427, ISBN: 978-0-12-821615-6. DOI: [10.1016/B978-0-12-821615-6.00005-8](https://doi.org/10.1016/B978-0-12-821615-6.00005-8). [Online]. Available: <https://www.sciencedirect.com/science/article/pii/B9780128216156000058> (visited on 03/14/2024).
- [69] T. Kawaguchi *et al.*, "Size measurements of droplets and bubbles by advanced interferometric laser imaging technique," *Measurement Science and Technology*, vol. 13, no. 3, p. 308, Feb. 2002, ISSN: 0957-0233. DOI: [10.1088/0957-0233/13/3/312](https://doi.org/10.1088/0957-0233/13/3/312). [Online]. Available: <https://dx.doi.org/10.1088/0957-0233/13/3/312> (visited on 01/17/2024).
- [70] R. O. Duda *et al.*, "Use of the hough transformation to detect lines and curves in pictures," *Communications of the ACM*, vol. 15, no. 1, pp. 11–15, 1972, ISSN: 0001-0782, 1557-7317. DOI: [10.1145/361237.361242](https://doi.org/10.1145/361237.361242). [Online]. Available: <https://dl.acm.org/doi/10.1145/361237.361242> (visited on 05/13/2024).
- [71] S. Brahmhatt, *Practical OpenCV*. Berkeley, CA: Apress, 2013, ISBN: 978-1-4302-6079-0 978-1-4302-6080-6. DOI: [10.1007/978-1-4302-6080-6](https://doi.org/10.1007/978-1-4302-6080-6). [Online]. Available: <http://link.springer.com/10.1007/978-1-4302-6080-6> (visited on 05/13/2024).
- [72] K. Ibrahim *et al.*, "Signal processing considerations for low signal to noise ratio laser doppler and phase doppler signals," 1991.
- [73] K. A. Shinpaugh *et al.*, "Signal-processing techniques for low signal-to-noise ratio laser doppler velocimetry signals," *Experiments in Fluids*, vol. 12, no. 4, pp. 319–328, Mar. 1, 1992, ISSN: 1432-1114. DOI: [10.1007/BF00187310](https://doi.org/10.1007/BF00187310). [Online]. Available: <https://doi.org/10.1007/BF00187310> (visited on 03/18/2024).

- [74] International Electrotechnical Commission. "IEC 60193:2019 - hydraulic turbines, storage pumps and pump-turbines - model acceptance tests," iTeh Standards. (2019), [Online]. Available: <https://standards.iteh.ai/catalog/standards/iec/e473e535-bcfb-45dc-8b0b-3e60bc13d4c4/iec-60193-2019> (visited on 06/20/2024).
- [75] ASME Hydro Power Technical Committee, *The Guide to Hydropower Mechanical Design*. Kansas City MO: HCI Publications, 1996, 1 p., OCLC: 874436978, ISBN: 978-0-9651765-0-7.
- [76] C. Nicolet, "Hydroacoustic modelling and numerical simulation of unsteady operation of hydroelectric systems," Ph.D. dissertation, EPFL, Lausanne, 2007, 334 pp. DOI: [10.5075/epfl-thesis-3751](https://doi.org/10.5075/epfl-thesis-3751).
- [77] K. Celebioglu *et al.*, "Numerical research of cavitation on francis turbine runners," *International Journal of Hydrogen Energy*, Special Issue on The 4th European Conference on Renewable Energy Systems (ECRES 2016), 28-31 August 2016, Istanbul, Turkey, vol. 42, no. 28, pp. 17771–17781, Jul. 13, 2017, ISSN: 0360-3199. DOI: [10.1016/j.ijhydene.2017.03.180](https://doi.org/10.1016/j.ijhydene.2017.03.180). [Online]. Available: <https://www.sciencedirect.com/science/article/pii/S0360319917312259> (visited on 10/11/2024).
- [78] S. Stalikas *et al.*, "Labyrinth-induced gap cavitation in high head francis turbines: CFD analysis and experimental observations," 2024.
- [79] A. P. Pentland, "A new sense for depth of field," *IEEE Transactions on Pattern Analysis and Machine Intelligence*, vol. PAMI-9, no. 4, pp. 523–531, Jul. 1987, Conference Name: IEEE Transactions on Pattern Analysis and Machine Intelligence, ISSN: 1939-3539. DOI: [10.1109/TPAMI.1987.4767940](https://doi.org/10.1109/TPAMI.1987.4767940). [Online]. Available: <https://ieeexplore.ieee.org/document/4767940> (visited on 09/03/2024).
- [80] LaVision GmbH. "LaVision - sheet optics." (), [Online]. Available: <https://www.digitalimagecorrelation.com/en/products/flowmaster/piv-system-components/light-sheet-optics/> (visited on 10/18/2024).
- [81] M. Birvalski *et al.*, *Application of Interferometric Particle Imaging to cavitation nuclei measurements in a ship model basin*. Jul. 16, 2018.
- [82] Y. Wei *et al.*, "Mechanisms of the memory effect of clathrate hydrates," *Chemical Engineering Science*, vol. 270, p. 118538, Apr. 15, 2023, ISSN: 0009-2509. DOI: [10.1016/j.ces.2023.118538](https://doi.org/10.1016/j.ces.2023.118538). [Online]. Available: <https://www.sciencedirect.com/science/article/pii/S0009250923000945> (visited on 10/22/2024).
- [83] R. A. McAllister, "The viscosity of liquid mixtures," *AIChE Journal*, vol. 6, no. 3, pp. 427–431, 1960, eprint: <https://onlinelibrary.wiley.com/doi/pdf/10.1002/aic.690060316>, ISSN: 1547-5905. DOI: [10.1002/aic.690060316](https://doi.org/10.1002/aic.690060316). [Online]. Available: <https://onlinelibrary.wiley.com/doi/abs/10.1002/aic.690060316> (visited on 10/02/2024).
- [84] W. Cornel, "Shock waves in two-phase bubbly liquids," Ph.D. dissertation, Delft University of Technology, 2024. DOI: [10.4233/UUID:0384A3C9-EAF1-4FB8-A67A-93920DA3F0DF](https://doi.org/10.4233/UUID:0384A3C9-EAF1-4FB8-A67A-93920DA3F0DF). [Online]. Available: <https://resolver.tudelft.nl/uuid:0384a3c9-eaf1-4fb8-a67a-93920da3f0df>.
- [85] U. U. Gawandalkar *et al.*, *Examination of ventilated cavities in the wake of a two-dimensional bluff body*, Aug. 4, 2024. arXiv: [2408.02026](https://arxiv.org/abs/2408.02026). [Online]. Available: <http://arxiv.org/abs/2408.02026>.
- [86] E. B. Corrochano, *Handbook of Geometric Computing: Applications in Pattern Recognition, Computer Vision, Neural Computing, and Robotics*. Berlin, Heidelberg: Springer, 2005, ISBN: 978-3-540-20595-1 978-3-540-28247-1. DOI: [10.1007/3-540-28247-5](https://doi.org/10.1007/3-540-28247-5). [Online]. Available: <https://link.springer.com/10.1007/3-540-28247-5> (visited on 05/10/2024).
- [87] D. Lyon, "The discrete fourier transform, part 4: Spectral leakage.," *The Journal of Object Technology*, vol. 8, no. 7, p. 23, 2009, ISSN: 1660-1769. DOI: [10.5381/jot.2009.8.7.c2](https://doi.org/10.5381/jot.2009.8.7.c2). [Online]. Available: http://www.jot.fm/contents/issue_2009_11/column2.html (visited on 05/12/2024).
- [88] A. Breitenbach, "Against spectral leakage," *Measurement*, vol. 25, no. 2, pp. 135–142, 1999, ISSN: 0263-2241. DOI: [10.1016/S0263-2241\(98\)00074-8](https://doi.org/10.1016/S0263-2241(98)00074-8). [Online]. Available: <https://www.sciencedirect.com/science/article/pii/S0263224198000748> (visited on 05/12/2024).

- [89] A. Brandt, *Noise and Vibration Analysis: Signal Analysis and Experimental Procedures*, 1st ed. Wiley, 2011, ISBN: 978-0-470-74644-8 978-0-470-97816-0. DOI: [10.1002/9780470978160](https://doi.org/10.1002/9780470978160). [Online]. Available: <https://onlinelibrary.wiley.com/doi/book/10.1002/9780470978160> (visited on 03/14/2024).
- [90] R. J. Beerends *et al.*, *Fourier and Laplace Transforms*. Cambridge: Cambridge University Press, 2003, ISBN: 978-0-521-80689-3. DOI: [10.1017/CB09780511806834](https://doi.org/10.1017/CB09780511806834). [Online]. Available: <https://www.cambridge.org/core/books/fourier-and-laplace-transforms/OF9A50F9BC601A58ADF6A77FA0C8FED3> (visited on 03/02/2024).
- [91] E. O. Brigham, *The fast Fourier transform and its applications* (Prentice Hall signal processing series). Englewood Cliffs, N.J: Prentice-Hall, 1988, 448 pp., ISBN: 978-0-13-307505-2 978-0-13-307547-2.

A

Background information

In this appendix, a detailed description of the different concepts used in the IPI image processing is given. This starts with a description of the application of the different filters in Section A.1, followed by a general description of the Hough Gradient method and Fourier Transform in Sections A.2 and A.3, respectively.

A.1. Filters

Filters are often used to manipulate signals, thereby making post-processing more effective. To process the IPI images two filters are used: a kernel and 2D Hann filter.

Image operations, including blurring or sharpening of images and edge detection, can be performed using the convolution of a kernel filter and an image [86]. An example image to illustrate the application of a kernel filter is shown in Figure A.1. The original image is an 8-bit image described by a 4x4 matrix showing different grey values. These values are characterised by $2^{N_{bits}}$, where 0 corresponds to a black px, whereas 255 corresponds to a white px. The convolution of the kernel matrix and the original image is determined for each part of the image as the kernel matrix shifts along the image. Figure A.1 illustrates two of these operations and their outputs. Although the weights of the kernel filter in Figure A.1 are arbitrarily chosen, these are important to describe the influence of neighbouring px and thus affect the appearance of the output image. Depending on these weights, it is possible to sharpen or blur an image. Figure A.2 illustrates some of these possibilities. Here, Figure A.2a is an example image, while Figures A.2b-A.2d show the convolution of a 3x3 kernel filter and Figure A.2a, resulting in more sharpness, a box blur and a gaussian blur, respectively. Additionally, the size of the kernel matrix affects the convolution, as a larger kernel matrix involves more neighbouring px, thereby reducing the number of details in the output image.

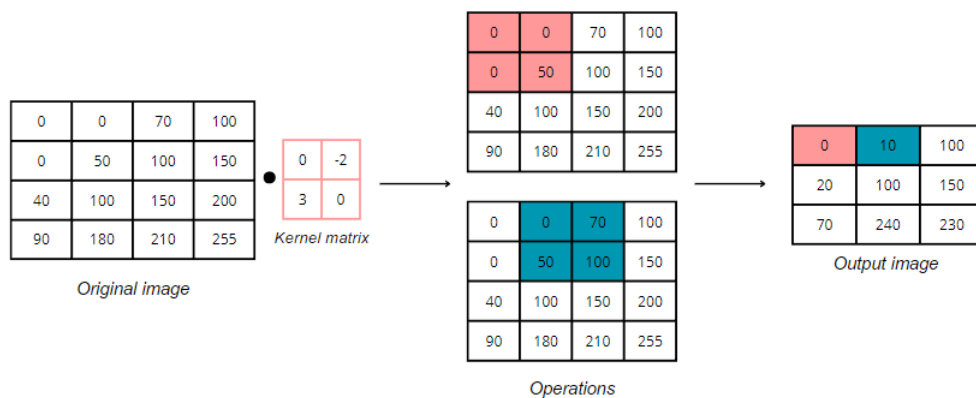


Figure A.1: Application of a kernel filter to a greyscale image. The cover of the kernel filter on the original image is here limited to 2 locations.

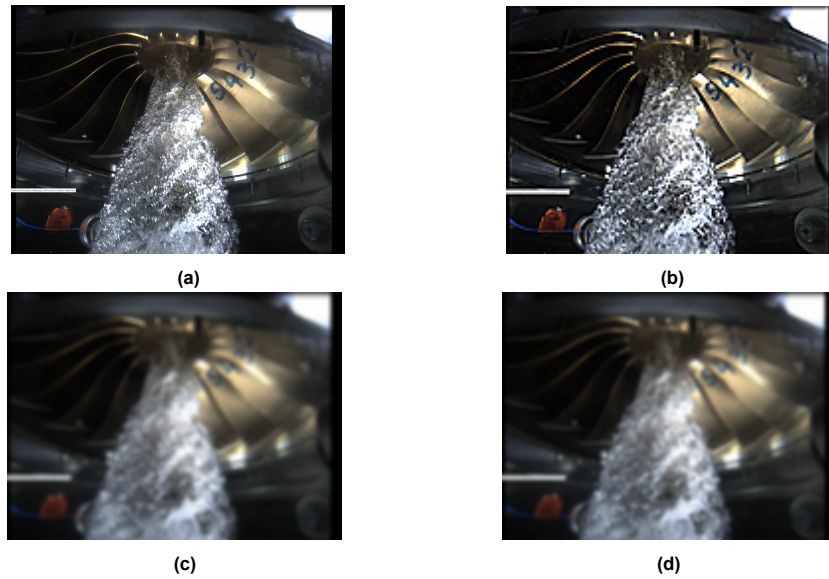


Figure A.2: a) Original image. The convolution of the original image and the 3x3 kernel filter is used to b) sharpen the image, c) blur the image with a box blur and c) blur the image with a Gaussian blur.

Additionally, a 2D Hann filter is used in this study. This filter is commonly used to reduce the amount of spectral leakage, for example, when applying an FT [87], [88]. This is illustrated with Figure A.3a for 1D, showing a sample of a cosine function indicated by the blue curve. If a non-integer number of periods of a function is sampled multiple times, a discontinuity in the signal appears, indicated at the red dotted line (Figure A.3a). This discontinuity will cause spectral leakage in the FT, meaning that a range of frequencies around the frequency of the signal is found by the FT (Figure A.3b). To reduce the amount of spectral leakage, a Hann filter can be multiplied with the function. This filter uses a weighted cosine [89]:

$$w_H(n) = 0.5 \cdot \left(1 - \cos\left(\frac{2\pi n}{N-1}\right) \right) \quad \text{for } 0 \leq n \leq N-1 \quad (\text{A.1})$$

where N is the total amount of samples. Multiplication of Equation A.1 with the original cosine function results in a new sample free of discontinuities, indicated by the yellow curve in Figure A.3a. The FT of this new function results in a smaller spread of frequencies detected by the FT (Figure A.3b).

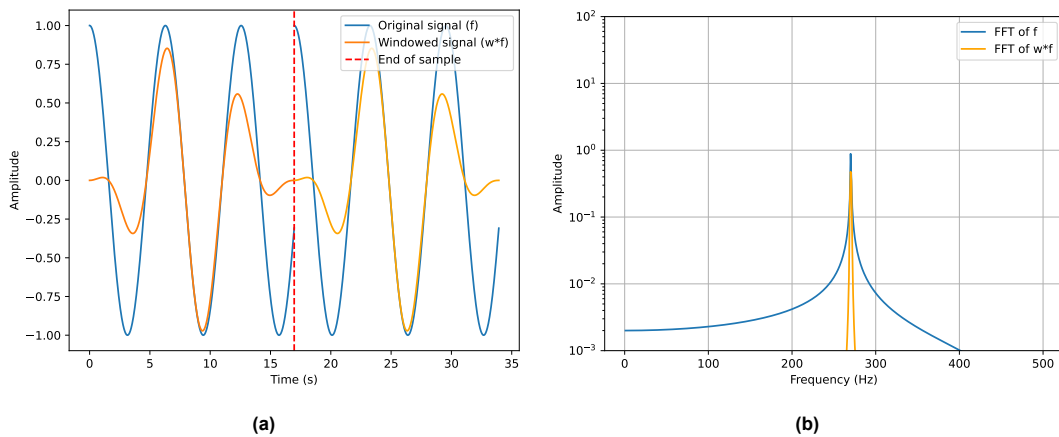


Figure A.3: a) Two samples of a cosine function f with $\omega=1.0$ rad/s, and the multiplication of the Hann window w with f , indicated by the blue and orange curves, respectively. The red line indicates the time corresponding to the end of the first sample. b) Outcome of the FFT of the original function f and windowed function $w \cdot f$, indicated by the blue and orange lines, respectively. The amount of spectral leakage is significantly reduced by applying the Hann window.

A.2. Hough transform

Microbubbles, represented as circular disks in the IPI images, can be detected with the Hough Gradient method. This method was originally developed for line detection by introducing the parameters ρ and θ [70], the perpendicular distance between the origin and a line and the angle between the perpendicular line and the x-axis (Figure A.4a), respectively. Here, the latter is within the interval $[0, \pi]$. With these parameters, it is possible to describe every line in the image space (xy system) as:

$$x \cos(\theta) + y \sin(\theta) = \rho \quad (\text{A.2})$$

For known values of ρ and θ , it is possible to determine every point on the line. However, if these parameters are unknown, while the (x,y) coordinates of certain points are known, it is possible to determine ρ and θ by rewriting Equation A.2 as:

$$\rho = x_i \cos(\theta) + y_i \sin(\theta) \quad (\text{A.3})$$

Using Equation A.3, the known points (x_i, y_i) can be mapped from the image space to the parameter space (Figure A.4b), where the axes represent ρ and θ . In the parameter space, every point can be written as a summation of cosine and sine waves. The intersection of these waves of different points corresponds to the values of ρ and θ describing the line in Figure A.4a. A general approach is to develop an accumulator matrix where the rows and columns represent ρ and θ , respectively. For each combination of ρ and θ the number of intersecting waves can be written down in this matrix. The maximum in this matrix will present the values of ρ and θ of the corresponding line.

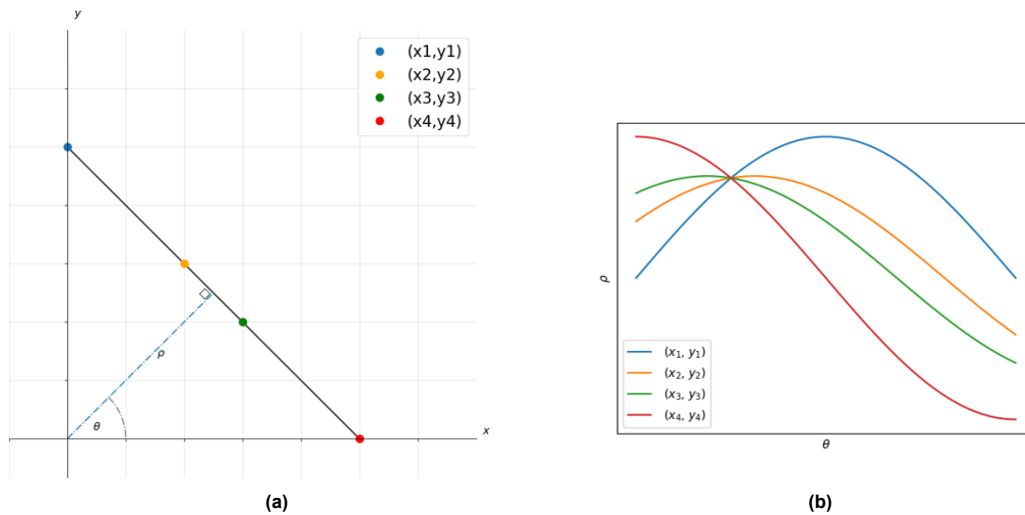


Figure A.4: a) Characterisation of a line in the image space by the parameters ρ and θ . A set of 4 different points on the line are shown. b) Parameter space representing the data points on the line in the image space.

The principles of the Hough Gradient method also apply to circle detection using the equation of a circle:

$$(x - a)^2 + (y - b)^2 = r^2 \quad (\text{A.4})$$

where a , b and r represent the x and y coordinates of a circle's centre and the circle's radius, respectively. Similar to line detection, for known points on a circle, Equation A.4 can be rewritten as:

$$a = r - x_i \cdot \cos(\theta) \quad (\text{A.5})$$

$$b = r - y_i \cdot \sin(\theta) \quad (\text{A.6})$$

If the radius of a circle is known, different points on a circle in the image space (Figure A.5a) can be mapped into the parameter space (Figure A.5b), where each point is represented by a circle. The intersection of these circles indicates the values of a and b of the original circle shown in Figure A.5a. However, if the radius of a circle is unknown, a point (x_i, y_i) on a circle in the image space cannot be

represented by a single circle in the parameter space. Instead, for every value of r , a point can be described by a different circle in the parameter space, resulting in a cone (Figure A.6). Similar to line detection, the parameters a , b and r of a circle can be found using an accumulator matrix. However, an additional dimension is added to this matrix representing r .

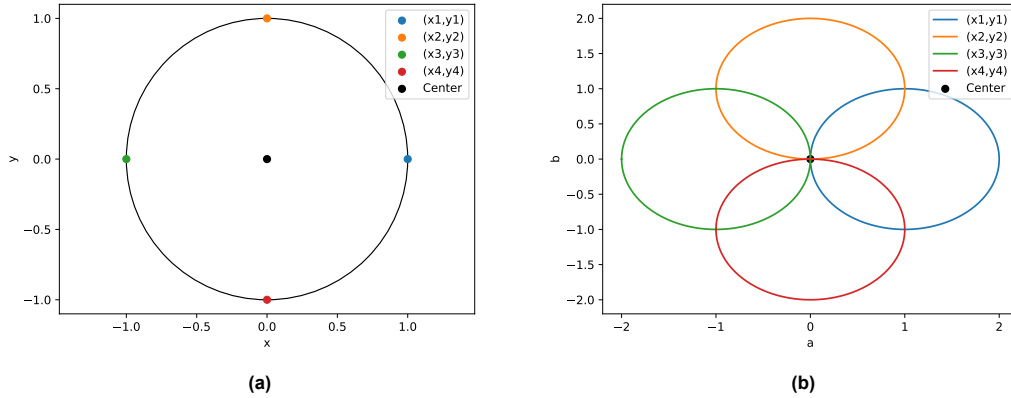


Figure A.5: Different points (x_i, y_i) on a circle with radius 1 and centre $(0,0)$ shown in the a) image space and b) parameter space. In the parameter space, the points (x_i, y_i) are represented by a circle. The intersection of these circles represents the centre of the circle that is shown in the image space.

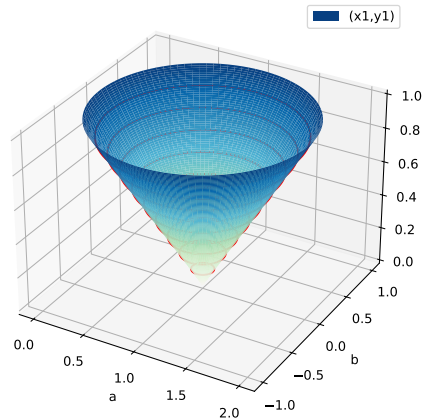


Figure A.6: Visualisation of point (x_1, y_1) that is shown Figure A.5a for different radii in the parameter space. For every value of r , point (x_1, y_1) is represented by a different circle in the parameter space, resulting in a cone shape.

A.3. Fourier Transform

The fringe frequency of a microbubble can be determined using a FT, which converts functions from the time to frequency domain, thereby providing information on the frequencies of the functions [90]. The main principle behind an FT is that any continuous function can be written as a combination of sine and cosine waves and can in complex notation be written as [91]:

$$\mathcal{F}(\omega) = \int_{-\infty}^{\infty} f(t) \cdot e^{-i\omega t} dt \quad \text{with } \omega = 2\pi f_f \tag{A.7}$$

where \mathcal{F} denotes the FT of a continuous function f . It should be noted that this definition of the FT only holds for non-periodic functions. For a periodic function with period T , i.e., $f(t+T)=f(t)$, the FT will go to infinity, as the frequency is identical for each period of the function. The FT of a periodic function is therefore written as a series of sines or cosines rather than an integral form. Using Euler's equation,

this FT can in complex notation be written as [90]:

$$\mathcal{F}(\omega) = \sum_{n=-\infty}^{\infty} c_n \cdot e^{in\omega_0 t} \quad \text{with } c_n = \frac{1}{T} \int_{-T/2}^{T/2} f(t) e^{-in\omega_0 t} dt \quad \text{for } n \in \mathbb{Z} \quad (\text{A.8})$$

where ω_0 denotes the fundamental frequency of $f(t)$ equal to $2\pi/T$. Next, c_n represents the amplitude and phase of each frequency component. The application of the FT is widely used in different fields of research, such as signal processing, where the FT of a function is numerically solved [91]. One way to solve this is by applying a Discrete Fourier Transform (DFT) on an array of data. This method relies on linear interpolation of a function by making use of the trapezoidal rule [90]. If the number of data representing the function is N , the computational time of a DFT is $\mathcal{O}(N^2)$ [91]. As the computational time increases significantly for a large data set, a faster approach is favourable. Therefore, an algorithm called a Fast Fourier Transform (FFT) of the DFT has been developed, which reduces the computation time to $\mathcal{O}(N \log(N))$ [91].

The theory behind the FT can be expanded to multiple dimensions making it possible to perform an FT on fringe patterns of microbubbles. Two examples of fringe patterns and their spatial frequencies are illustrated in Figures A.7 and A.8, respectively. The frequencies obtained with the FFT are illustrated using a power density spectrum (PSD), which shows the power of these frequencies. The FFT algorithm shows two equivalent spatial frequencies with opposite signs for each fringe pattern, due to the appearance of sine and cosines in the frequency domain. However, in this study, only the positive spatial frequency is considered.

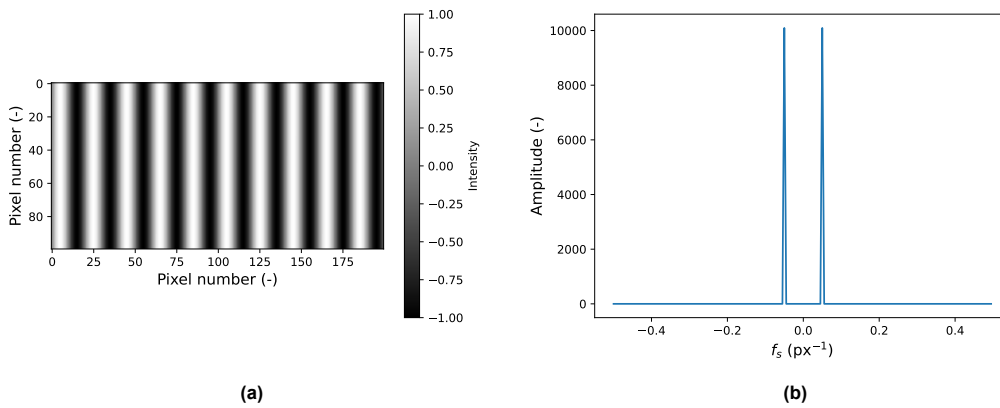


Figure A.7: a) Fringe pattern ($f=0.05$ cycles/px) for a resolution of 200 by 100 px and b) corresponding spatial frequency retrieved from FFT analysis

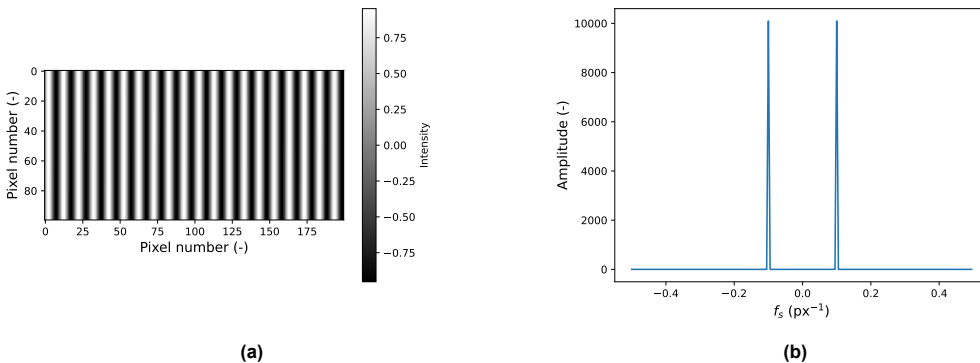


Figure A.8: a) Fringe pattern ($f=0.1$ cycles/px) for a resolution of 200 by 100 px and b) corresponding spatial frequency retrieved from FFT analysis

B

Concentration distributions

The microbubble concentration distribution for a runner speed of 1000 and 1200 rpm for different DO concentrations and different values of σ is illustrated in Figure [B.1](#) for the critical working point considered in this study. A more detailed overview of the microbubble concentration distribution observed at a DO concentration of 3.5 mg/L for these runner speeds is illustrated in Figure [B.2](#).

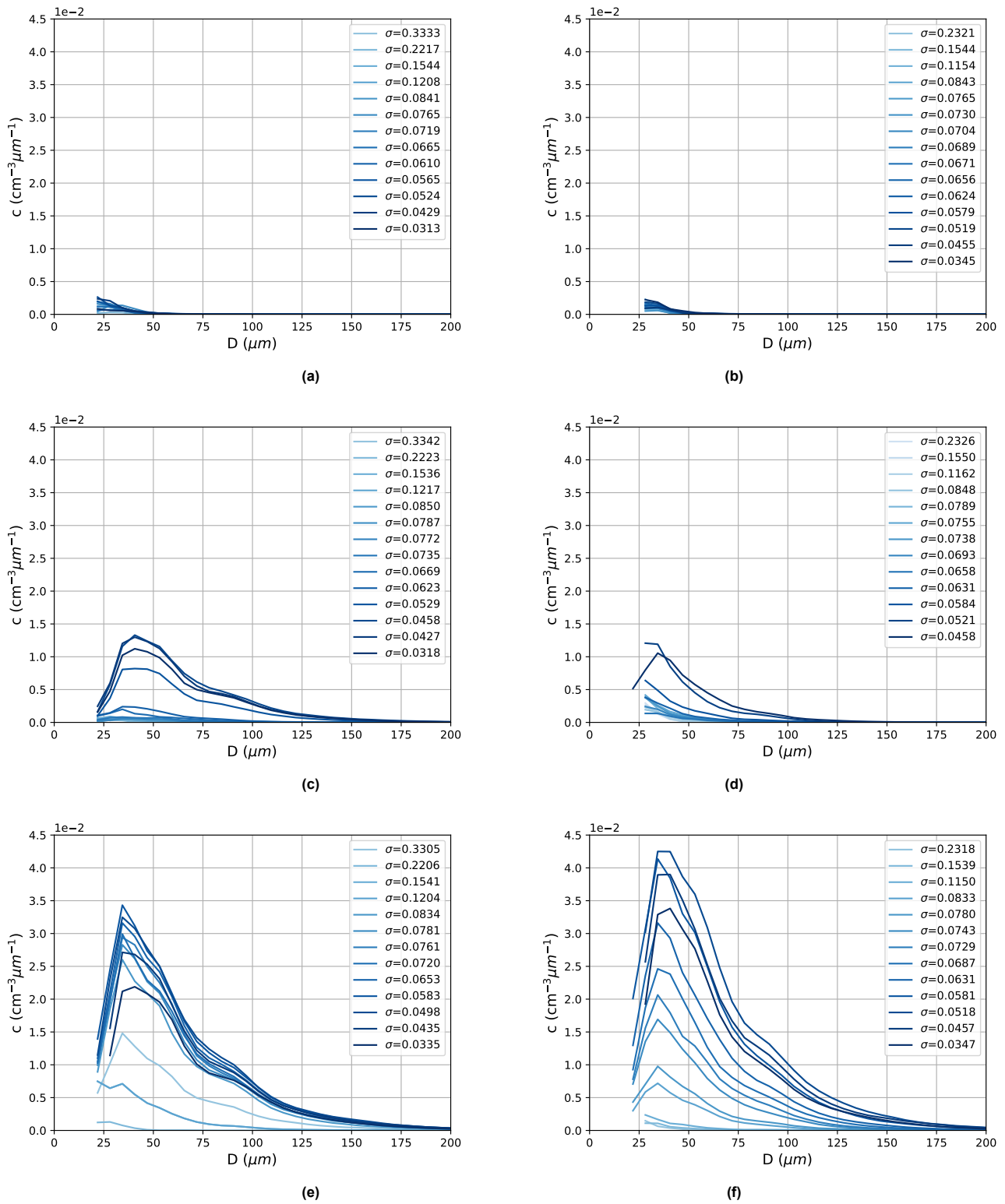


Figure B.1: Average microbubble concentration distribution of all Monte Carlo simulations for a working point with characteristics $n_{ED}=0.2234$, $Q_{ED}=0.2293$, $AOA=20.3^\circ$ for a) $n=1000$ rpm, $\text{DO}=3.5$ mg/L, b) $n=1200$ rpm, $\text{DO}=3.5$ mg/L, c) $n=1000$ rpm, $\text{DO}=5.5$ mg/L, d) $n=1200$ rpm, $\text{DO}=5.5$ mg/L, e) $n=1000$ rpm, $\text{DO}=8.5$ mg/L, f) $n=1200$ rpm, $\text{DO}=8.5$ mg/L

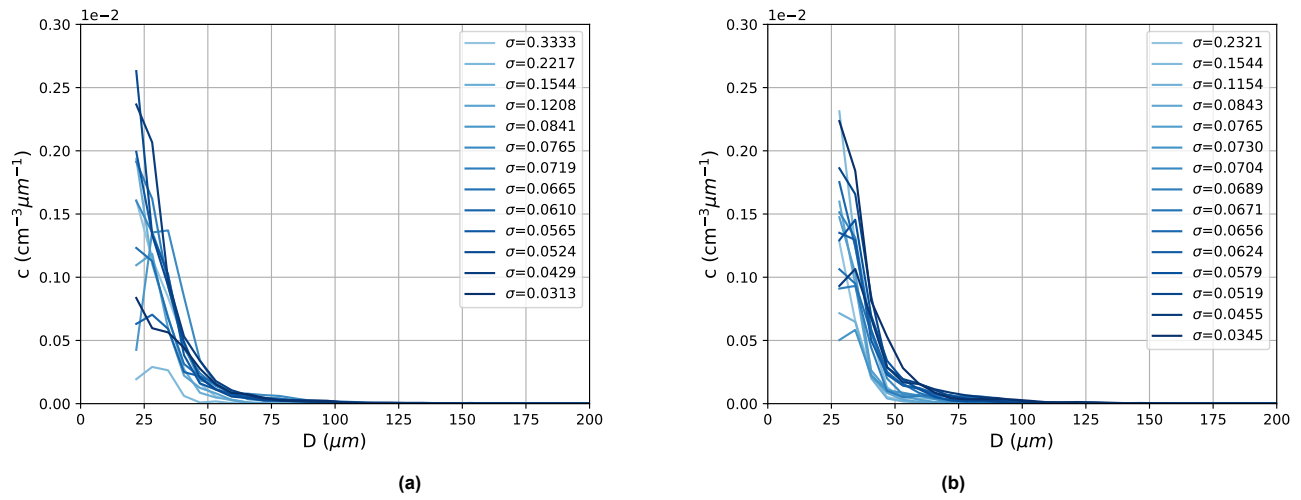


Figure B.2: Average microbubble concentration distribution of all Monte Carlo simulations for a working point with characteristics $n_{ED}=0.2234$, $Q_{ED}=0.2293$, $AOA=20.3^\circ$ for a) $n=1000$ rpm, $\text{DO}=3.5$ mg/L, b) $n=1200$ rpm, $\text{DO}=3.5$ mg/L.